

How high frequency atmospheric forcing impacts mesoscale eddy surface signature and vertical structure

Alexandre Barboni¹, alexandre stegner², Franck DUMAS³, and Xavier J. Carton⁴

¹École Polytechnique

²Laboratoire de Météorologie Dynamique, CNRS, IPSL

³SHOM

⁴Universite de Bretagne Occidentale

July 23, 2023

Abstract

Seasonal evolution of both surface signature and subsurface structure of a Mediterranean mesoscale anticyclones is assessed using the CROCO high-resolution numerical model with realistic background stratification and fluxes. In good agreement with remote-sensing and in-situ observations, our numerical simulations capture the seasonal cycle of the anomalies, induced by the anticyclone, both in the sea surface temperature (SST) and the mixed layer depth (MLD). The eddy signature on the SST shifts from warm-core in winter to cold-core in summer, while the MLD deepens significantly in the core of the anticyclone in late winter. Our sensitivity analysis shows that these dynamical properties can be accurately reproduced only if the resolution is high enough (~ 1 km for the horizontal with 100 vertical levels in a Mediterranean stratification) and if the atmospheric forcing contains high-frequency. In this configuration the deformation radius is explicitly resolved and the vertical mixing parametrized by the k- ϵ closure scheme is three times higher inside the eddy than outside the eddy. This differential mixing is explained by near-inertial waves, triggered by the high-frequency atmospheric forcing. Near-inertial waves propagate more energy inside the eddy because of the lower effective Coriolis parameter in the anticyclonic core. In addition to these high spatial and temporal resolution, SST retroaction on air-sea fluxes appears to be necessary to obtain marked eddy mixed layer depth anomaly.

1 **How high frequency atmospheric forcing impacts**
2 **mesoscale eddy surface signature and vertical structure**

3 **Alexandre Barboni** ^{1,2,3}, **Alexandre Stegner** ¹, **Franck Dumas** ^{2,3}, **Xavier**
4 **Carton** ³

5 ¹Laboratoire de Météorologie Dynamique/IPSL, Ecole Polytechnique, Institut Polytechnique de Paris,

6 ENS, Université PSL, Sorbonne Université, CNRS, 91128 Palaiseau, France

7 ²Service Hydrographique et Océanographique de la Marine, 29200 Brest, France

8 ³Laboratoire d'Océanographie Physique et Spatiale, UBO, CNRS, IRD, Ifremer, 29280 Plouzané, France

9 **Key Points:**

- 10 • Seasonal variations in SST and mixed layer anomalies of a Mediterranean anti-
11 cyclone are retrieved in high resolution simulation
- 12 • The summer surface cold-core signatures are driven by differential vertical mix-
13 ing due to near-inertial waves
- 14 • SST retroaction on air-sea fluxes is necessary to retrieve eddy-induced mixed layer
15 anomalies

Corresponding author: Alexandre Barboni, alexandre.barboni@lmd.ipsl.fr

Abstract

Seasonal evolution of both surface signature and subsurface structure of a Mediterranean mesoscale anticyclones is assessed using the CROCO high-resolution numerical model with realistic background stratification and fluxes. In good agreement with remote-sensing and in-situ observations, our numerical simulations capture the seasonal cycle of the anomalies, induced by the anticyclone, both in the sea surface temperature (SST) and the mixed layer depth (MLD). The eddy signature on the SST shifts from warm-core in winter to cold-core in summer, while the MLD deepens significantly in the core of the anticyclone in late winter. Our sensitivity analysis shows that these dynamical properties can be accurately reproduced only if the resolution is high enough ($\sim 1km$ for the horizontal with 100 vertical levels in a Mediterranean stratification) and if the atmospheric forcing contains high-frequency. In this configuration the deformation radius is explicitly resolved and the vertical mixing parametrized by the $k-\epsilon$ closure scheme is three times higher inside the eddy than outside the eddy. This differential mixing is explained by near-inertial waves, triggered by the high-frequency atmospheric forcing. Near-inertial waves propagate more energy inside the eddy because of the lower effective Coriolis parameter in the anticyclonic core. In addition to these high spatial and temporal resolution, SST retroaction on air-sea fluxes appears to be necessary to obtain marked eddy mixed layer depth anomaly.

Plain Language Summary

Mesoscale eddies are turbulent structures present in every regions of the world ocean, and accounting for a significant part of its kinetic energy budget. These structures can be tracked in time and recently revealed a seasonal cycle from in situ data. An anticyclone (clockwise rotating eddy in the northern hemisphere) is observed in the Mediterranean to be predominantly warm at the surface and to deepen the mixed layer in winter, but shifts to a cold-core summer signature. This seasonal signal is not yet understood and studied in ocean models. In this study we assess the realism of an anticyclone seasonal evolution in high resolution numerical simulations. Eddy surface temperature seasonal shift is retrieved and is linked to an increased mixing at the eddy core spontaneously appearing at high resolution (grid size $\sim 1km$) in the presence of high frequency atmospheric forcing. This increased mixed is due to the preferred propagation of near-inertial waves in the anticyclone due to its negative relative vorticity. Eddy-induced mixed layer depth anomalies also appear to be triggered by sea surface temperature retroaction on air-sea fluxes. These results suggest that present-day operational ocean forecasting models are too coarse to accurately retrieve mesoscale evolution.

1 Introduction

Mesoscale eddies are ubiquitous turbulent structures in the oceans, in thermal wind balance with a signature in density. Eddies have been observed for a long time, in particular in energetic regions such as the Gulf Stream rings (Richardson, 1980), the Kuroshio extension (Itoh & Yasuda, 2010), the Agulhas current retroflexion (Olson & Evans, 1986), but also in the Mediterranean Sea (Mkhinini et al., 2014). Mesoscale anticyclones (respectively cyclones) are structures of negative (positive) density anomaly, identified with a sea surface height (SSH) elevation (depression) (Chelton et al., 2007). Eddies statistical descriptions really began with the availability of eddy automated detections based on gridded altimetry products (Doglioli et al., 2007; Chaigneau et al., 2009; Nencioli et al., 2010; Chelton, Schlax, & Samelson, 2011; Mason et al., 2014; Le Vu et al., 2018; Laxenaire et al., 2018). The first quantitative studies were done in a composite approach : many daily snapshots detections are colocated with eddy contours and gathered into a single annual mean eddy signature (Hausmann & Czaja, 2012; Everett et al., 2012). This approach combined with remote-sensing measurements provide an extensive view of ed-

66 dies in various regions of the global ocean, with SST, sea surface salinity (Trott et al.,
 67 2019), chlorophyll (Chelton, Gaube, et al., 2011) and also meteorological variables (Frenger
 68 et al., 2013). Composite approach also allowed to reveal a modulation of air-sea fluxes
 69 at the eddy scale : in the Agulhas retroflexion region, (Villas Bôas et al., 2015) showed
 70 the total heat flux to the atmosphere to be enhanced over very strong and warm anti-
 71 cyclones. Similarly for the eddy vertical structure, gathering Argo profiles as a function
 72 of normalized distance to the eddy center, eddies were found to influence the mixed layer
 73 depth (MLD) (Sun et al., 2017; Gaube et al., 2019). Anticyclones have deeper MLD in
 74 their core, cyclones shallower MLD, with larger mixed layer anomalies in winter. Eddies
 75 were also observed to incorporate a significant seasonal cycle in their radius variations
 76 (Zhai et al., 2008) and their SST signature (Sun et al., 2019; Y. Liu et al., 2021). An-
 77 ticyclones (respectively cyclones) usually identified as warm in surface, actually shift to
 78 cold (warm) signatures in summer in several regions of the world ocean (Sun et al., 2019;
 79 Moschos et al., 2022). This phenomenon is then referred to as 'inverse' SST signatures.
 80 (Moschos et al., 2022) showed that these 'inverse' signatures actually become predom-
 81 inant in summer in the Mediterranean Sea, a seasonal shift yet not properly understood.

82 The composite approach is nonetheless ill-suited to study eddy temporal variabil-
 83 ity due to the stacking of numerous observations in time. Recently Lagrangian approaches
 84 were developed to study eddies enabling to better track their temporal variability (Pessini
 85 et al., 2018; Laxenaire et al., 2020; Barboni et al., 2021). Using a Lagrangian approach,
 86 (Moschos et al., 2022) showed that the same individual anticyclones shift from a warm
 87 winter SST anomaly to a cold one in summer (and conversely for cyclone). With the ad-
 88 ditional Argo floats trapped in anticyclones, they further noticed that anticyclonic den-
 89 sity anomaly remain warmer at depth while becoming colder in surface, leading to a smoother
 90 density gradient. Hence the hypothesis that this seasonal shift could be explained by a
 91 modulation of the vertical mixing by mesoscale eddies, anticyclones (cyclones) likely en-
 92 hancing (decreasing) mixing in surface. Recent observations in the Mediterranean Sea
 93 of inside-anticyclone properties temporal evolution further revealed eddy mixed layer anom-
 94 alies to be much larger than the composite approach mean value, reaching sometimes 300m
 95 (Barboni, Coadou-Chaventon, et al., 2023). MLD anomalies evolution was also shown
 96 to have evolution much faster than the month, with delayed restratification inside an-
 97 ticyclones. Mechanisms driving these MLD anomalies are also unexplained, but (Barboni,
 98 Coadou-Chaventon, et al., 2023) found it to be impacted by interactions with the an-
 99 ticyclone vertical structure.

100 An eddy modulation of vertical mixing was not proven so far but could be due to
 101 a modulation of near-inertial waves (NIW) propagation. NIW can not propagate at fre-
 102 quencies lower than the inertial frequency f due to Earth rotation (Garrett & Munk, 1972).
 103 However in the presence of a balanced flow, anticyclones (cyclones) having negative (pos-
 104 itive) relative vorticity ζ locally shift this cut-off by an effective inertial frequency $f_e =$
 105 $f + \zeta/2$ (Kunze, 1985). Sub-inertial waves ($\omega \lesssim f$) can then remained trapped in an-
 106 ticyclones and supra-inertial waves ($\omega \gtrsim f$) can be expelled from cyclones. Consequently,
 107 NIW propagate more inside anticyclones, what was experimentally (D'Asaro, 1995) and
 108 numerically (Danioux et al., 2008, 2015; Asselin & Young, 2020) proven. This NIW trap-
 109 ping potential partly explains the interest in anticyclones rather than in cyclones, the
 110 other reason likely being that anticyclones are more stable in time (Arai & Yamagata,
 111 1994; Graves et al., 2006), in particular for large structures (Perret et al., 2006), then
 112 more easily detected and trapping more often profilers (thus easing field campaigns). Sev-
 113 eral recent observations (Martínez-Marrero et al., 2019; Fernández-Castro et al., 2020)
 114 showed that mixing at depth is enhanced below anticyclones due to this more energetic
 115 NIW propagation. On the other hand numerical studies assumed extremely simplified
 116 set-up with constant wind (Danioux et al., 2008) or an idealized wind burst (Asselin &
 117 Young, 2020). They also looked at NIW propagation in an eddying field at short time
 118 scales, then without significant evolution of the eddies and stratification. Eddy-NIW in-
 119 teraction on longer time scales - eddy evolving time scales like months - in a varying strat-

120 ification due to seasonal cycle has never been assessed so far. In particular the effect of
 121 this differential NIW propagation on eddies remains unknown and a gap remains between
 122 wave propagation and enhanced surface mixing.

123 Some recent studies started to assess eddy temporal evolution in high resolution
 124 regional models. In the Mediterranean Sea, Escudier et al. (2016) compared eddy size,
 125 drift and lifetime compared to eddies in altimetric observations. Mason et al. (2019) in-
 126 vestigated these variables in assimilated operational models and additionally looked at
 127 MLD anomalies, but both were in a composite approach and did not look at eddy SST
 128 variations. More recently Stegner et al. (2021) performed an observation system simu-
 129 lation experiment on a $1/60^\circ$ simulation of the Mediterranean sea and found great bias
 130 on size and strength for small eddy detections, but did not look at SST variations. Us-
 131 ing the same simulation, an interesting method was developed by Ioannou et al. (2021),
 132 investigating differences in both trajectories, size and stratification of the Ierapetra an-
 133 ticyclonic eddy, but restricted to this particular case.

134 Both eddy SST anomalies seasonal shift and mixed layer depth anomalies remain
 135 poorly investigated so far in ocean models. If NIW propagation and eddy vertical struc-
 136 ture are considered, grid resolution - both horizontal and vertical - and atmospheric forc-
 137 ing are likely key aspects to take into account. Indeed air-sea fluxes and near-inertia-gravity
 138 waves involve much shorter temporal and spatial scales, not reproduced even in eddy-
 139 permitting models at present stage. We then aim to assess the realism of an anticyclone
 140 seasonal signal in both surface and mixed layer using an idealized but high-resolution
 141 simulation and investigating driving physical processes. The goal is to assess the real-
 142 ism of the eddy temporal evolution compared to similar observations, in particular the
 143 retrieval of the surface signature seasonal cycle. In a first part we conduct a sensitivity
 144 analysis on horizontal grid cell. In a second part we study the sensitivity to atmospheric
 145 forcing frequency. Last, the effect of SST retroaction on air-sea fluxes is discussed.

146 2 Methods

147 2.1 Model set-up

148 Idealized numerical experiments are performed using the Coastal and Regional Ocean
 149 Community (CROCO) model. CROCO is based on the Regional Ocean Modeling Sys-
 150 tem (ROMS) kernel (Shchepetkin & McWilliams, 2005). It uses a time splitting method
 151 between the fast barotropic mode and the slow baroclinic ones. Advection schemes are
 152 UP3 for horizontal and Akima-Splines for the vertical. Trying to conciliate realistic and
 153 idealized approach, we use double periodic conditions in a realistic stratification and on
 154 long timescale. The atmospheric forcing has realistic temporal variations but is spatially
 155 homogeneous. The only active tracer used is temperature. As a consequence, a linear
 156 state equation links density ρ and temperature T , with thermal expansion $T_c = 0.28kg.m^{-3}.K^{-1}$
 157 and linear approximation close to $T_0 = 25^\circ C$ and $\rho_0 = 1026kg.m^{-3}$:

$$\rho = \rho_0 + T_c(T - T_0) \quad (1)$$

158 Discarding salinity effects is justified by the very weak salinity seasonal cycle in the
 159 Mediterranean Sea. The heat flux seasonal cycle is roughly $\pm 150 W.m^{-2}$ (Pettenuzzo et
 160 al., 2010), whereas salinity fluxes are mostly driven by the evaporation minus precipi-
 161 tation balance, with a mean of roughly $10^3 mm/y$, a seasonal cycle maximal amplitude
 162 of $\Delta F = 4 \times 10^2 mm/y$ and river input being negligible (Mariotti, 2010). Consider-
 163 ing a haline contraction coefficient of $S_c = 0.78kg.m^{-3}.PSU^{-1}$, a ΔF freshwater in-
 164 put would have a seasonal equivalent effect on buoyancy $Q_{eq} = \rho_0 c_p \frac{S_c}{T_c} S_0 \Delta F \approx 5 W.m^{-2}$,
 165 indeed almost two orders of magnitude lower than Q_{tot} .

166

Grid

167

168

169

170

171

172

173

174

Simulation domain is double periodic, on the f -plane, with a flat bottom $H_{bot} = 3000m$. Horizontal extent is 200km in both directions, with horizontal resolution ranging between 4km and 500m, with respectively 25 to 150 vertical levels. Horizontal to vertical grid size ratio is kept roughly constant about 1000/3 in the upper layers, close to the Brunt-Vaisala to inertia frequency ratio. Coriolis parameter is $f = 9.0 \times 10^{-5} s^{-1}$. CROCO uses a σ terrain-following coordinate, the N vertical levels being modulated in time between bottom and sea surface height η . Constant depth level z_0 are stretched over thickness h_c with surface coefficient θ_s :

$$z = \eta + (\eta + H_{bot})z_0 \quad (2)$$

$$z_0 = \frac{h_c \sigma + H_{bot} C_s(\sigma)}{h_c + H_{bot}} \quad \text{with} \quad C_s(\sigma) = \frac{1 - \cosh(\theta_s \frac{\sigma - N}{N})}{\cosh(\theta_s) - 1} \quad (3)$$

175

176

177

178

179

180

With $N = 100$ levels, $h_c = 400m$ and $\theta_s = 8$, vertical grid steps are then close to 5m in the upper 200m. 200m being the vertical scale of the thermocline, it ensures a maximal resolution in the upper ocean where seasonal variations occur (Houpert et al., 2015). This configuration has then a higher vertical resolution than previous similar studies ($N = 32$ $h_c = 250m$ and $\theta_s = 6.5$ for Escudier et al. (2016)) or operational models (Juza et al., 2016).

181

Turbulent closure

182

183

184

185

Mixing is parametrized through k - ϵ closure scheme (Rodi, 1987) using the generic length scale approach (Umlauf & Burchard, 2003). Turbulent kinetic energy k dissipates with rate ϵ and stability function c_v into an effective viscosity ν (respectively c_T and κ for diffusivity). No additional explicit mixing is added.

$$\nu = \frac{c_v k^2}{\epsilon} \quad \text{and} \quad \kappa = \frac{c_T k^2}{\epsilon} \quad (4)$$

186

187

188

189

190

191

As implemented in the CROCO model, a minimal k input is parameterized. Given that the minimal dissipation rate ϵ is set to $10^{-12} W.kg^{-1}$, the minimal k has to be set to $10^{-9} m^2.s^{-2}$ in order to retrieve a minimal diffusivity of $10^{-6} m^2.s^{-1}$ with a stability function of order unity. This diffusivity value is close to kinematic viscosity and thermal diffusivity for water (respectively 1×10^{-6} and $1 \times 10^{-7} m^2.s^{-1}$). This issue is also discussed by Perfect et al. (2020).

2.2 Background stratification and initial mesoscale anticyclone

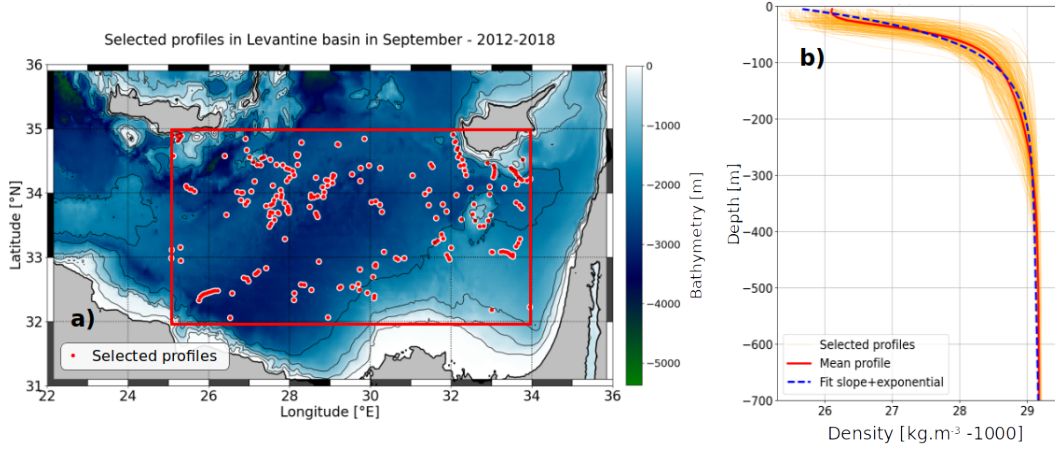


Figure 1. (a) Map showing the region of high long-lived anticyclones occurrence in the Levantine basin. The atmospheric fields used as input are averaged over the area delimited by the green frame. Black dots are the cast position of 242 selected in situ profiles identified as outside-eddy. Bathymetry is ETOPO1 data (Smith & Sandwell, 1997) with 0, 500, 1000 and 1500m isobaths. (b) Density vertical structure of selected profiles (orange thin lines), mean profile (red thick line) and fitted profile using Eq.5 (blue dashed).

A realistic background stratification is set from a climatological database gathering in situ delayed-time and near-real-time data from Copernicus Marine Environment Monitoring Service (Barboni, Stegner, et al., 2023). A region of interest is considered at the center of the Levantine Basin (25 to 34 °E and 32 to 35 °N, shown in Fig.1a). For background stratification we used only profiles in the region of interest, detected as outside-eddy using the DYNED eddy atlas dataset (see Barboni, Coadou-Chaventon, et al. (2023) for details), from 2012 to 2018 and for each year in September. Considering these criteria, 242 profiles are averaged into a mean stratification $\rho_b(z)$ fitted over the first 1000m with a linear slope S added to an exponential with vertical Z_T in the upper water column (Eq.5, see Fig.1b). September is chosen as the end of summer when the thermocline is marked and stratification gradient the strongest, allowing a better fit with exponential slope.

$$\rho_b(z) = \rho_1 + (\rho_s - \rho_1) \exp\left(-\frac{z}{Z_T}\right) + Sz \quad (5)$$

Regression fit gave $\rho_1 = 1029.03 \text{ kg.m}^{-3}$, $\rho_s = 1025.3 \text{ kg.m}^{-3}$, $Z_T = 55 \text{ m}$, $S = 1.8 \times 10^{-4} \text{ kg.m}^{-4}$. Corresponding baroclinic deformation radius is approximately 11km. An initial density anomaly σ in geostrophic equilibrium is added to the background stratification. $\sigma(r, z)$ is azimuthally symmetric and has a Gaussian shape in the vertical direction and pseudo-Gaussian in the radial one, with radius R_m and vertical extent H :

$$\sigma(r, z) = \sigma_0 \frac{z}{H} \exp\left(-\frac{1}{\alpha} \left(\frac{r}{R_m}\right)^\alpha\right) \exp\left(-\frac{1}{2} \left(\frac{z}{H}\right)^2\right) \quad \text{with} \quad \sigma_0 = \frac{\rho_0 f V_m R_m e^{1/\alpha}}{gH} \quad (6)$$

211 The initial maximal speed radius R_m is 25 km, slightly more than twice the defor-
 212 mation radius but still smaller than the large long-lived Eastern Mediterranean anticy-
 213 clones (Barboni, Coadou-Chaventon, et al., 2023), giving a Burger number ($Bu = R_d^2/R_m^2$)
 214 close to 0.2. Maximal speed is initially set to $V_m = 0.4 m.s^{-1}$ giving a Rossby number
 215 ($Ro = V_m/R_m f$) of 0.16, but later decays around 0.1 due to eddy evolution. $Ro = 0.1$
 216 is a standard value in the Mediterranean Sea (Ioannou et al., 2019). H is set to 100m
 217 on the same order as thermocline extent Z_T , and shape parameter $\alpha = 1.6$ ensures baro-
 218 clinic stability (Carton et al., 1989; Stegner & Dritschel, 2000). Cyclogeostrophic cor-
 219 rection is added following Penven et al. (2014).

220 **2.3 Atmospheric heat forcing**

221 Air-sea fluxes are computed with the Coupled Ocean–Atmosphere Response Ex-
 222 periment (COARE) 3.0 parametrization (Fairall et al., 2003), with improved accuracy
 223 for large wind speeds ($> 10m.s^{-1}$) encountered in high frequency forcing. Short wave
 224 heat flux Q_{SW} is distributed on the vertical following Paulson and Simpson (1977) trans-
 225 parency model with Jerlov water type I, consistent with very clear Mediterranean wate-
 226 rs ($R = 0.58$, $\zeta_1 = 0.35m$, $\zeta_2 = 23m$):

$$I(z) = Q_{SW} \left(R \exp\left(-\frac{z}{\zeta_1}\right) + (1 - R) \exp\left(-\frac{z}{\zeta_2}\right) \right) \quad (7)$$

227 Upward long-wave heat flux Q_{LW}^\uparrow computes the ocean SST (T_s) thermal loss us-
 228 ing Stefan-Boltzmann black body law, with emissivity $\epsilon_{sb} = 98.5\%$ and $\sigma_{sb} = 5.6697 \times$
 229 $10^{-8} W.m^{-2}.K^{-4}$, convention positive downwards :

$$Q_{LW}^\uparrow = -\epsilon_{sb} \sigma_{sb} T_s^4 \quad (8)$$

230 Latent heat flux Q_{Lat} and sensible heat flux Q_{Sen} also involves a direct SST retroac-
 231 tion:

$$Q_{Lat} = -\rho_a L_E C_E |V| (q_s - q_a) \quad ; \quad Q_{Sen} = -\rho_a c_p C_S |V| (T_s - T_{2m}) \quad (9)$$

232 With ρ_a air density, c_p air thermal capacity, L_E evaporation enthalpy and $|V|$ 10m
 233 wind speed. q_s and q_a are specific humidity for ocean and atmosphere at 2m respectively,
 234 saturated at T_s for q_s , related to saturated water pressure P_{sat} fro q_a : $q_a = 0.622 h_{2m} P_{sat}(T_{2m}) / P_{SL}$
 235 and $q_s = 0.98 \times 0.622 \times P_{sat}(T_s) / P_{SL}$. Factor 0.98 accounts for water vapor reduction
 236 caused by salinity (Sverdrup et al., 1942). Last, wind stress is computed from zonal and
 237 meridional winds (u and v) :

$$\tau_x = \frac{\rho_a}{\rho_0} C_D |u| u \quad \text{and} \quad \tau_y = \frac{\rho_a}{\rho_0} C_D |v| v \quad (10)$$

238 In equations 9-10, C_E , C_S and C_D are corresponding transfer coefficients consid-
 239 ering the stability of the atmospheric boundary layer based on the Monin-Obukhov simi-
 240 larity theory. They are all on the order of 1×10^{-3} (Fairall et al., 2003).

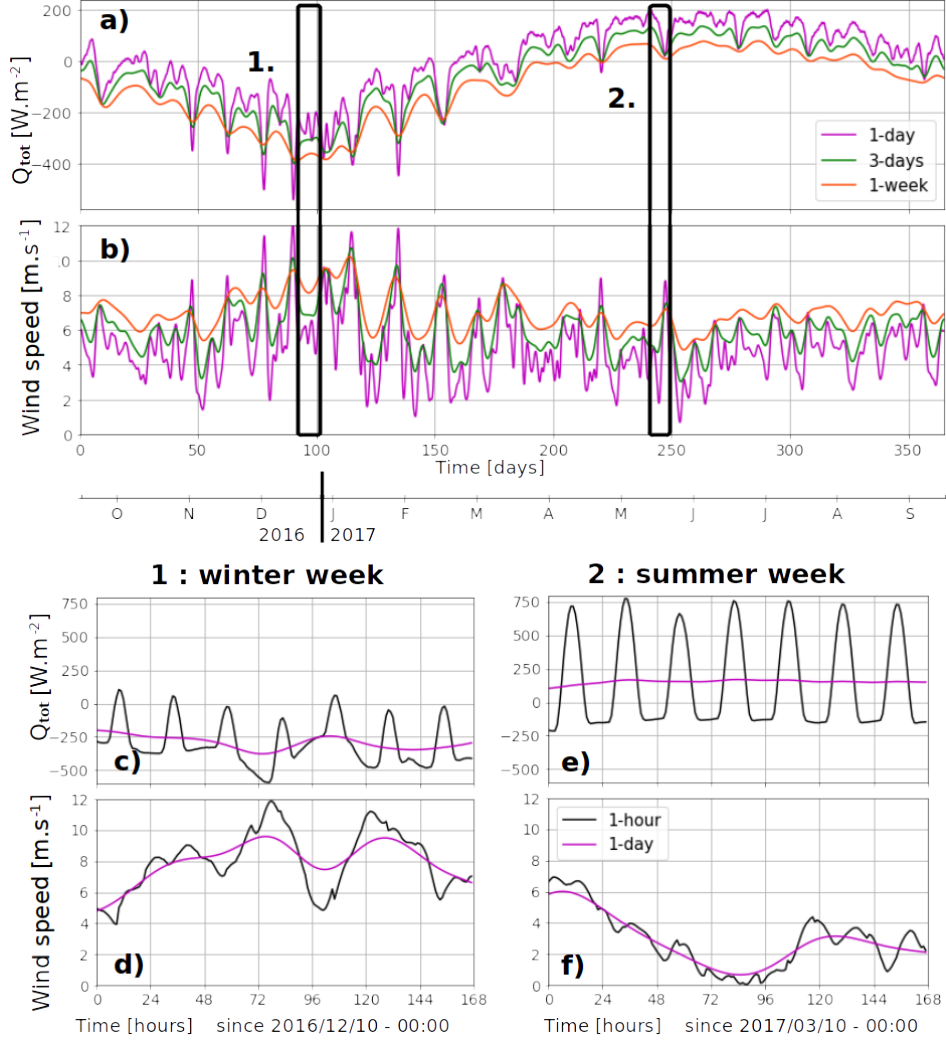


Figure 2. Net heat flux and wind speed for the 5 input timeseries, shown separately as diurnal cycle gives larger variations. (a) Net heat flux and (b) wind speed for the 1-day (magenta line), 3-days (green) and 1-week (orange) timeseries over one year. To enhance readability, 3-days and 1-week net heat flux are lowered by 20 and 40 $W.m^{-2}$ respectively. (c) 1-hour (black) and 1-day (magenta) net heat flux (respectively (d) for wind speed) in a winter week of 2016. (e) and (f) : same as (c) and (d) in a summer 2017 week.

241 ERA5 reanalysis input is used for atmospheric forcing. Fields are available with
 242 a 1 hour temporal resolution and $1/4^\circ$ horizontal resolution (Hersbach et al., 2020). To
 243 focus on the temporal variability, forcing timeseries are spatially averaged over the Lev-
 244 antine basin (Fig.1a). Four forcing inputs with different temporal scales are tested : 1-
 245 hour, 1-day, 3-days and 1-week. The 1-hour forcing is the original ERA5 timeseries, the
 246 three later ones are Gaussian smoothing of the 1-hour timeseries with double-window
 247 size of 1, 3 and 7 days respectively, shown in Fig.2. One year of forcing from 15 Septem-
 248 ber 2016 to 15 September 2017 runs cyclically for 2 years as forcing input, with root mean
 249 square wind speed $\bar{V} = 5.5 m.s^{-1}$. 10m neutral wind from ERA5 is used for wind stress
 250 in Eq.10. To keep the same wind speed magnitude with varying wind frequency, smoothed
 251 timeseries for zonal and meridional winds (\bar{u} and \bar{v}) have to be rescaled. The correction
 252 factor λ being $\gtrsim 1.1$ for 1-day timeseries, and $1.1 < \lambda < 2$ for 3-days and 1-week :

$$\tilde{u} = \lambda \bar{u}; \tilde{v} = \lambda \bar{v} \quad \text{with} \quad \lambda = \frac{\sqrt{u^2 + v^2}}{\sqrt{\bar{u}^2 + \bar{v}^2}} \quad (11)$$

253 The same year is kept to avoid disturbance with interannual variations, which are
 254 strong for heat fluxes over the Mediterranean Sea (Mariotti, 2010; Pettenuzzo et al., 2010),
 255 but no significant variations were observed when selecting another year.

256 ***Forcing without surface temperature retroaction***

257 A comparison experiment is run without SST retroaction on ocean-atmosphere fluxes.
 258 In this configuration, the net heat flux Q_{tot} from ERA5 directly forces the upper ocean
 259 layer, the short wave part Q_{SW} being still distributed on the vertical (Eq.7). Momen-
 260 tum fluxes are computed from Eq.10 with constant drag coefficient $C_D = 1.6 \times 10^{-3}$.
 261 The net heat flux Q_{tot} timeseries in ERA5 has daily amplitudes around $\pm 150 W.m^{-2}$ and
 262 an annual average of $-3.0 W.m^{-2}$, consistent with the net evaporation of the Mediter-
 263 ranean sea (Mariotti, 2010). The net heat flux is then corrected by linearly decreasing
 264 the negative values to achieve a zero annual average, avoiding a drift of the mean strat-
 265 ification.

266 **2.4 Eddy tracking indicators**

267 ***Eddy shape, radius and intensity***

268 Eddy detections are provided through the Angular Momentum Eddy Detection and
 269 Tracking Algorithm (AMEDA). AMEDA is a mixed velocity-altimetry approach, its re-
 270 lies on using primarily streamlines from a velocity field and identifying possible eddy cen-
 271 ters computed as maxima of local normalized angular momentum (Le Vu et al., 2018).
 272 It was successfully used in several regions of the world ocean in altimetric data (Aroucha
 273 et al., 2020; Ayouche et al., 2021; Barboni et al., 2021), high frequency radar data (F. Liu
 274 et al., 2020) or numerical simulations (de Marez et al., 2021). In each eddy single ob-
 275 servation (one eddy observed one day), AMEDA gives a center (which position is noted
 276 \mathbf{X}_e hereafter) and two contours. The 'maximal speed' contour is the enclosed stream-
 277 line with maximal speed (i.e. in the geostrophic approximation, with maximal SSH gra-
 278 dient) ; it is assumed to be the limit of the eddy core region where water parcels are trapped.
 279 The 'end' contour is the outermost closed SSH contour surrounding the eddy center and
 280 the maximal speed contour ; it is assumed to be the area of the eddy footprint, larger
 281 than just its core but still influenced by the eddy shear (Le Vu et al., 2018). The observed
 282 maximal speed radius R_m is then defined as the radius of the circle having an area equal
 283 to the maximal speed contour. Eddy detection through interpolated Level 4 SSH prod-
 284 ucts leads to imperfections. It typically smooths gradients and then reduces observed
 285 geostrophic velocities (Amores et al., 2018; Stegner et al., 2021). To mimic those imper-
 286 fections in the numerical simulations, AMEDA detections are performed on the 48h-averaged
 287 SSH field at model grid resolution.

288 ***Eddy SST signature δT , heat flux δQ , differential mixing ratio ξ and mixed*** 289 ***layer anomaly***

290 The anticyclone-induced SST signature δT is defined as the difference of SST be-
 291 tween the eddy core SST_{in} and its periphery SST_{peri} . Adapting Moschos et al. (2022),
 292 SST_{in} is the average of the area centered on $\mathbf{X}_e(t)$ with radius $2/3R_m(t)$; SST_{peri} is
 293 the average on an annular area centered on \mathbf{X}_e with radius between $2/3R_m(t)$ and $2R_m(t)$.
 294 Positive (negative) δT then indicates a warm-core (cold-core) signature. Similarly the
 295 induced signature on ocean-atmosphere fluxes is defined as δQ , with positive δQ for in-
 296 creased warming at the eddy core. Thermal heat flux feedback (THFF) is then defined

297 as the linear regression of δQ as a function of δT over the second year of simulation (from
298 365 to 730 days, see Sect.3.3).

299 Differential mixing between the eddy core and outside-eddy are measured through
300 the index ξ . Temperature vertical diffusivity κ computed by $k-\epsilon$ mixing closure from
301 instantaneous history record is spatially averaged in the eddy core (κ^{AE}) and outside-
302 eddy (κ^{Out}). The eddy core region corresponds here to the area around the eddy center
303 with radius $2/3R_m(t)$. The outside-eddy region is defined as the area outside any 'end'
304 contours detected by the tracking algorithm. Diffusivity spanning several orders of mag-
305 nitude, differential mixing ξ is then evaluated as a vertical average of the ratio of these
306 two quantities, typically using a depth $h = 20m$ to focus on the upper layers stratified
307 in summer :

$$\xi = \frac{1}{h} \int_{-h}^{surf} \frac{\kappa^{AE}}{\kappa^{Out}} dz \quad (12)$$

308 Summer eddy SST signature magnitude $\overline{\delta T}$ is defined as the 30th δT percentile over
309 the summer, and its spread as the difference between the 30th and the 10th percentiles
310 (see results in Table 1). Similarly ξ is defined as the median of the ξ distribution over
311 the summer, and its spread as the difference between the median and the 30th percentile.
312 First and second summers are defined as 230 to 340 days and 590 to 700 days respec-
313 tively, corresponding to the May to August period when a significant number of warm-
314 core anticyclones are observed (Moschos et al., 2022).

315 Last, the MLD anomaly ΔMLD are defined for a given winter as the maximal dif-
316 ference reached between the MLD outside-eddy and the MLD inside-eddy, following (Barboni,
317 Coadou-Chaventon, et al., 2023). In the following numerical experiments running for 2
318 years, the first winter is considered as a transient period not retained for analysis. ΔMLD
319 is then computed only for the second winter, defined as 450 to 580 days, corresponding
320 to the December to April period, when maximal MLD are reached in the Mediterranean
321 Sea (Houpert et al., 2015).

322 **3 Idealized simulations compared to observations**

323 The temporal evolution of mesoscale eddies in the Levantine basin can be retrieved
324 for several anticyclones where Argo floats remained trapped several months, as exten-
325 sively studied in Barboni, Coadou-Chaventon, et al. (2023). A marked seasonal signal
326 is detected in both SST and vertical structure. An example is shown in Fig.3 with a Ier-
327 apetra anticyclone. Ierapetra anticyclones are strong recurrent anticyclonic structures
328 formed each year in the lee of Crete island (Ioannou et al., 2020). In the example shown
329 below, δT index has a marked oscillation between a winter warm core and summer cold
330 core. The weekly smoothed signature can be measured to about $\delta T \approx +0.7^\circ C$ in both
331 winters 2016-2017 and 2017-2018, and about $-0.3^\circ C$ in summer 2017 (about $-0.2^\circ C$
332 in summer 2018). The vertical structure could also be measured thanks to large Argo
333 deployments (Fig.3h) ; due to errors in the salinity sensors, density in 2018 is estimated
334 from temperature applying a linear regression using 2017 data. One can also notice the
335 seasonal variations of the anticyclone maximal speed, with two maxima in late winter.
336 This is consistent with kinetic energy inverse cascade maximal peak from submesoscale
337 to mesoscale in kinetic energy distributions (Zhai et al., 2008; Steinberg et al., 2022), but
338 it is still noticeable to have the same phenomenon tracking a single individual structure.
339 Here the physical processes driving these observed seasonal variations are studied with
340 numerical experiments, investigating sensitivity to horizontal resolutions, forcing frequency
341 and SST retroaction on air-sea fluxes. Simulations are summarized in Table 1, the ref-
342 erence considered being 1km resolution with 1-hour forcing, 100 vertical levels with SST
343 retroaction (run 1K100-1H in Table 1 below).

Ierapetra anticyclone timeline (2016-2018)

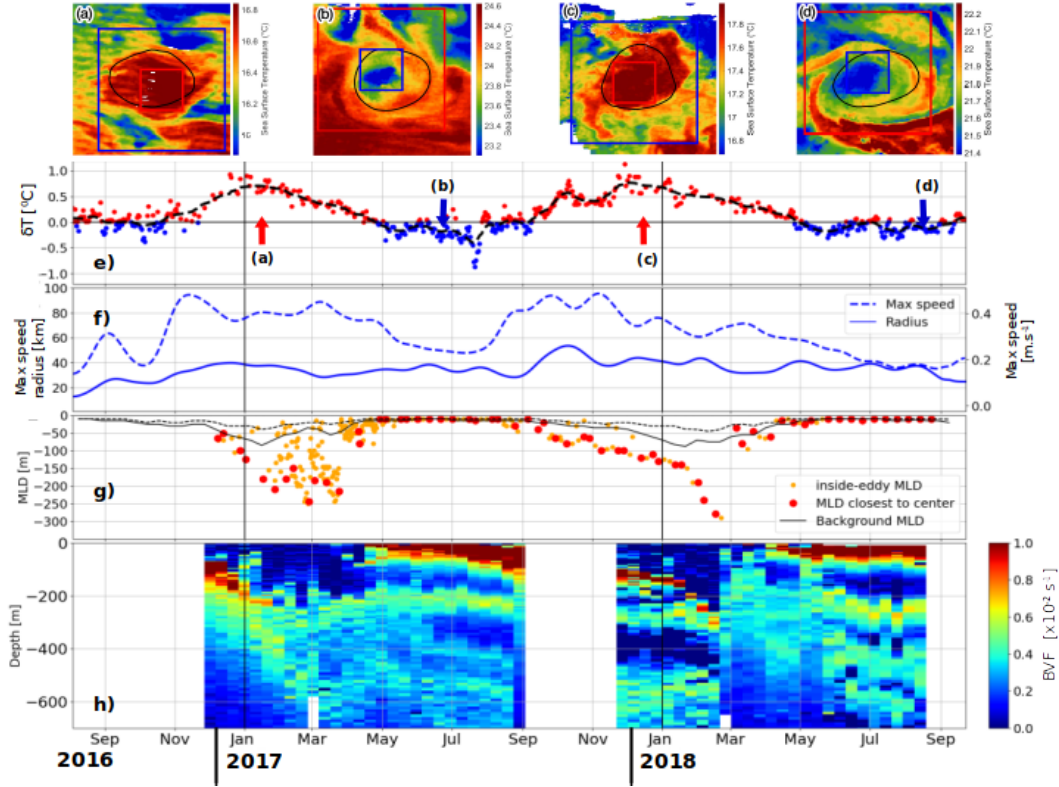


Figure 3. Temporal evolution of the Ierapetra anticyclone formed South-East of Crete in late summer 2016. Upper panels are high-resolution SST snapshots in (a) January 2017, (b) June 2017, (c) December 2017 and (d) July 2018, the maximal speed contour (see Sect.2.4 is in black line). (e) δT eddy SST anomaly, cold-core in blue and warm-core in red, with black dashed line showing the 5 days smoothed evolution. (f) Maximal speed V_m (dashed blue) and radius R_m (continuous blue) with 10 days smoothing. (g) MLD evolution inside the the anticyclone (dots, with red ones highlighting the closest to center), with outside-eddy background MLD in continuous black line (spread between dashed lines). (h) Brunt-Vaisala frequency.

344

3.1 Horizontal resolution sensitivity

345

The numerical simulation at 4km resolution and 25 vertical levels (run B in Table 1) reveals a few discrepancies with real observations. A horizontal resolution of 4km is close to operational oceanography models in the Mediterranean Sea (Juza et al., 2016). At the surface, despite seasonal variations of the eddy SST signatures (Fig.4a-c) and in the δT index (Fig.4f), summer 'inverse' signatures are not retrieved with no cold-core anticyclone. A steady erosion of the eddy strength is also noticeable, with a decrease in the maximal speed decreasing from $0.35m.s^{-1}$ to $0.15m.s^{-1}$ in 2 years, while its radius remains constant ($\approx 25km$, Fig. 4e). Note that the initial maximal speed is set to $0.4m.s^{-1}$ (see Sect.2.2) but the smoothing effect of time-averaging leads to a lower detected initial value of $0.35m.s^{-1}$.

355

At depth, the mixed layer anomaly is significant, on the order of 50m (Fig.4g). Some bursts of differential mixing are observed in late winter from December to March when mixed layer instabilities and restratification processes can occur, with ξ reaching a few

357

[ht]

Table 1. Summary table of CROCO numerical experiments. Runs start in September of the atmospheric forcing timeseries. Thermal heat flux feedback (THFF), eddy SST anomaly index $\delta\bar{T}$ and differential mixing ratio $\bar{\xi}$ are defined in Sect.2.4, and $\bar{\xi}$ is computed over the upper 20m. Subscripts ($\bar{\xi}_1, \bar{\xi}_2$) refers to first and second summers defined as 230 to 340 days and 590 to 700 days respectively. ΔMLD refers only to the second winter defined as 450 to 590 days (see shades in Fig.4d-h).

Name	Vertical levels	dx (km)	Freq	SST retroaction	THFF ($W.m^{-2}.K^{-1}$)	$\delta\bar{T}_1$ ($^{\circ}C$)	$\delta\bar{T}_2$ ($^{\circ}C$)	$\bar{\xi}_1$	$\bar{\xi}_2$	ΔMLD (m)
1K100-1H	100	1	1-hour	Yes	-41.5 ± 1.3	-0.20 ± 0.10	-0.18 ± 0.04	3.05 ± 0.70	2.81 ± 0.74	51
2K50-1H	50	2	1-hour	Yes	-40.7 ± 1.0	-0.12 ± 0.14	-0.11 ± 0.06	1.54 ± 0.31	1.34 ± 0.22	63
4K25-1H	25	4	1-hour	Yes	-34.3 ± 1.8	0.01 ± 0.14	0.02 ± 0.10	1.10 ± 0.12	1.00 ± 0.12	48
05K150-1H	150	0.5	1-hour	Yes	-39.2 ± 1.4	-0.16 ± 0.10	-0.19 ± 0.06	2.58 ± 0.58	2.71 ± 0.45	91
1K100-1D	100	1	1-day	Yes	-42.1 ± 0.8	-0.21 ± 0.20	-0.31 ± 0.06	2.99 ± 0.44	3.34 ± 1.23	57
1K100-3D	100	1	3-days	Yes	-44.7 ± 1.0	-0.12 ± 0.14	-0.09 ± 0.03	1.41 ± 0.28	0.99 ± 0.09	70
1K100-1W	100	1	1-week	Yes	-41.0 ± 0.4	-0.05 ± 0.05	-0.03 ± 0.01	1.25 ± 0.14	1.02 ± 0.01	94
1K100-1H-NoSST	100	1	1-hour	No	-	-0.41 ± 0.16	-0.51 ± 0.00	2.60 ± 0.46	2.47 ± 0.25	10

358 times values higher than 2 (Fig. 4h). However no differential mixing is retrieved in sum-
359 mer. On the other hand, the anticyclone vertical structure is coarsely reproduced. The
360 winter MLD cooling forms a homogeneous layer between 100 and 150m (Fig. 4i). These
361 winter waters formed by convection do not reproduce the homogeneous subsurface an-
362 ticyclone cores, separated by density jump or sharp temperature gradient such as the
363 continuous temperature gradient in Fig.3h around 200m depth (see other examples in
364 Fig.4-5 from Barboni, Coadou-Chaventon, et al. (2023)). The inability to reproduce this
365 mesoscale subsurface lens is not surprising given the low vertical resolution, the verti-
366 cal steps being on the order of 20m at 100m depth.

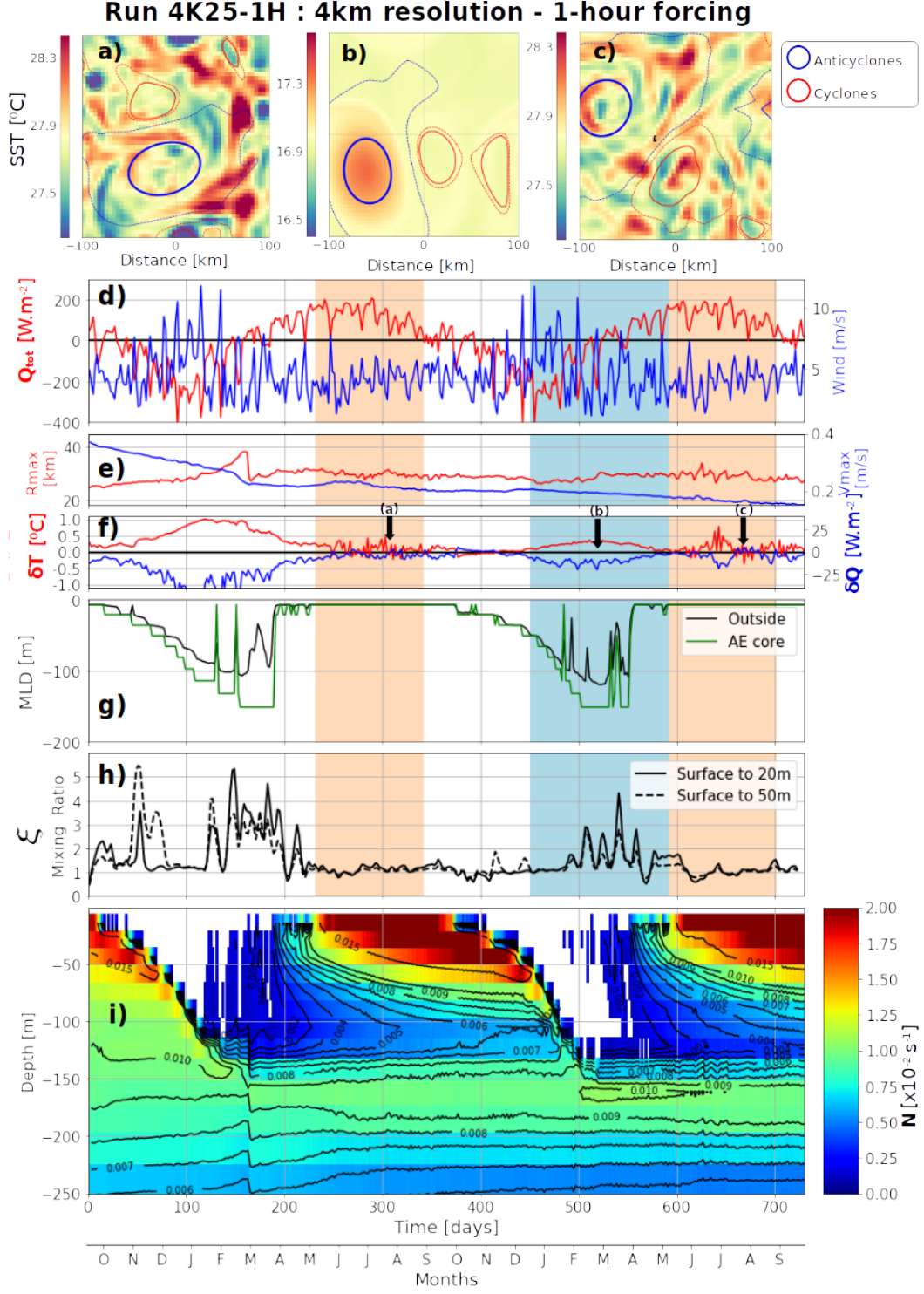


Figure 4. Simulation B from Table 1. (a) SST snapshot in the first summer, (b) in the second winter, (c) in the second summer, with eddies detected by AMEDA in contours. The initial anticyclone is highlighted by a thicker line. (d) Net heat flux (red) and windspeed (blue). (e) $R_m(t)$ (red) and $V_m(t)$ (blue) from AMEDA. (f) SST anomaly index δT (red), respectively heat flux anomaly δQ , blue). (g) Mixed layer inside-eddy (green) and outside-eddy (black). (h) Differential mixing ratio ξ defined in Eq.12 with $h = 20m$ (solid) and $h = 50m$ (dashed line). (i) Inside-eddy stratification evolution shown with Brunt-Vaisala frequency; contours are overlaid with interval $0.001s^{-1}$ and negative values are blanked. On panels c-h, summer periods are indicated by light red shades, winter by a light blue shade.

367 The same numerical set-up with a finer 1km horizontal resolution (run 1K100-1H
 368 in Table 1) shows a net contrast with the previous coarser simulation. This simulation
 369 has a 1km horizontal grid size and 100 levels with same stretching parameters giving ver-
 370 tical grid steps close to 3m in the upper 200m. A summer 'inverse' eddy surface tem-
 371 perature is clearly retrieved with 1-hour frequency heat and momentum forcing. As shown
 372 in Fig.5 in this configuration, a clear anticyclonic cold-core SST signature is observed
 373 in summer (Fig.5a), switching back to a winter warm-core SST the next winter (Fig.5b)
 374 and appearing again in the second summer (Fig.5c). This anticyclone surface seasonal
 375 oscillation can clearly be tracked by δT (Fig.5f). $\overline{\delta T}$ reached about $-0.2^{\circ}C$ in the both
 376 summers (see Table 1) with spikes of $\delta T \approx -0.5^{\circ}C$ and maximal value around $+0.4^{\circ}C$
 377 in winter. Considering anticyclonic cold-core signatures statistics in the Mediterranean
 378 Sea (Moschos et al., 2022) in particular their Fig.5b) $\delta T \approx -0.2^{\circ}C$ is a low but stan-
 379 dard value, anticyclone SST anomalies typically not being colder than $-0.5^{\circ}C$. This cold-
 380 core summer signature goes along with a mixing increase in the upper layers at the eddy
 381 core, measured by a diffusivity in summer more than twice as high inside the eddy core
 382 as outside. Sensibility of the ξ indicator is shown on Fig.5h, with ξ averaged over the
 383 upper 20m or 50m, the first case leading to ξ values higher than 4 in summer despite some
 384 variability. This enhanced mixing seems to be confined in the upper layers, as ξ decreases
 385 to approximately 1 as soon as the mixed layer deepens, but it increases again to simi-
 386 lar values during the second summer.

387 At depth the maximal mixed layer anomaly reaches about 50m (Fig.5h), very close
 388 to the value of the simulation at 4km resolution. However the vertical structure is bet-
 389 ter reproduced at 1km, and in particular between 100 and 150m deep the $5 \times 10^{-3} s^{-1}$
 390 stratification isoline closes in December, 4 months later than in the 4km simulation (in
 391 August, see Fig.4i). This means that homogeneous waters formed at depth in the first
 392 winter re-stratify more slowly. Eddy decay in time is also slower on maximal speed : af-
 393 ter 2 years the anticyclone velocity is about $0.3 m.s^{-1}$ with 1km resolution compared to
 394 $0.15 m.s^{-1}$ with 4km (Fig.4e). Sharp density gradients are smoothed in a coarser sim-
 395 ulation, leading to unrealistic temporal evolution of the anticyclones vertical structure.
 396 Surface (SST) or depth-integrated (maximal geostrophic speed) measurements are then
 397 not accurately reproduced at a spatial resolution of 4km.

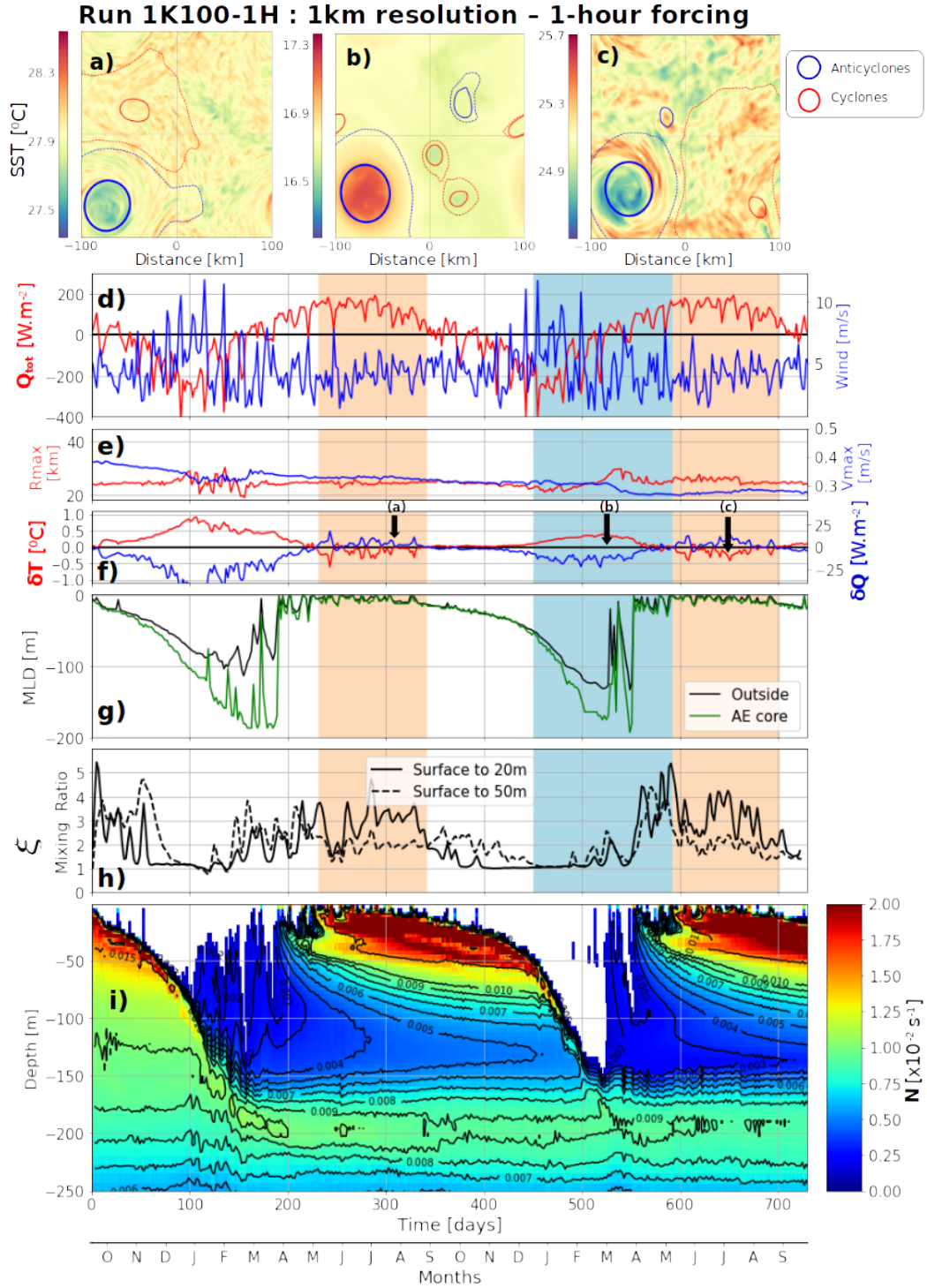


Figure 5. Simulation 1K100-1H from Table1. Same as in Fig.4 but with a 1km horizontal resolution.

398 An experimental series with the same numerical set-up is performed, increasing hori-
 399 zontal resolution from 4km to 500m (runs 1K100-1H, 2K50-1H, 4K25-1H, 05K150-1H)
 400 and vertical resolution accordingly. The horizontal to vertical resolution ratio is kept close
 401 to the Brunt-Vaisala to inertial frequencies ratio. It reveal that summer anticyclonic cold-

402 core signature $\overline{\delta T}$ and differential mixing $\overline{\xi}$ both continuously increase when decreasing
 403 the grid cell (see Fig.6c). Summer eddy SST inversions are then consistently correlated
 404 with an increased mixing. In addition a convergence behavior is observed for mixing at
 405 1km with 100 levels to $\xi \approx 3$, as no further mixing is obtained increasing the resolu-
 406 tion to 500m and 150 levels. Differential mixing appearing at 1km resolution implies that
 407 small scale processes, smaller than the eddy size are at stake. 1km horizontal resolution
 408 with a baroclinic first deformation radius around 11km entails that deformation radius
 409 to be explicitly resolved, which is not entirely effective for resolution of 2km or larger,
 410 similarly to other numerical studies (Marchesiello et al., 2011; Soufflet et al., 2016). On
 411 the other hand in winter very similar δT are retrieved at all resolution, with a maximum
 412 around $+0.4^{\circ}\text{C}$ (Fig.6a) and similar THFF suggesting that winter thermal loss is less af-
 413 fected by horizontal resolution. THFF slightly decreases for lower resolution, likely due
 414 to smoothing effect of strong SST patterns.

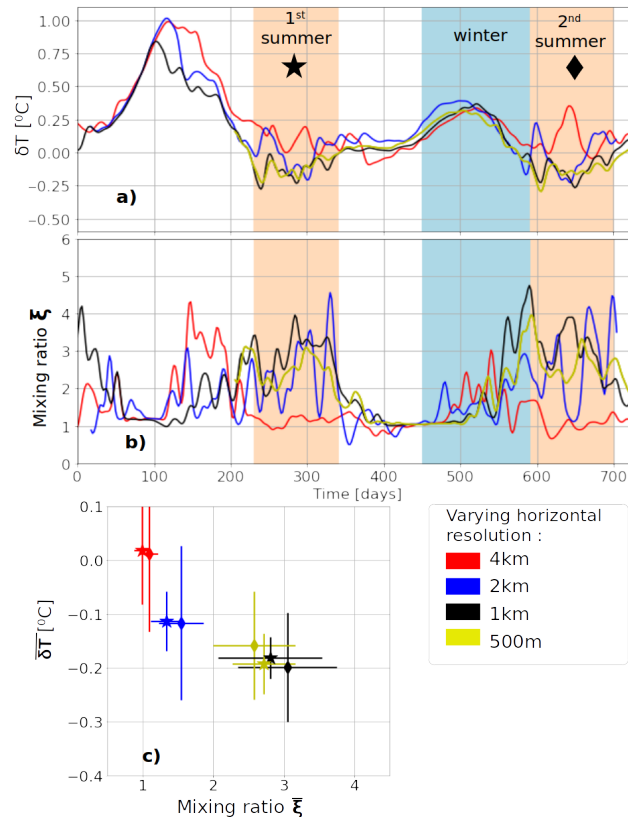


Figure 6. (a) δT and (b) ξ timeseries for experiments 1K100-1H, 2K50-1H, 4K25-1H, 05K150-1H listed in Tab.1 with SST retroaction on air-sea fluxes and varying horizontal resolution frequency. 2-days Gaussian smoothing is applied and summer periods are shaded in light red, winter in light blue. Due to computer memory issues, the first transient winter at 500m resolution was not recorded. (c) Summer-averaged eddy-induced SST anomalies ($\overline{\delta T}$) and mixing ratio ($\overline{\xi}$), with stars for the first summer and diamonds for the second one. Errorbars are ξ spread (30th percentile) over the same period.

415 For the eddy-induced mixed layer anomaly, similar values are obtained from 4km
 416 to 1km resolution ($\Delta MLD \approx 50m$), but a larger $\Delta MLD = 91m$ is retrieved at 500m
 417 resolution. This effect could be due to the partial resolution of sub-mesoscale processes

418 such as mixed layer instabilities (Boccaletti et al., 2007; Capet et al., 2008). Maximal
419 background mixed layer deepens when resolution gets finer down to 1km resolution (see
420 Fig.4g and 5g), in consistence with previous experiments (Couvelard et al., 2015). At
421 500m resolution, a closer look at the MLD evolution inside- and outside-eddy shows that
422 the outside-eddy MLD restratified earlier in run 05K150-1H (in March) than in run 1K100-
423 1H (in April) due to restratification beginning at submesoscale with mixed layer insta-
424 bilities (Fig.7b). But in both cases inside-eddy MLD reached the same depth (193m, see
425 Fig.7e-f). This suggests that maximal mixed layer inside-eddy indeed reached a max-
426 imum driven by air-sea cooling, while restratification outside-eddy occurred too late in
427 run 1K100-1H because vertical buoyancy fluxes are too weak (Capet et al., 2008). Com-
428 pared to Mediterranean MLD climatology, a restratification in April is indeed quite late
429 (Houpert et al., 2015).

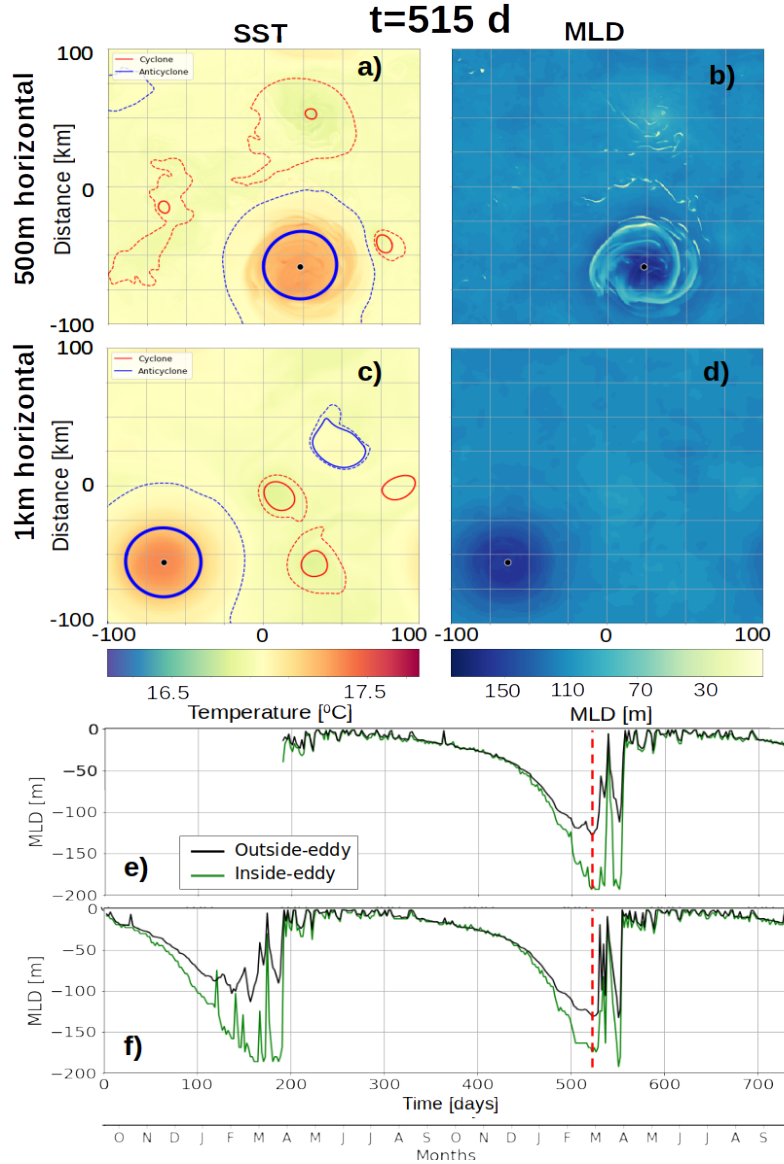


Figure 7. (a) SST with anticyclones and cyclones as in Fig.4 (the initial anticyclone has thicker contour) in 05K150-1H simulation. (b) MLD in 05K150-1H. (c) and (d) : same as (a) and (b) but in 1K100-1H simulation. (e) MLD time series inside-anticyclone (green) and outside-eddy (black) for the 05K150-1H simulation, a red dashed line indicates the time step shown in panels (a)-(d). Due to memory issues, the first transient winter was not recorded. (f) Same as (e) in 1K100-1H simulation.

430 Mixing patterns over the vertical in the 1km resolution simulation are also consistent with observations. Anticyclones were recently observed to enhance mixing at depth
 431 through the propagation of trapped near-inertial internal waves in their core. In studies from Martínez-Marrero et al. (2019) and Fernández-Castro et al. (2020), in situ measurements revealed lower dissipation rate ϵ in anticyclonic homogeneous core than in the
 432 neighboring background, and enhanced ϵ below at depth. In our numerical experiments, both diffusivity κ (Fig.8c) and dissipation rate ϵ (Fig.8e) match this feature, with enhanced mixing in summer below the anticyclone, up to one order of magnitude larger
 433
 434
 435
 436
 437

438 from 200 to 300m depth. The anticyclone subsurface core revealed by thick isopycnal
 439 displacement on Fig.8e, also shows locally reduced ϵ between 100 and 200m. Fig.8e is
 440 then a striking reproduction of dissipation rate section obtained by Fernández-Castro
 441 et al. (2020) (see in particular their Fig.5f). However those in situ measurements could
 442 not compare outside- and inside-eddy mixing close to the surface, because the value range
 443 for ϵ would be too large with surface processes a lot more powerful than deep ocean ones.
 444 Numerical simulation enables to reveal that anticyclones also enhance mixing in near sur-
 445 face, with higher ϵ and κ just above the homogeneous core, in the upper 50 meters. The
 446 differential mixing ratio ξ previously shown in anticyclone time series then accurately
 447 measures a surface-enhanced mixing.

448 The seasonal cycle of eddy SST signature is then effectively reproduced at 1km hor-
 449 izontal resolution, close to observed value for the example shown above (Fig.3e). eddy
 450 SST seasonal shift correlates with increased mixing at the anticyclone core, in consis-
 451 tence with Moschos et al. (2022) hypothesis. This differential mixing is absent at 4km,
 452 but appears through $k - \epsilon$ mixing parametrization and converges at 1km resolution.

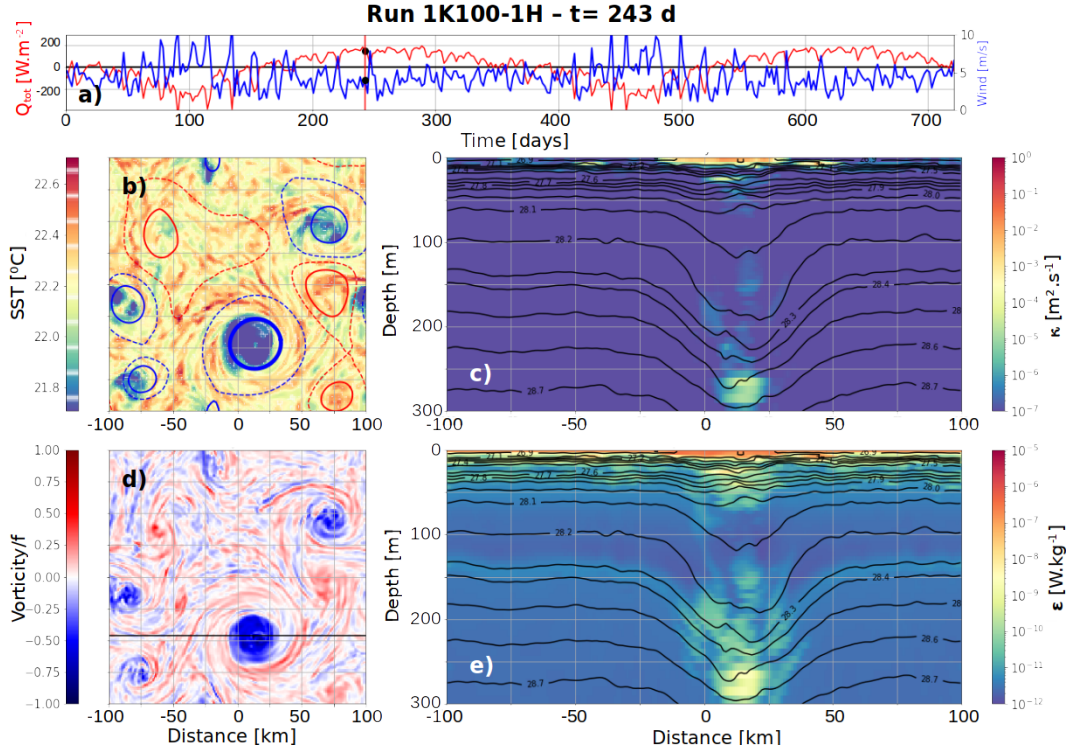


Figure 8. Snapshot at $t = 243 d$ for the 1K100-1H simulation (see Fig.5). (a) Wind speed (blue line) and Q_{tot} (red lines) timeseries. (b) SST and (d) surface vorticity normalized by f with eddy detections as in Fig.4 (initial anticyclone has a thicker contour). (c) κ and (e) ϵ vertical sections in the upper 300m with logarithmic color scales, in both case the colorbar lower bound is the minimal possible value (see Sect.2.1). Isopycnals are added in black lines.

3.2 Forcing frequency sensitivity

453 Sensitivity of the eddy SST signature δT and differential mixing ξ to forcing tem-
 454 poral resolution is investigated by progressively removing high frequencies from the at-
 455 mospheric inputs. These experiences are summarized as 1K100-1D to 1K100-1W in Ta-
 456

457 ble 1, using 1-day, 3-days and 1-week atmospheric timeseries respectively. δT and dif-
 458 ferential mixing ξ timeseries for these experiments are shown in Fig.9a-b. Significantly
 459 cold SST signatures ($\overline{\delta T} \lesssim -0.2^\circ C$) are obtained together with strong mixing ($\bar{\xi} \approx 3$)
 460 for 1-hour and 1-day frequency, but no significant differential mixing is retrieved ($1 <$
 461 $\bar{\xi} < 1.5$) for all lower forcing frequencies (Fig.9c). This threshold behavior is a strong
 462 result and shows that spontaneous appearance of differential mixing is driven by small
 463 scale and high frequency features. With a Coriolis parameter $f = 9.0 \times 10^{-5} s^{-1} =$
 464 $1.24cpd$, the inertial period is about 19h, the 1-day forcing can then partly trigger near-
 465 inertial waves.

466 The relationship between $\overline{\delta T}$ and $\bar{\xi}$ is however less clear than for the resolution sen-
 467 sitivity analysis (Fig.6). No differential mixing is observed for forcing frequencies lower
 468 than 1 day, but summer cold-core signatures are still found ($\overline{\delta T} \gtrsim 0.1^\circ C$, see Table1),
 469 even for the 1-week forcing. δT timeseries clearly show for all frequencies a marked sea-
 470 sonal signal (Fig.6a). In particular a significant warm winter signature is always observed,
 471 with stable maximal value at $\delta T \approx +0.4^\circ C$. In the same context a surprising result is
 472 the summer averaged $\overline{\delta T}$ being colder on average at 1-day than 1-hour forcing, despite
 473 similar differential mixing. Temporal evolution of eddy SST anomalies reveals this ef-
 474 fect to be caused by a larger oscillation of the eddy surface signature (Fig.9a) about $\pm 0.2^\circ C$,
 475 hence larger errorbars at 1-day on Fig.9c. This suggests that other mechanisms not trig-
 476 gered by high frequency winds also contribute to the eddy SST seasonal cycle. If no dif-
 477 ferential vertical mixing is observed but if seasonal variations of the anticyclone SST (and
 478 hence surface density) is found, one can only hypothesize the role of lateral exchanges.
 479 Despite some tries, we were unsuccessful in quantifying eddy lateral exchanges follow-
 480 ing a varying $R_m(t)$ contour. No particular asymmetric wave modes was observed on SST
 481 snapshots, discarding the hypothesis of vortex Rossby waves (Guinn & Schubert, 1993;
 482 Montgomery & Kallenbach, 1997).

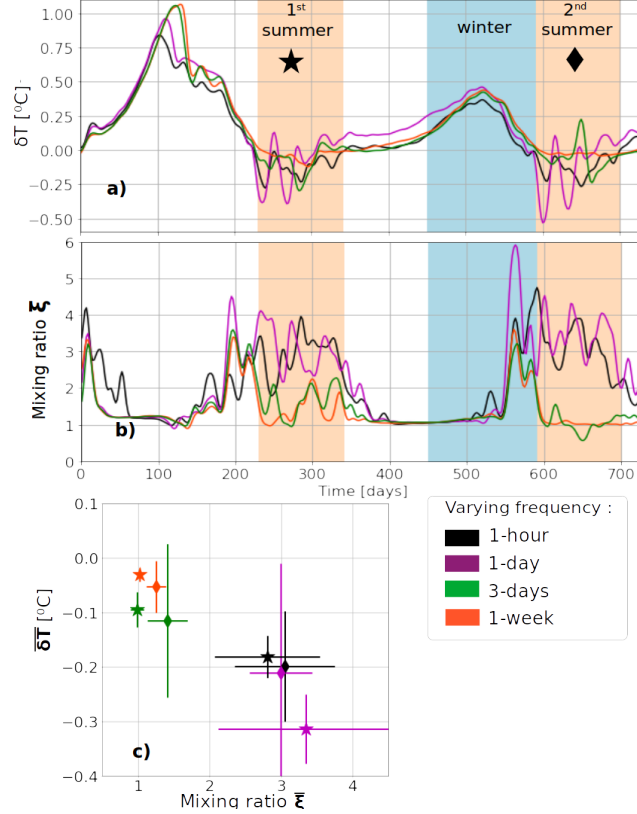


Figure 9. (a) δT and (b) ξ timeseries for experiments 1K100-1H, 1K100-1D, 1K100-3D and 1K100-1W listed in Tab.1 with SST retroaction on air-sea fluxes and varying forcing frequency. 2-days Gaussian smoothing is applied, summer periods are shaded in light red, winter in light blue. (c) Summer-averaged eddy-induced SST anomalies ($\overline{\delta T}$) and mixing ratio ($\overline{\xi}$), with stars for the first summer and diamonds for the second one.

483 Near-inertial internal waves are investigated using Fourier transforms on vertical
 484 speed anomalies in run 1K100-1H. We focus on a single vertical level at 20m in near-surface
 485 where the enhanced mixing occurs (see Fig.8c). Transforms are computed only in the
 486 second summer (590 to 700 simulated days) with a 1-hour sampling frequency. Follow-
 487 ing Babiano et al. (1987), inside-eddy spectrum is performed keeping only the inside-eddy
 488 area (around the eddy center with radius $2/3R_m(t)$) and the remaining area is set to 0
 489 before performing the Fourier transform. Similarly outside-eddy spectrum is performed
 490 blanking all value inside any eddy contours. The results clearly show a differential ef-
 491 fect inside-eddy vertical kinetic energy density revealing a second powerful peak at the
 492 effective inertial frequency $f_e = f + \zeta/2 \approx 1.0cpd$, lower than the inertia frequency
 493 (Fig.10a). Outside-eddy spectrum (Fig.10b) shows only one peak at the inertial frequency,
 494 and internal waves cannot propagate at lower frequencies due to the f -cut-off (Garrett
 495 & Munk, 1972). Normalizing by the investigated area, total vertical kinetic energy per
 496 unit surface is indeed higher inside the anticyclone ($4.19 \times 10^{-14} m^2 \cdot s^{-2} / m^2$) than outside-
 497 eddy ($1.64 \times 10^{-14} m^2 \cdot s^{-2} / m^2$) due to these powerful subinertial internal waves. An as-
 498 sumption of this method is however to assume that both inside- and outside-eddy ar-
 499 eas roughly keep the same area, which is verified. This result is consistent with (Kunze,
 500 1985) theory and recent numerical works (Danioux et al., 2015; Asselin & Young, 2020)
 501 subinertial waves ($\omega \lesssim f$) can be trapped in the anticyclone due to the locally lower
 502 absolute vorticity, and enhance mixing while breaking as proposed by Fernández-Castro
 503 et al. (2020).

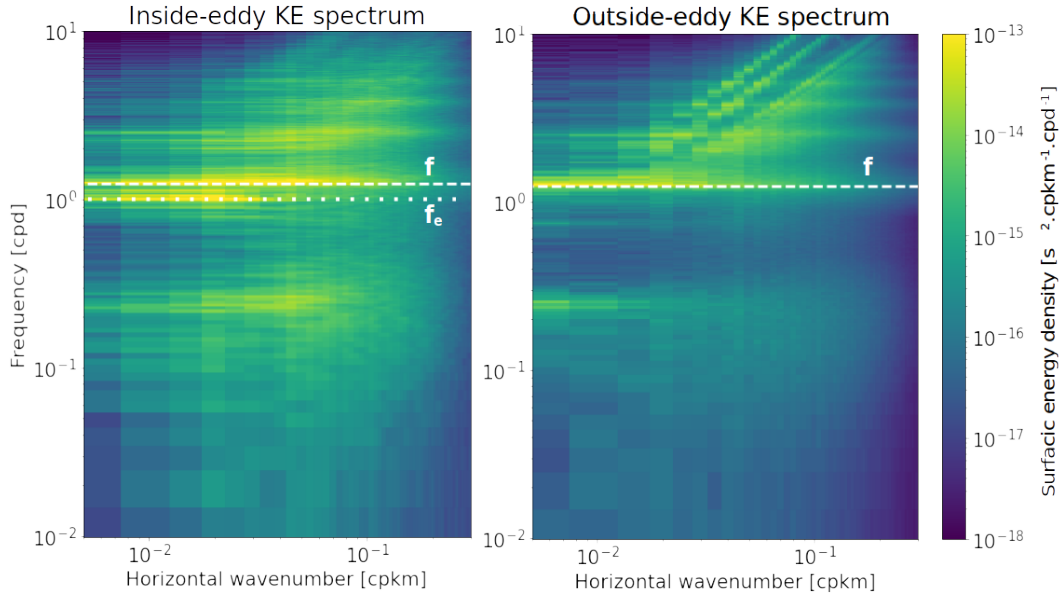


Figure 10. (a) Inside-eddy and (b) outside-eddy vertical kinetic energy density spectrum at 20m depth. For comparison, spectrum are normalized by the area of interest. Analysis performed on simulation 1K100-1H with 1-hour sampling. Normal (respectively effective) inertial frequencies $f = 1.24cpd$ ($f_e \approx 1.0cpd$) are highlighted by a white dashed (dotted) line.

504

3.3 Air-sea fluxes sensitivity

505

506

507

508

509

510

511

512

513

514

515

516

517

Sensitivity of the anticyclone temporal evolution to air-sea fluxes components is further investigated. A $1km$ resolution simulation experiment is run similarly as the 1K100-1H simulation without applying SST retroaction on air-sea fluxes (see Sect.2.3, run 1K100-1H-NoSST in Table 1). Although quite unrealistic, this experiment enables to check if the eddy SST anomaly seasonal shift and differential mixing observed in previous simulations are triggered by air-sea fluxes retroaction. Time series for SST reveals that eddy SST anomalies seasonal oscillation is retrieved without SST retroaction (Fig.11a-c), and summer cold-core signatures are even stronger : $\delta T \approx -0.8^\circ C$ the first summer and $\approx -0.8^\circ C$ the second one (Fig.11f). Simultaneously, differential mixing reaches $\xi \approx 3$, approximately the same value as run 1K100-1H (Fig.11h). This confirms that differential eddy mixing triggering the eddy SST variations is not linked to air-sea fluxes retroaction. However this feedback can modulate and dampen the δT seasonal cycle leading to reduced anomalies.

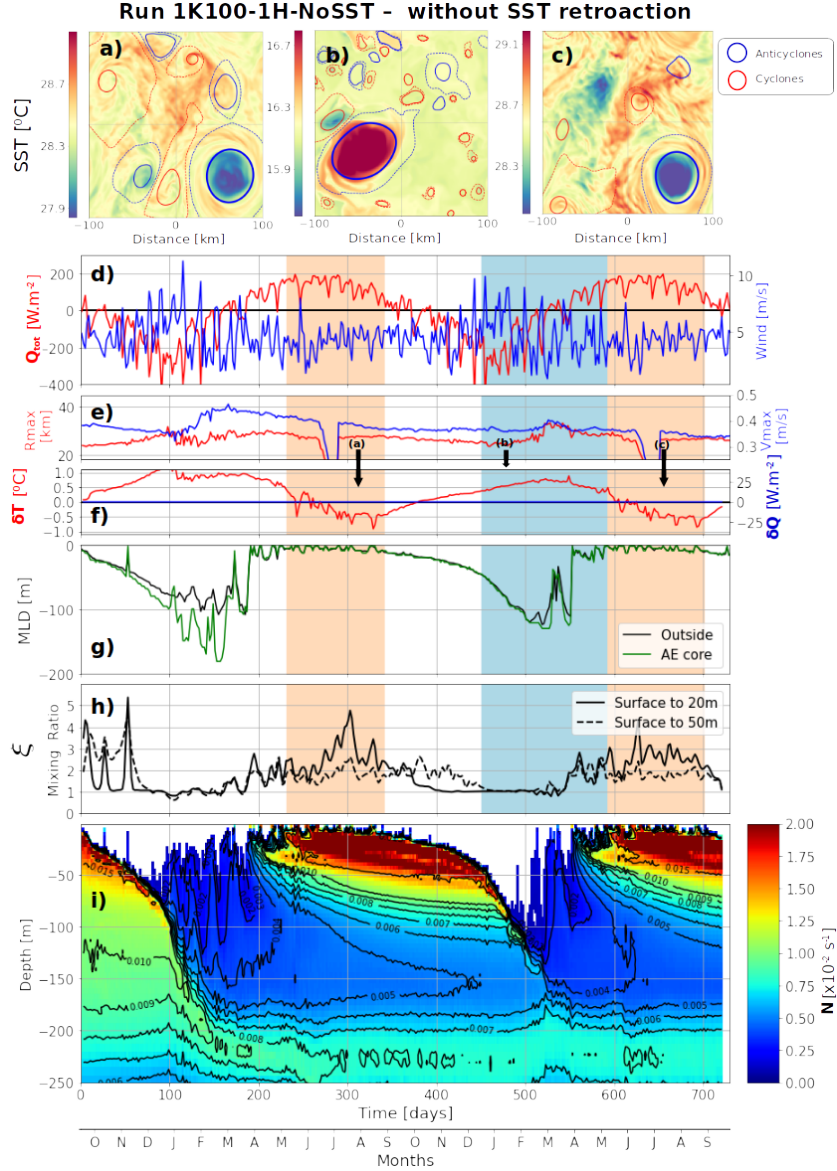


Figure 11. Simulation 1K100-1H-NoSST from Table 1. Same as in Fig.4 but without SST retroaction on air-sea fluxes. Discontinuities in R_{max} and V_{max} in panel (e) are due to the anticyclone crossing twice the grid borders.

518 SST retroaction acting as a negative feedback on SST anomalies can be analyti-
 519 cally expected as linear. The derivative of each heat component with respect to T_s is in-
 520 deed approximately constant (T_s being in Kelvin in Eq.13). Transfer coefficients C_E and
 521 C_S are indeed much more dependent on wind speed than on temperature, varying roughly
 522 about 0.2 with a T_s change of 1K. The most sensitive case is a low air-sea temperature
 523 difference with weak wind, in which the boundary layer can switch from stable to un-
 524 stable conditions (see for instance Fig.A1b from Pettenuzzo et al. (2010)). Assuming C_E
 525 and C_S are roughly constant with respect to temperature one gets :

$$\frac{\partial Q_{LW}^\uparrow}{\partial T_s} = -4\epsilon_{sb}\sigma_{sb}T_s^3 \approx -6 W.m^{-2}.K^{-1} \quad (13)$$

$$\frac{\partial Q_{Lat}}{\partial T_s} \approx -\frac{\rho_a L_E C_E |V| 0.610}{P_{SL}} \frac{dP_{sat}}{dT_s} \approx -3 \times 10^1 W.m^{-2}.K^{-1} \quad (14)$$

$$\frac{\partial Q_{Sen}}{\partial T_s} = -\rho_a c_p C_S |V| \approx -1 \times 10^1 W.m^{-2}.K^{-1} \quad (15)$$

526 Altogether a thermal feedback on the order of $\frac{dQ_{tot}}{dT_s} \approx -4 \times 10^1 W.m^{-2}.K^{-1}$ is
 527 then expected, mostly driven by latent heat flux. THFF in Table 1 is computed only on
 528 the whole simulated year (from 365 to 730 days) and a value of $\approx -40 W.m^{-2}.K^{-1}$ is
 529 retrieved with a simple SST retroaction, in consistence with Eq.13 to 15. This value is
 530 relatively constant in our simulations, slightly decreasing for coarser resolution and lower
 531 forcing frequencies (see Table 1). $\partial C_E/\partial T_s$ and $\partial C_S/\partial T_s$ being also positive, taking this
 532 into account in Eq.14 leads to a even higher THFF estimate. THFF for the 1K100-1H
 533 simulation, defined here as δQ as a function of δT is shown in Fig.12. The obtained ther-
 534 mal feedback is consistent with previous estimates in coupled climate model : Ma et al.
 535 (2016) found a higher THFF ranging between 40 and $56 W.m^{-2}.K^{-1}$ but in the specific
 536 area of very warm eddies of the Kuroshio extension region. Moreton et al. (2021) found
 537 THFF ranging between 35 and $45 W.m^{-2}.K^{-1}$ over mesoscale eddies. They however used
 538 a composite approach in a model coupled with atmosphere and maximal oceanic reso-
 539 lution of $1/12^\circ$, for effective radius about $40km$. A coupled atmosphere layer is expected
 540 to further dampen the total THFF, taking into account other feedbacks than SST, in
 541 particular evaporation. Humidity is expected to increase over warm eddy, consequently
 542 decreasing the latent heat flux driving evaporation, whereas we applied a uniform h_{2m}
 543 field. Similar THFF in our simulations compared to coupled ocean-atmosphere models
 544 suggests that our results would not change significantly with more complex heat flux retroac-
 545 tion.

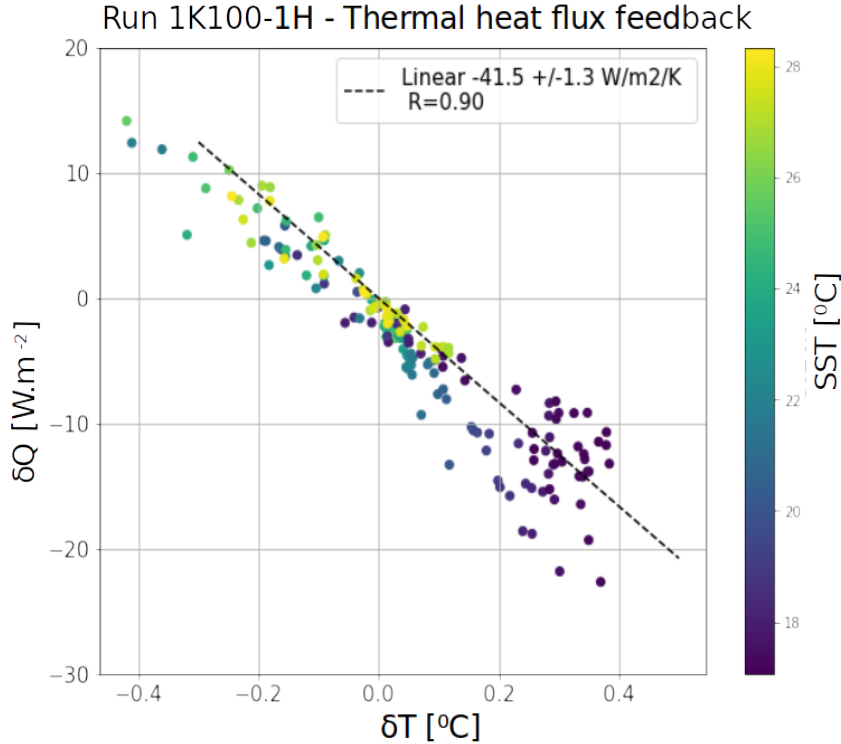


Figure 12. Thermal heat flux feedback in run 1K100-1H on the 2nd simulated year, with linear regression as dashed black line, δQ and δT are from Fig.5f. Regression coefficient and parameters are indicated in the legend.

546 Without SST retroaction on air-sea fluxes, the most important difference from run
 547 1K100-1H is the MLD anomaly variations. Outside-eddy, mixed layer evolution is very
 548 similar in runs 1K100-1H and 1K100-1H-NoSST reaching about 100m at its winter max-
 549 imum, but the eddy MLD anomaly is an order of magnitude smaller ($\Delta MLD = 10m$,
 550 see Fig.11h). With no THFF, the MLD deepens at the same rate outside- and inside-
 551 eddy. Winter MLD deepening can be computed estimating the thermal loss ΔT , assum-
 552 ing a linear thermal linear stratification $\partial_z T$:

$$MLD = \frac{\Delta T}{\partial_z T} \quad (16)$$

553 The thermal loss is the integration of the heat flux over winter duration D . Assum-
 554 ing stratification is at first order the same outside- and inside-eddy, MLD anomaly is then
 555 driven by heat flux lateral gradients :

$$\Delta MLD = \frac{D}{\rho_0 c_p \partial_z T} \delta Q \quad (17)$$

556 In the 1K100-1H with SST retroaction on air-sea fluxes, δQ is positive in winter
 557 reaching about $+15W.m^{-2}$ over 4 months. This leads to an estimate $\Delta MLD \approx 2 \times$
 558 $10^1 m$. This estimate should then be the eddy MLD anomaly contribution from THFF
 559 alone, but a lot higher difference is obtained between run 1K100-1H and 1K100-1H-NoSST.
 560 The main assumption in Eq.17 is that $\partial_z T$ is roughly the same inside- and outside-eddy.
 561 This is true in the upper layers where stratification is mostly the seasonal thermocline
 562 (see isopycnals in Fig.8c-d). At depth lower than 100m however, the anticyclone consti-
 563 tutes a more homogenized layer and this assumption should not hold as MLD should deepen
 564 faster inside-eddy, even with no SST retroaction. The very low ΔMLD found with no
 565 THFF then suggests that thermal feedback may also impact inside-eddy stratification.
 566 An example of inside-eddy MLD faster deepening is shown in Fig.3g : the MLD connects
 567 in February 2018 with the layer homogenized the previous winter and reaching quickly
 568 about 300m. Such mixed layer deepening acceleration is partly retrieved in run 1K100-
 569 1H around 500 days, with a MLD jump of about 30m (Fig.5g) inside-eddy but only about
 570 10m outside-eddy. This coincides with the mixing of the subsurface homogenized layer
 571 formed in the first winter, despite diffusion (stratification isolines progressively closing,
 572 Fig. 5i) as discussed earlier.

573 ΔMLD is however still relatively weak compared to the 200 to 300m MLD anoma-
 574 lies observed in Mediterranean anticyclones (Barboni, Coadou-Chaventon, et al., 2023).
 575 Two main hypotheses can be proposed, the first being that some interannual variabil-
 576 ity is needed. The second hypothesis is that layers homogenized by winter MLD progres-
 577 sively restratify at depth in summer due to numerical diffusion. MLD in the following
 578 winter will then have to break this numerical stratification. This second hypothesis en-
 579 tails that the vertical grid is not enough refined yet to correctly preserve homogenized
 580 layers from one winter to another. From the comparison between runs 1K100-1H and
 581 1K100-1H-NoSST shows that SST retroaction on air-sea fluxes is necessary to obtained
 582 eddy MLD anomalies, but quantitative description deserves further research and ΔMLD
 583 is not only driven by fluxes gradients at the eddy scale.

584 Conclusions

585 Idealized numerical experiment at high horizontal resolution and high frequency
 586 atmospheric forcing are able to qualitatively and quantitatively retrieve SST signature
 587 seasonal cycle for a mesoscale anticyclone. Starting from a surface intensified mesoscale
 588 anticyclone at $Ro \approx 0.16$, seasonal oscillations of the eddy SST anomalies are recov-
 589 ered with an 1km resolution, hourly atmospheric forcing and SST retroaction on air-sea

590 fluxes. Retrieved eddy anomalies are a warm winter SST feature at $\delta T \approx +0.5^\circ C$ and
 591 a cold summer SST at $\delta T \approx -0.2^\circ C$, in consistence with in situ observations. The shift
 592 from warm winter SST signature to summer cold one is partly explained by an increased
 593 vertical mixing in the anticyclone upper layers. This differential mixing is due to higher
 594 NIW energy propagation well captured through the $\kappa - \epsilon$ mixing parametrization.

595 A sensitivity analysis reveals that this differential mixing depends on the grid res-
 596 olution. Model diffusivity near the surface is then consistently 3 times higher in sum-
 597 mer inside-eddy than outside for horizontal resolution of 1km or smaller. This resolu-
 598 tion corresponds to an explicitly resolved first baroclinic deformation radius. Sensitiv-
 599 ity to the forcing frequency is investigated by progressively removing high frequencies
 600 from the atmospheric input fields. A threshold behavior is observed when forcing fre-
 601 quency is lower than a day, then differential mixing dramatically vanishes with no sig-
 602 nificant summer cold-core anticyclonic SST. Vertical kinetic energy signing internal wave
 603 propagation indeed reveals a second powerful peak at $\omega = 1.0cpd$ inside the anticyclone
 604 in near-surface, corresponding to the effective inertial frequency and responding to high
 605 frequency forcing. This peak is absent outside-eddy because the cut-off inertia frequency
 606 $f = 1.24cpd$ is higher. Such an analysis suggests a significant impact of the eddy vort-
 607 icity as cut-off frequency in allowing or not the selective NIW propagation. Weaker eddy
 608 SST seasonal oscillations are also retrieved in the absence of high frequently forcing and
 609 consequently without differential mixing (3-days and 1-week experiments). This high-
 610 lights that other contributions might participate to these eddy SST signatures, in par-
 611 ticular lateral exchanges. A new question for future research opened by this eddy-modulated
 612 mixing is how it depends on the eddy vorticity and size.

613 SST retroaction on air-sea fluxes is not found to be responsible of eddy SST sig-
 614 natures seasonal shift, as the seasonal oscillation is retrieved with and without air-sea
 615 fluxes parametrization. However this retroaction is logically found to dampen the SST
 616 anomalies, and then reduces eddy anomalies magnitude in both summer and winter. The
 617 average thermal heat flux feedback of our mesoscale anticyclone is approximately $40W.m^{-2}.K^{-1}$,
 618 in consistence with analytical derivation and previous studies.

619 Significant eddy-induced mixed layer anomaly $\Delta MLD \approx 50m$ are found at 1km
 620 horizontal resolution, only in the presence of SST retroaction on fluxes. Linear MLD anomaly
 621 analysis suggests that the thermal feedback is only responsible for about half of the MLD
 622 anomaly. Further analysis should then investigate how SST retroaction impacts inside-
 623 eddy stratification. MLD anomalies do not completely converge at 1km as larger anoma-
 624 lies are obtained with a 500m resolution due to restratification beginning outside-eddy
 625 driven by submesoscale instabilities, despite similar maximal mixed-layer at the anticy-
 626 clone core. No restratification delay is clearly observed, but it could occur at even higher
 627 resolution inside the anticyclone because the balanced density gradients inhibits mixed
 628 layer instabilities there. This hypothesis is consistent with observations (Barboni, Coadou-
 629 Chaventon, et al., 2023) but would deserve more investigation in the future. This result
 630 is also important as the mixed layer is a significant driver of atmospheric and bio-geochemical
 631 exchanges, and the explicit resolution of submesoscale processes might be needed to ac-
 632 curately reproduce their interaction with eddies (Capet et al., 2008; Lévy et al., 2018).
 633 An important result is still that significant ΔMLD is retrieved only when SST exerts
 634 a retroaction on air-sea fluxes, but the quantitative description of its evolution would de-
 635 serve more analysis.

636 This is the first time that subinertial waves concentration in anticyclones is linked
 637 to an increased mixing in near surface, spontaneously retrieved through the $k-\epsilon$ mix-
 638 ing closure. Mixing modulation by eddies suggests a strong scale interactions between
 639 subinertial internal waves ($\omega \lesssim f$) and the mesoscale ($\omega \ll f$). Differential mixing trig-
 640 gered by high frequency winds is an important result highlighting the need of both fine
 641 resolution and atmospheric forcing at sufficiently high frequency to correctly reproduce
 642 mesoscale eddies evolution. At present stage, global operational models do not have the

643 spatial resolution to capture these phenomena. According to this study, 1/120 °resolution
 644 with 100 vertical levels would then be necessary to reproduce accurately mesoscale tem-
 645 poral evolution.

646 Open Research Section

647 In-situ profiles colocalized with mesoscale eddies database is available at <https://doi.org/10.17882/93077>. AMEDA eddy tracking algorithm is open source and avail-
 648 able at <https://github.com/briaclevu/AMEDA>. ERA5 atmospheric reanalysis are pub-
 649 650 licly available at <https://doi.org/10.24381/cds.adbb2d47>. The CROCO code is pub-
 651 licly available at <https://www.croco-ocean.org/>.

652 Acknowledgments

653 Authors gratefully acknowledge *Ifremer* and *Service Hydrographique et Océanographique de la Marine*
 654 *de la Marine* for their use of the *Datarmor* computing facility. Authors acknowledge Evan-
 655 gelos Moschos (*Amphitrite*) for the reuse of his figures as snapshots in Fig.3a-d. Authors
 656 also acknowledge fruitful discussions with Clément Vic (*Ifremer*), in particular the com-
 657 parison with observations in Fig.8 and 10.

658 References

- 659 Amores, A., Jordà, G., Arsouze, T., & Le Sommer, J. (2018). Up to what extent can
 660 we characterize ocean eddies using present-day gridded altimetric products?
 661 *Journal of Geophysical Research: Oceans*, *123*(10), 7220–7236.
- 662 Arai, M., & Yamagata, T. (1994). Asymmetric evolution of eddies in rotating shal-
 663 low water. *Chaos: An Interdisciplinary Journal of Nonlinear Science*, *4*(2),
 664 163–175.
- 665 Aroucha, L. C., Veleza, D., Lopes, F. S., Tyaquicã, P., Lefèvre, N., & Araujo, M.
 666 (2020). Intra- and inter-annual variability of north brazil current rings us-
 667 ing angular momentum eddy detection and tracking algorithm: Observa-
 668 tions from 1993 to 2016. *Journal of Geophysical Research: Oceans*, *125*(12),
 669 e2019JC015921. doi: <https://doi.org/10.1029/2019JC015921>
- 670 Asselin, O., & Young, W. R. (2020). Penetration of wind-generated near-inertial
 671 waves into a turbulent ocean. *Journal of Physical Oceanography*, *50*(6), 1699–
 672 1716.
- 673 Ayouche, A., De Marez, C., Morvan, M., L’hegaret, P., Carton, X., Le Vu, B., &
 674 Stegner, A. (2021). Structure and dynamics of the ras al hadd oceanic dipole
 675 in the arabian sea. In *Oceans* (Vol. 2, pp. 105–125).
- 676 Babiano, A., Basdevant, C., Legras, B., & Sadourny, R. (1987). Vorticity and
 677 passive-scalar dynamics in two-dimensional turbulence. *Journal of Fluid Me-*
 678 *chanics*, *183*, 379–397.
- 679 Barboni, A., Coadou-Chaventon, S., Stegner, A., Le Vu, B., & Dumas, F. (2023).
 680 How subsurface and double-core anticyclones intensify the winter mixed-layer
 681 deepening in the mediterranean sea. *Ocean Science*, *19*(2), 229–250.
- 682 Barboni, A., Lazar, A., Stegner, A., & Moschos, E. (2021). Lagrangian eddy track-
 683 ing reveals the eratosthenes anticyclonic attractor in the eastern levantine
 684 basin. *Ocean Science*, *17*(5), 1231–1250.
- 685 Barboni, A., Stegner, A., Le Vu, B., & Dumas, F. (2023). *2000-2021 in situ pro-*
 686 *files colocalized with ameda eddy detections from 1/8 aviso altimetry in the*
 687 *mediterranean sea*. SEANOE.
- 688 Boccaletti, G., Ferrari, R., & Fox-Kemper, B. (2007). Mixed layer instabilities and
 689 restratification. *Journal of Physical Oceanography*, *37*(9), 2228–2250.
- 690 Capet, X., McWilliams, J. C., Molemaker, M. J., & Shchepetkin, A. F. (2008).
 691 Mesoscale to submesoscale transition in the california current system. part i:

- 692 Flow structure, eddy flux, and observational tests. *Journal of physical oceanog-*
693 *raphy*, *38*(1), 29–43.
- 694 Carton, X., Flierl, G., & Polvani, L. (1989). The generation of tripoles from unsta-
695 ble axisymmetric isolated vortex structures. *EPL (Europhysics Letters)*, *9*(4),
696 339.
- 697 Chaigneau, A., Eldin, G., & Dewitte, B. (2009). Eddy activity in the four major
698 upwelling systems from satellite altimetry (1992–2007). *Progress in Oceanogra-*
699 *phy*, *83*(1-4), 117–123.
- 700 Chelton, D. B., Gaube, P., Schlax, M. G., Early, J. J., & Samelson, R. M. (2011).
701 The influence of nonlinear mesoscale eddies on near-surface oceanic chloro-
702 phyll. *Science*, *334*(6054), 328–332.
- 703 Chelton, D. B., Schlax, M. G., & Samelson, R. M. (2011). Global observations of
704 nonlinear mesoscale eddies. *Progress in oceanography*, *91*(2), 167–216.
- 705 Chelton, D. B., Schlax, M. G., Samelson, R. M., & de Szoeke, R. A. (2007). Global
706 observations of large oceanic eddies. *Geophysical Research Letters*, *34*(15).
- 707 Couvelard, X., Dumas, F., Garnier, V., Ponte, A., Talandier, C., & Treguier, A.-M.
708 (2015). Mixed layer formation and restratification in presence of mesoscale and
709 submesoscale turbulence. *Ocean Modelling*, *96*, 243–253.
- 710 Danioux, E., Klein, P., & Rivière, P. (2008). Propagation of wind energy into the
711 deep ocean through a fully turbulent mesoscale eddy field. *Journal of Physical*
712 *Oceanography*, *38*(10), 2224–2241.
- 713 Danioux, E., Vanneste, J., & Bühler, O. (2015). On the concentration of near-
714 inertial waves in anticyclones. *Journal of Fluid Mechanics*, *773*, R2.
- 715 D’Asaro, E. A. (1995). Upper-ocean inertial currents forced by a strong storm.
716 part iii: Interaction of inertial currents and mesoscale eddies. *Journal of physi-*
717 *cal oceanography*, *25*(11), 2953–2958.
- 718 de Marez, C., Le Corre, M., & Gula, J. (2021). The influence of merger and con-
719 vection on an anticyclonic eddy trapped in a bowl. *Ocean Modelling*, *167*,
720 101874.
- 721 Doglioli, A., Blanke, B., Speich, S., & Lapeyre, G. (2007). Tracking coherent struc-
722 tures in a regional ocean model with wavelet analysis: Application to cape
723 basin eddies. *Journal of Geophysical Research: Oceans*, *112*(C5).
- 724 Escudier, R., Renault, L., Pascual, A., Brasseur, P., Chelton, D., & Beuvier, J.
725 (2016). Eddy properties in the western mediterranean sea from satellite alti-
726 metry and a numerical simulation. *Journal of Geophysical Research: Oceans*,
727 *121*(6), 3990–4006.
- 728 Everett, J., Baird, M., Oke, P., & Suthers, I. (2012). An avenue of eddies: Quantify-
729 ing the biophysical properties of mesoscale eddies in the tasman sea. *Geophysi-*
730 *cal Research Letters*, *39*(16).
- 731 Fairall, C. W., Bradley, E. F., Hare, J., Grachev, A. A., & Edson, J. B. (2003).
732 Bulk parameterization of air–sea fluxes: Updates and verification for the coare
733 algorithm. *Journal of climate*, *16*(4), 571–591.
- 734 Fernández-Castro, B., Evans, D. G., Frajka-Williams, E., Vic, C., & Naveira-
735 Garabato, A. C. (2020). Breaking of internal waves and turbulent dissipation
736 in an anticyclonic mode water eddy. *Journal of Physical Oceanography*, *50*(7),
737 1893–1914.
- 738 Frenger, I., Gruber, N., Knutti, R., & Münnich, M. (2013). Imprint of southern
739 ocean eddies on winds, clouds and rainfall. *Nature geoscience*, *6*(8), 608–612.
- 740 Garrett, C., & Munk, W. (1972). Space-time scales of internal waves. *Geophysical*
741 *Fluid Dynamics*, *3*(3), 225–264.
- 742 Gaube, P., J. McGillicuddy Jr, D., & Moulin, A. J. (2019). Mesoscale eddies mod-
743 ulate mixed layer depth globally. *Geophysical Research Letters*, *46*(3), 1505–
744 1512.
- 745 Graves, L. P., McWilliams, J. C., & Montgomery, M. T. (2006). Vortex evolution
746 due to straining: A mechanism for dominance of strong, interior anticyclones.

- 747 *Geophysical and Astrophysical Fluid Dynamics*, 100(3), 151–183.
- 748 Guinn, T. A., & Schubert, W. H. (1993). Hurricane spiral bands. *Journal of the at-*
749 *mospheric sciences*, 50(20), 3380–3403.
- 750 Hausmann, U., & Czaja, A. (2012). The observed signature of mesoscale eddies in
751 sea surface temperature and the associated heat transport. *Deep Sea Research*
752 *Part I: Oceanographic Research Papers*, 70, 60–72.
- 753 Hersbach, H., Bell, B., Berrisford, P., Hirahara, S., Horányi, A., Muñoz-Sabater, J.,
754 ... others (2020). The era5 global reanalysis. *Quarterly Journal of the Royal*
755 *Meteorological Society*, 146(730), 1999–2049.
- 756 Houpert, L., Testor, P., De Madron, X. D., Somot, S., D’ortenzio, F., Estournel, C.,
757 & Lavigne, H. (2015). Seasonal cycle of the mixed layer, the seasonal thermo-
758 cline and the upper-ocean heat storage rate in the mediterranean sea derived
759 from observations. *Progress in Oceanography*, 132, 333–352.
- 760 Ioannou, A., Stegner, A., Dubos, T., Le Vu, B., & Speich, S. (2020). Generation
761 and intensification of mesoscale anticyclones by orographic wind jets: The case
762 of ierapetra eddies forced by the etesians. *Journal of Geophysical Research:*
763 *Oceans*, 125(8), e2019JC015810.
- 764 Ioannou, A., Stegner, A., & Dumas, F. (2021). Three-dimensional evolution of
765 mesoscale anticyclones in the lee of crete. *Frontiers in Marine Science*.
- 766 Ioannou, A., Stegner, A., Tuel, A., LeVu, B., Dumas, F., & Speich, S. (2019). Cy-
767 clostrophic corrections of aviso/duacs surface velocities and its application to
768 mesoscale eddies in the mediterranean sea. *Journal of Geophysical Research:*
769 *Oceans*, 124(12), 8913–8932.
- 770 Itoh, S., & Yasuda, I. (2010). Characteristics of mesoscale eddies in the kuroshio-
771 oyashio extension region detected from the distribution of the sea surface
772 height anomaly. *Journal of Physical Oceanography*, 40(5), 1018–1034.
- 773 Juza, M., Mourre, B., Renault, L., Gómara, S., Sebastián, K., Lora, S., ... others
774 (2016). Socib operational ocean forecasting system and multi-platform valida-
775 tion in the western mediterranean sea. *Journal of Operational Oceanography*,
776 9(sup1), s155–s166.
- 777 Kunze, E. (1985). Near-inertial wave propagation in geostrophic shear. *Journal of*
778 *Physical Oceanography*, 15(5), 544–565.
- 779 Laxenaire, R., Speich, S., Blanke, B., Chaigneau, A., Pegliasco, C., & Stegner, A.
780 (2018). Anticyclonic eddies connecting the western boundaries of indian and
781 atlantic oceans. *Journal of Geophysical Research: Oceans*, 123(11), 7651–
782 7677.
- 783 Laxenaire, R., Speich, S., & Stegner, A. (2020). Agulhas ring heat content and
784 transport in the south atlantic estimated by combining satellite altimetry and
785 argo profiling floats data. *Journal of Geophysical Research: Oceans*, 125(9),
786 e2019JC015511.
- 787 Le Vu, B., Stegner, A., & Arsouze, T. (2018). Angular momentum eddy detection
788 and tracking algorithm (amedea) and its application to coastal eddy formation.
789 *Journal of Atmospheric and Oceanic Technology*, 35(4), 739–762.
- 790 Lévy, M., Franks, P. J., & Smith, K. S. (2018). The role of submesoscale currents in
791 structuring marine ecosystems. *Nature communications*, 9(1), 4758.
- 792 Liu, F., Zhou, H., Huang, W., & Wen, B. (2020). Submesoscale eddies observation
793 using high-frequency radars: A case study in the northern south china sea.
794 *IEEE Journal of Oceanic Engineering*, 46(2), 624–633.
- 795 Liu, Y., Zheng, Q., & Li, X. (2021). Characteristics of global ocean abnormal
796 mesoscale eddies derived from the fusion of sea surface height and temperature
797 data by deep learning. *Geophysical Research Letters*, 48(17), e2021GL094772.
- 798 Ma, X., Jing, Z., Chang, P., Liu, X., Montuoro, R., Small, R. J., ... others (2016).
799 Western boundary currents regulated by interaction between ocean eddies and
800 the atmosphere. *Nature*, 535(7613), 533–537.
- 801 Marchesiello, P., Capet, X., Menkes, C., & Kennan, S. C. (2011). Submesoscale dy-

- 802 namics in tropical instability waves. *Ocean Modelling*, 39(1-2), 31–46.
- 803 Mariotti, A. (2010). Recent changes in the mediterranean water cycle: a pathway
804 toward long-term regional hydroclimatic change? *Journal of Climate*, 23(6),
805 1513–1525.
- 806 Martínez-Marrero, A., Barceló-Llull, B., Pallàs-Sanz, E., Aguiar-González, B.,
807 Gordo, C., Grisolia, D., . . . Arístegui, J. (2019). Near-inertial wave trapping
808 near the base of an anticyclonic mesoscale eddy under normal atmospheric
809 conditions. *Journal of Geophysical Research: Oceans*, 124(11), 8455–8467.
- 810 Mason, E., Pascual, A., & McWilliams, J. C. (2014). A new sea surface height–based
811 code for oceanic mesoscale eddy tracking. *Journal of Atmospheric and Oceanic
812 Technology*, 31(5), 1181–1188.
- 813 Mason, E., Ruiz, S., Bourdalle-Badie, R., Reffray, G., García-Sotillo, M., & Pascual,
814 A. (2019). New insight into 3-d mesoscale eddy properties from cmems opera-
815 tional models in the western mediterranean. *Ocean Science*, 15(4), 1111–1131.
- 816 Mkhinini, N., Coimbra, A. L. S., Stegner, A., Arsouze, T., Taupier-Letage, I., &
817 Béranger, K. (2014). Long-lived mesoscale eddies in the eastern mediterranean
818 sea: Analysis of 20 years of aviso geostrophic velocities. *Journal of Geophysical
819 Research: Oceans*, 119(12), 8603–8626.
- 820 Montgomery, M. T., & Kallenbach, R. J. (1997). A theory for vortex rossby-waves
821 and its application to spiral bands and intensity changes in hurricanes. *Quar-
822 terly Journal of the Royal Meteorological Society*, 123(538), 435–465.
- 823 Moreton, S., Ferreira, D., Roberts, M., & Hewitt, H. (2021). Air-sea turbulent heat
824 flux feedback over mesoscale eddies. *Geophysical Research Letters*, 48(20),
825 e2021GL095407.
- 826 Moschos, E., Barboni, A., & Stegner, A. (2022). Why do inverse eddy surface tem-
827 perature anomalies emerge? the case of the mediterranean sea. *Remote Sens-
828 ing*, 14(15), 3807.
- 829 Nencioli, F., Dong, C., Dickey, T., Washburn, L., & McWilliams, J. C. (2010).
830 A vector geometry–based eddy detection algorithm and its application to a
831 high-resolution numerical model product and high-frequency radar surface
832 velocities in the southern california bight. *Journal of atmospheric and oceanic
833 technology*, 27(3), 564–579.
- 834 Olson, D. B., & Evans, R. H. (1986). Rings of the agulhas current. *Deep Sea Re-
835 search Part A. Oceanographic Research Papers*, 33(1), 27–42.
- 836 Paulson, C. A., & Simpson, J. J. (1977). Irradiance measurements in the upper
837 ocean. *Journal of Physical Oceanography*, 7(6), 952–956.
- 838 Penven, P., Halo, I., Pous, S., & Marié, L. (2014). Cyclogeostrophic balance in the
839 mozambique channel. *Journal of Geophysical Research: Oceans*, 119(2), 1054–
840 1067.
- 841 Perfect, B., Kumar, N., & Riley, J. (2020). Energetics of seamount wakes. part i:
842 Energy exchange. *Journal of Physical Oceanography*, 50(5), 1365–1382.
- 843 Perret, G., Stegner, A., Farge, M., & Pichon, T. (2006). Cyclone-anticyclone asym-
844 metry of large-scale wakes in the laboratory. *Physics of Fluids*, 18(3).
- 845 Pessini, F., Olita, A., Cotroneo, Y., & Perilli, A. (2018). Mesoscale eddies in the
846 algerian basin: do they differ as a function of their formation site? *Ocean Sci-
847 ence*, 14(4), 669–688.
- 848 Pettenuzzo, D., Large, W., & Pinardi, N. (2010). On the corrections of era-40 sur-
849 face flux products consistent with the mediterranean heat and water budgets
850 and the connection between basin surface total heat flux and nao. *Journal of
851 Geophysical Research: Oceans*, 115(C6).
- 852 Richardson, P. L. (1980). Gulf stream ring trajectories. *Journal of Physical
853 Oceanography*, 10(1), 90–104.
- 854 Rodi, W. (1987). Examples of calculation methods for flow and mixing in stratified
855 fluids. *Journal of Geophysical Research: Oceans*, 92(C5), 5305–5328. doi: 10
856 .1029/JC092iC05p05305

- 857 Shchepetkin, A. F., & McWilliams, J. C. (2005). The regional oceanic modeling
 858 system (roms): a split-explicit, free-surface, topography-following-coordinate
 859 oceanic model. *Ocean modelling*, *9*(4), 347–404.
- 860 Smith, W. H., & Sandwell, D. T. (1997). Global sea floor topography from satellite
 861 altimetry and ship depth soundings. *Science*, *277*(5334), 1956–1962.
- 862 Soufflet, Y., Marchesiello, P., Lemarié, F., Jouanno, J., Capet, X., Debreu, L., &
 863 Benschila, R. (2016). On effective resolution in ocean models. *Ocean Modelling*,
 864 *98*, 36–50.
- 865 Stegner, A., & Dritschel, D. (2000). A numerical investigation of the stability of iso-
 866 lated shallow water vortices. *Journal of Physical Oceanography*, *30*(10), 2562–
 867 2573.
- 868 Stegner, A., Le Vu, B., Dumas, F., Ghannami, M. A., Nicolle, A., Durand, C., &
 869 Faugere, Y. (2021). Cyclone-anticyclone asymmetry of eddy detection on
 870 gridded altimetry product in the mediterranean sea. *Journal of Geophysical*
 871 *Research: Oceans*, *126*(9), e2021JC017475.
- 872 Steinberg, J. M., Cole, S. T., Drushka, K., & Abernathey, R. P. (2022). Seasonality
 873 of the mesoscale inverse cascade as inferred from global scale-dependent eddy
 874 energy observations. *Journal of Physical Oceanography*, *52*(8), 1677–1691.
- 875 Sun, W., Dong, C., Tan, W., & He, Y. (2019). Statistical characteristics of cyclonic
 876 warm-core eddies and anticyclonic cold-core eddies in the north pacific based
 877 on remote sensing data. *Remote Sensing*, *11*(2), 208.
- 878 Sun, W., Dong, C., Wang, R., Liu, Y., & Yu, K. (2017). Vertical structure anomalies
 879 of oceanic eddies in the kuroshio extension region. *Journal of Geophysical Re-*
 880 *search: Oceans*, *122*(2), 1476–1496.
- 881 Sverdrup, H. U., Johnson, M. W., Fleming, R. H., et al. (1942). *The oceans: Their*
 882 *physics, chemistry, and general biology* (Vol. 1087) (No. 8). Prentice-Hall New
 883 York.
- 884 Trott, C. B., Subrahmanyam, B., Chaigneau, A., & Roman-Stork, H. L. (2019).
 885 Eddy-induced temperature and salinity variability in the arabian sea. *Geophys-*
 886 *ical Research Letters*, *46*(5), 2734–2742.
- 887 Umlauf, L., & Burchard, H. (2003). A generic length-scale equation for geophysical
 888 turbulence models. *Journal of Marine Research*, *61*(2), 235–265.
- 889 Villas Bôas, A., Sato, O., Chaigneau, A., & Castelão, G. (2015). The signature
 890 of mesoscale eddies on the air-sea turbulent heat fluxes in the south atlantic
 891 ocean. *Geophysical Research Letters*, *42*(6), 1856–1862.
- 892 Zhai, X., Greatbatch, R. J., & Kohlmann, J.-D. (2008). On the seasonal variability
 893 of eddy kinetic energy in the gulf stream region. *Geophysical Research Letters*,
 894 *35*(24).

1 **How high frequency atmospheric forcing impacts**
2 **mesoscale eddy surface signature and vertical structure**

3 **Alexandre Barboni** ^{1,2,3}, **Alexandre Stegner** ¹, **Franck Dumas** ^{2,3}, **Xavier**
4 **Carton** ³

5 ¹Laboratoire de Météorologie Dynamique/IPSL, Ecole Polytechnique, Institut Polytechnique de Paris,

6 ENS, Université PSL, Sorbonne Université, CNRS, 91128 Palaiseau, France

7 ²Service Hydrographique et Océanographique de la Marine, 29200 Brest, France

8 ³Laboratoire d'Océanographie Physique et Spatiale, UBO, CNRS, IRD, Ifremer, 29280 Plouzané, France

9 **Key Points:**

- 10 • Seasonal variations in SST and mixed layer anomalies of a Mediterranean anti-
11 cyclone are retrieved in high resolution simulation
- 12 • The summer surface cold-core signatures are driven by differential vertical mix-
13 ing due to near-inertial waves
- 14 • SST retroaction on air-sea fluxes is necessary to retrieve eddy-induced mixed layer
15 anomalies

Corresponding author: Alexandre Barboni, alexandre.barboni@lmd.ipsl.fr

Abstract

Seasonal evolution of both surface signature and subsurface structure of a Mediterranean mesoscale anticyclones is assessed using the CROCO high-resolution numerical model with realistic background stratification and fluxes. In good agreement with remote-sensing and in-situ observations, our numerical simulations capture the seasonal cycle of the anomalies, induced by the anticyclone, both in the sea surface temperature (SST) and the mixed layer depth (MLD). The eddy signature on the SST shifts from warm-core in winter to cold-core in summer, while the MLD deepens significantly in the core of the anticyclone in late winter. Our sensitivity analysis shows that these dynamical properties can be accurately reproduced only if the resolution is high enough ($\sim 1km$ for the horizontal with 100 vertical levels in a Mediterranean stratification) and if the atmospheric forcing contains high-frequency. In this configuration the deformation radius is explicitly resolved and the vertical mixing parametrized by the $k-\epsilon$ closure scheme is three times higher inside the eddy than outside the eddy. This differential mixing is explained by near-inertial waves, triggered by the high-frequency atmospheric forcing. Near-inertial waves propagate more energy inside the eddy because of the lower effective Coriolis parameter in the anticyclonic core. In addition to these high spatial and temporal resolution, SST retroaction on air-sea fluxes appears to be necessary to obtain marked eddy mixed layer depth anomaly.

Plain Language Summary

Mesoscale eddies are turbulent structures present in every regions of the world ocean, and accounting for a significant part of its kinetic energy budget. These structures can be tracked in time and recently revealed a seasonal cycle from in situ data. An anticyclone (clockwise rotating eddy in the northern hemisphere) is observed in the Mediterranean to be predominantly warm at the surface and to deepen the mixed layer in winter, but shifts to a cold-core summer signature. This seasonal signal is not yet understood and studied in ocean models. In this study we assess the realism of an anticyclone seasonal evolution in high resolution numerical simulations. Eddy surface temperature seasonal shift is retrieved and is linked to an increased mixing at the eddy core spontaneously appearing at high resolution (grid size $\sim 1km$) in the presence of high frequency atmospheric forcing. This increased mixed is due to the preferred propagation of near-inertial waves in the anticyclone due to its negative relative vorticity. Eddy-induced mixed layer depth anomalies also appear to be triggered by sea surface temperature retroaction on air-sea fluxes. These results suggest that present-day operational ocean forecasting models are too coarse to accurately retrieve mesoscale evolution.

1 Introduction

Mesoscale eddies are ubiquitous turbulent structures in the oceans, in thermal wind balance with a signature in density. Eddies have been observed for a long time, in particular in energetic regions such as the Gulf Stream rings (Richardson, 1980), the Kuroshio extension (Itoh & Yasuda, 2010), the Agulhas current retroflexion (Olson & Evans, 1986), but also in the Mediterranean Sea (Mkhinini et al., 2014). Mesoscale anticyclones (respectively cyclones) are structures of negative (positive) density anomaly, identified with a sea surface height (SSH) elevation (depression) (Chelton et al., 2007). Eddies statistical descriptions really began with the availability of eddy automated detections based on gridded altimetry products (Doglioli et al., 2007; Chaigneau et al., 2009; Nencioli et al., 2010; Chelton, Schlax, & Samelson, 2011; Mason et al., 2014; Le Vu et al., 2018; Laxenaire et al., 2018). The first quantitative studies were done in a composite approach : many daily snapshots detections are collocated with eddy contours and gathered into a single annual mean eddy signature (Hausmann & Czaja, 2012; Everett et al., 2012). This approach combined with remote-sensing measurements provide an extensive view of ed-

66 dies in various regions of the global ocean, with SST, sea surface salinity (Trott et al.,
 67 2019), chlorophyll (Chelton, Gaube, et al., 2011) and also meteorological variables (Frenger
 68 et al., 2013). Composite approach also allowed to reveal a modulation of air-sea fluxes
 69 at the eddy scale : in the Agulhas retroflexion region, (Villas Bôas et al., 2015) showed
 70 the total heat flux to the atmosphere to be enhanced over very strong and warm anti-
 71 cyclones. Similarly for the eddy vertical structure, gathering Argo profiles as a function
 72 of normalized distance to the eddy center, eddies were found to influence the mixed layer
 73 depth (MLD) (Sun et al., 2017; Gaube et al., 2019). Anticyclones have deeper MLD in
 74 their core, cyclones shallower MLD, with larger mixed layer anomalies in winter. Eddies
 75 were also observed to incorporate a significant seasonal cycle in their radius variations
 76 (Zhai et al., 2008) and their SST signature (Sun et al., 2019; Y. Liu et al., 2021). An-
 77 ticyclones (respectively cyclones) usually identified as warm in surface, actually shift to
 78 cold (warm) signatures in summer in several regions of the world ocean (Sun et al., 2019;
 79 Moschos et al., 2022). This phenomenon is then referred to as 'inverse' SST signatures.
 80 (Moschos et al., 2022) showed that these 'inverse' signatures actually become predom-
 81 inant in summer in the Mediterranean Sea, a seasonal shift yet not properly understood.

82 The composite approach is nonetheless ill-suited to study eddy temporal variabil-
 83 ity due to the stacking of numerous observations in time. Recently Lagrangian approaches
 84 were developed to study eddies enabling to better track their temporal variability (Pessini
 85 et al., 2018; Laxenaire et al., 2020; Barboni et al., 2021). Using a Lagrangian approach,
 86 (Moschos et al., 2022) showed that the same individual anticyclones shift from a warm
 87 winter SST anomaly to a cold one in summer (and conversely for cyclone). With the ad-
 88 ditional Argo floats trapped in anticyclones, they further noticed that anticyclonic den-
 89 sity anomaly remain warmer at depth while becoming colder in surface, leading to a smoother
 90 density gradient. Hence the hypothesis that this seasonal shift could be explained by a
 91 modulation of the vertical mixing by mesoscale eddies, anticyclones (cyclones) likely en-
 92 hancing (decreasing) mixing in surface. Recent observations in the Mediterranean Sea
 93 of inside-anticyclone properties temporal evolution further revealed eddy mixed layer anom-
 94 alies to be much larger than the composite approach mean value, reaching sometimes 300m
 95 (Barboni, Coadou-Chaventon, et al., 2023). MLD anomalies evolution was also shown
 96 to have evolution much faster than the month, with delayed restratification inside an-
 97 ticyclones. Mechanisms driving these MLD anomalies are also unexplained, but (Barboni,
 98 Coadou-Chaventon, et al., 2023) found it to be impacted by interactions with the an-
 99 ticyclone vertical structure.

100 An eddy modulation of vertical mixing was not proven so far but could be due to
 101 a modulation of near-inertial waves (NIW) propagation. NIW can not propagate at fre-
 102 quencies lower than the inertial frequency f due to Earth rotation (Garrett & Munk, 1972).
 103 However in the presence of a balanced flow, anticyclones (cyclones) having negative (pos-
 104 itive) relative vorticity ζ locally shift this cut-off by an effective inertial frequency $f_e =$
 105 $f + \zeta/2$ (Kunze, 1985). Sub-inertial waves ($\omega \lesssim f$) can then remained trapped in an-
 106 ticyclones and supra-inertial waves ($\omega \gtrsim f$) can be expelled from cyclones. Consequently,
 107 NIW propagate more inside anticyclones, what was experimentally (D'Asaro, 1995) and
 108 numerically (Danioux et al., 2008, 2015; Asselin & Young, 2020) proven. This NIW trap-
 109 ping potential partly explains the interest in anticyclones rather than in cyclones, the
 110 other reason likely being that anticyclones are more stable in time (Arai & Yamagata,
 111 1994; Graves et al., 2006), in particular for large structures (Perret et al., 2006), then
 112 more easily detected and trapping more often profilers (thus easing field campaigns). Sev-
 113 eral recent observations (Martínez-Marrero et al., 2019; Fernández-Castro et al., 2020)
 114 showed that mixing at depth is enhanced below anticyclones due to this more energetic
 115 NIW propagation. On the other hand numerical studies assumed extremely simplified
 116 set-up with constant wind (Danioux et al., 2008) or an idealized wind burst (Asselin &
 117 Young, 2020). They also looked at NIW propagation in an eddying field at short time
 118 scales, then without significant evolution of the eddies and stratification. Eddy-NIW in-
 119 teraction on longer time scales - eddy evolving time scales like months - in a varying strat-

120 ification due to seasonal cycle has never been assessed so far. In particular the effect of
 121 this differential NIW propagation on eddies remains unknown and a gap remains between
 122 wave propagation and enhanced surface mixing.

123 Some recent studies started to assess eddy temporal evolution in high resolution
 124 regional models. In the Mediterranean Sea, Escudier et al. (2016) compared eddy size,
 125 drift and lifetime compared to eddies in altimetric observations. Mason et al. (2019) in-
 126 vestigated these variables in assimilated operational models and additionally looked at
 127 MLD anomalies, but both were in a composite approach and did not look at eddy SST
 128 variations. More recently Stegner et al. (2021) performed an observation system simu-
 129 lation experiment on a $1/60^\circ$ simulation of the Mediterranean sea and found great bias
 130 on size and strength for small eddy detections, but did not look at SST variations. Us-
 131 ing the same simulation, an interesting method was developed by Ioannou et al. (2021),
 132 investigating differences in both trajectories, size and stratification of the Ierapetra an-
 133 ticyclonic eddy, but restricted to this particular case.

134 Both eddy SST anomalies seasonal shift and mixed layer depth anomalies remain
 135 poorly investigated so far in ocean models. If NIW propagation and eddy vertical struc-
 136 ture are considered, grid resolution - both horizontal and vertical - and atmospheric forc-
 137 ing are likely key aspects to take into account. Indeed air-sea fluxes and near-inertia-gravity
 138 waves involve much shorter temporal and spatial scales, not reproduced even in eddy-
 139 permitting models at present stage. We then aim to assess the realism of an anticyclone
 140 seasonal signal in both surface and mixed layer using an idealized but high-resolution
 141 simulation and investigating driving physical processes. The goal is to assess the real-
 142 ism of the eddy temporal evolution compared to similar observations, in particular the
 143 retrieval of the surface signature seasonal cycle. In a first part we conduct a sensitivity
 144 analysis on horizontal grid cell. In a second part we study the sensitivity to atmospheric
 145 forcing frequency. Last, the effect of SST retroaction on air-sea fluxes is discussed.

146 2 Methods

147 2.1 Model set-up

148 Idealized numerical experiments are performed using the Coastal and Regional Ocean
 149 Community (CROCO) model. CROCO is based on the Regional Ocean Modeling Sys-
 150 tem (ROMS) kernel (Shchepetkin & McWilliams, 2005). It uses a time splitting method
 151 between the fast barotropic mode and the slow baroclinic ones. Advection schemes are
 152 UP3 for horizontal and Akima-Splines for the vertical. Trying to conciliate realistic and
 153 idealized approach, we use double periodic conditions in a realistic stratification and on
 154 long timescale. The atmospheric forcing has realistic temporal variations but is spatially
 155 homogeneous. The only active tracer used is temperature. As a consequence, a linear
 156 state equation links density ρ and temperature T , with thermal expansion $T_c = 0.28kg.m^{-3}.K^{-1}$
 157 and linear approximation close to $T_0 = 25^\circ C$ and $\rho_0 = 1026kg.m^{-3}$:

$$\rho = \rho_0 + T_c(T - T_0) \quad (1)$$

158 Discarding salinity effects is justified by the very weak salinity seasonal cycle in the
 159 Mediterranean Sea. The heat flux seasonal cycle is roughly $\pm 150 W.m^{-2}$ (Pettenuzzo et
 160 al., 2010), whereas salinity fluxes are mostly driven by the evaporation minus precipi-
 161 tation balance, with a mean of roughly $10^3 mm/y$, a seasonal cycle maximal amplitude
 162 of $\Delta F = 4 \times 10^2 mm/y$ and river input being negligible (Mariotti, 2010). Consider-
 163 ing a haline contraction coefficient of $S_c = 0.78kg.m^{-3}.PSU^{-1}$, a ΔF freshwater in-
 164 put would have a seasonal equivalent effect on buoyancy $Q_{eq} = \rho_0 c_p \frac{S_c}{T_c} S_0 \Delta F \approx 5 W.m^{-2}$,
 165 indeed almost two orders of magnitude lower than Q_{tot} .

166

Grid

167

168

169

170

171

172

173

174

Simulation domain is double periodic, on the f -plane, with a flat bottom $H_{bot} = 3000m$. Horizontal extent is 200km in both directions, with horizontal resolution ranging between 4km and 500m, with respectively 25 to 150 vertical levels. Horizontal to vertical grid size ratio is kept roughly constant about 1000/3 in the upper layers, close to the Brunt-Vaisala to inertia frequency ratio. Coriolis parameter is $f = 9.0 \times 10^{-5} s^{-1}$. CROCO uses a σ terrain-following coordinate, the N vertical levels being modulated in time between bottom and sea surface height η . Constant depth level z_0 are stretched over thickness h_c with surface coefficient θ_s :

$$z = \eta + (\eta + H_{bot})z_0 \quad (2)$$

$$z_0 = \frac{h_c \sigma + H_{bot} C_s(\sigma)}{h_c + H_{bot}} \quad \text{with} \quad C_s(\sigma) = \frac{1 - \cosh\left(\theta_s \frac{\sigma - N}{N}\right)}{\cosh(\theta_s) - 1} \quad (3)$$

175

176

177

178

179

180

With $N = 100$ levels, $h_c = 400m$ and $\theta_s = 8$, vertical grid steps are then close to 5m in the upper 200m. 200m being the vertical scale of the thermocline, it ensures a maximal resolution in the upper ocean where seasonal variations occur (Houpert et al., 2015). This configuration has then a higher vertical resolution than previous similar studies ($N = 32$ $h_c = 250m$ and $\theta_s = 6.5$ for Escudier et al. (2016)) or operational models (Juza et al., 2016).

181

Turbulent closure

182

183

184

185

Mixing is parametrized through k - ϵ closure scheme (Rodi, 1987) using the generic length scale approach (Umlauf & Burchard, 2003). Turbulent kinetic energy k dissipates with rate ϵ and stability function c_v into an effective viscosity ν (respectively c_T and κ for diffusivity). No additional explicit mixing is added.

$$\nu = \frac{c_v k^2}{\epsilon} \quad \text{and} \quad \kappa = \frac{c_T k^2}{\epsilon} \quad (4)$$

186

187

188

189

190

191

As implemented in the CROCO model, a minimal k input is parameterized. Given that the minimal dissipation rate ϵ is set to $10^{-12} W.kg^{-1}$, the minimal k has to be set to $10^{-9} m^2.s^{-2}$ in order to retrieve a minimal diffusivity of $10^{-6} m^2.s^{-1}$ with a stability function of order unity. This diffusivity value is close to kinematic viscosity and thermal diffusivity for water (respectively 1×10^{-6} and $1 \times 10^{-7} m^2.s^{-1}$). This issue is also discussed by Perfect et al. (2020).

2.2 Background stratification and initial mesoscale anticyclone

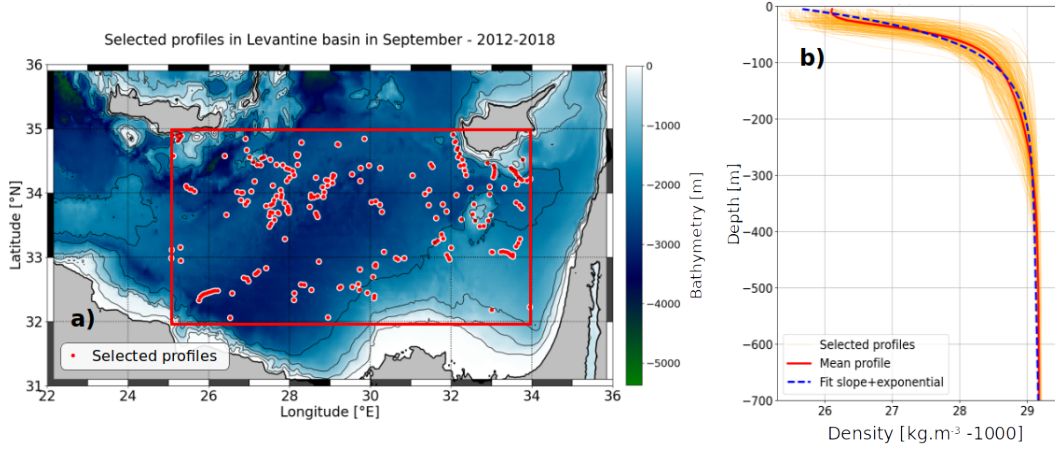


Figure 1. (a) Map showing the region of high long-lived anticyclones occurrence in the Levantine basin. The atmospheric fields used as input are averaged over the area delimited by the green frame. Black dots are the cast position of 242 selected in situ profiles identified as outside-eddy. Bathymetry is ETOPO1 data (Smith & Sandwell, 1997) with 0, 500, 1000 and 1500m isobaths. (b) Density vertical structure of selected profiles (orange thin lines), mean profile (red thick line) and fitted profile using Eq.5 (blue dashed).

A realistic background stratification is set from a climatological database gathering in situ delayed-time and near-real-time data from Copernicus Marine Environment Monitoring Service (Barboni, Stegner, et al., 2023). A region of interest is considered at the center of the Levantine Basin (25 to 34 °E and 32 to 35 °N, shown in Fig.1a). For background stratification we used only profiles in the region of interest, detected as outside-eddy using the DYNED eddy atlas dataset (see Barboni, Coadou-Chaventon, et al. (2023) for details), from 2012 to 2018 and for each year in September. Considering these criteria, 242 profiles are averaged into a mean stratification $\rho_b(z)$ fitted over the first 1000m with a linear slope S added to an exponential with vertical Z_T in the upper water column (Eq.5, see Fig.1b). September is chosen as the end of summer when the thermocline is marked and stratification gradient the strongest, allowing a better fit with exponential slope.

$$\rho_b(z) = \rho_1 + (\rho_s - \rho_1) \exp\left(-\frac{z}{Z_T}\right) + Sz \quad (5)$$

Regression fit gave $\rho_1 = 1029.03 \text{ kg.m}^{-3}$, $\rho_s = 1025.3 \text{ kg.m}^{-3}$, $Z_T = 55 \text{ m}$, $S = 1.8 \times 10^{-4} \text{ kg.m}^{-4}$. Corresponding baroclinic deformation radius is approximately 11km. An initial density anomaly σ in geostrophic equilibrium is added to the background stratification. $\sigma(r, z)$ is azimuthally symmetric and has a Gaussian shape in the vertical direction and pseudo-Gaussian in the radial one, with radius R_m and vertical extent H :

$$\sigma(r, z) = \sigma_0 \frac{z}{H} \exp\left(-\frac{1}{\alpha} \left(\frac{r}{R_m}\right)^\alpha\right) \exp\left(-\frac{1}{2} \left(\frac{z}{H}\right)^2\right) \quad \text{with} \quad \sigma_0 = \frac{\rho_0 f V_m R_m e^{1/\alpha}}{gH} \quad (6)$$

211 The initial maximal speed radius R_m is 25 km, slightly more than twice the defor-
 212 mation radius but still smaller than the large long-lived Eastern Mediterranean anticy-
 213 clones (Barboni, Coadou-Chaventon, et al., 2023), giving a Burger number ($Bu = R_d^2/R_m^2$)
 214 close to 0.2. Maximal speed is initially set to $V_m = 0.4 m.s^{-1}$ giving a Rossby number
 215 ($Ro = V_m/R_m f$) of 0.16, but later decays around 0.1 due to eddy evolution. $Ro = 0.1$
 216 is a standard value in the Mediterranean Sea (Ioannou et al., 2019). H is set to 100m
 217 on the same order as thermocline extent Z_T , and shape parameter $\alpha = 1.6$ ensures baro-
 218 clinic stability (Carton et al., 1989; Stegner & Dritschel, 2000). Cyclogeostrophic cor-
 219 rection is added following Penven et al. (2014).

220 **2.3 Atmospheric heat forcing**

221 Air-sea fluxes are computed with the Coupled Ocean–Atmosphere Response Ex-
 222 periment (COARE) 3.0 parametrization (Fairall et al., 2003), with improved accuracy
 223 for large wind speeds ($> 10m.s^{-1}$) encountered in high frequency forcing. Short wave
 224 heat flux Q_{SW} is distributed on the vertical following Paulson and Simpson (1977) trans-
 225 parency model with Jerlov water type I, consistent with very clear Mediterranean wate-
 226 rs ($R = 0.58$, $\zeta_1 = 0.35m$, $\zeta_2 = 23m$):

$$I(z) = Q_{SW} \left(R \exp\left(-\frac{z}{\zeta_1}\right) + (1 - R) \exp\left(-\frac{z}{\zeta_2}\right) \right) \quad (7)$$

227 Upward long-wave heat flux Q_{LW}^\uparrow computes the ocean SST (T_s) thermal loss us-
 228 ing Stefan-Boltzmann black body law, with emissivity $\epsilon_{sb} = 98.5\%$ and $\sigma_{sb} = 5.6697 \times$
 229 $10^{-8} W.m^{-2}.K^{-4}$, convention positive downwards :

$$Q_{LW}^\uparrow = -\epsilon_{sb} \sigma_{sb} T_s^4 \quad (8)$$

230 Latent heat flux Q_{Lat} and sensible heat flux Q_{Sen} also involves a direct SST retroac-
 231 tion:

$$Q_{Lat} = -\rho_a L_E C_E |V| (q_s - q_a) \quad ; \quad Q_{Sen} = -\rho_a c_p C_S |V| (T_s - T_{2m}) \quad (9)$$

232 With ρ_a air density, c_p air thermal capacity, L_E evaporation enthalpy and $|V|$ 10m
 233 wind speed. q_s and q_a are specific humidity for ocean and atmosphere at 2m respectively,
 234 saturated at T_s for q_s , related to saturated water pressure P_{sat} fro $q_a : q_a = 0.622 h_{2m} P_{sat}(T_{2m}) / P_{SL}$
 235 and $q_s = 0.98 \times 0.622 \times P_{sat}(T_s) / P_{SL}$. Factor 0.98 accounts for water vapor reduction
 236 caused by salinity (Sverdrup et al., 1942). Last, wind stress is computed from zonal and
 237 meridional winds (u and v) :

$$\tau_x = \frac{\rho_a}{\rho_0} C_D |u| u \quad \text{and} \quad \tau_y = \frac{\rho_a}{\rho_0} C_D |v| v \quad (10)$$

238 In equations 9-10, C_E , C_S and C_D are corresponding transfer coefficients consid-
 239 ering the stability of the atmospheric boundary layer based on the Monin-Obukhov simi-
 240 larity theory. They are all on the order of 1×10^{-3} (Fairall et al., 2003).

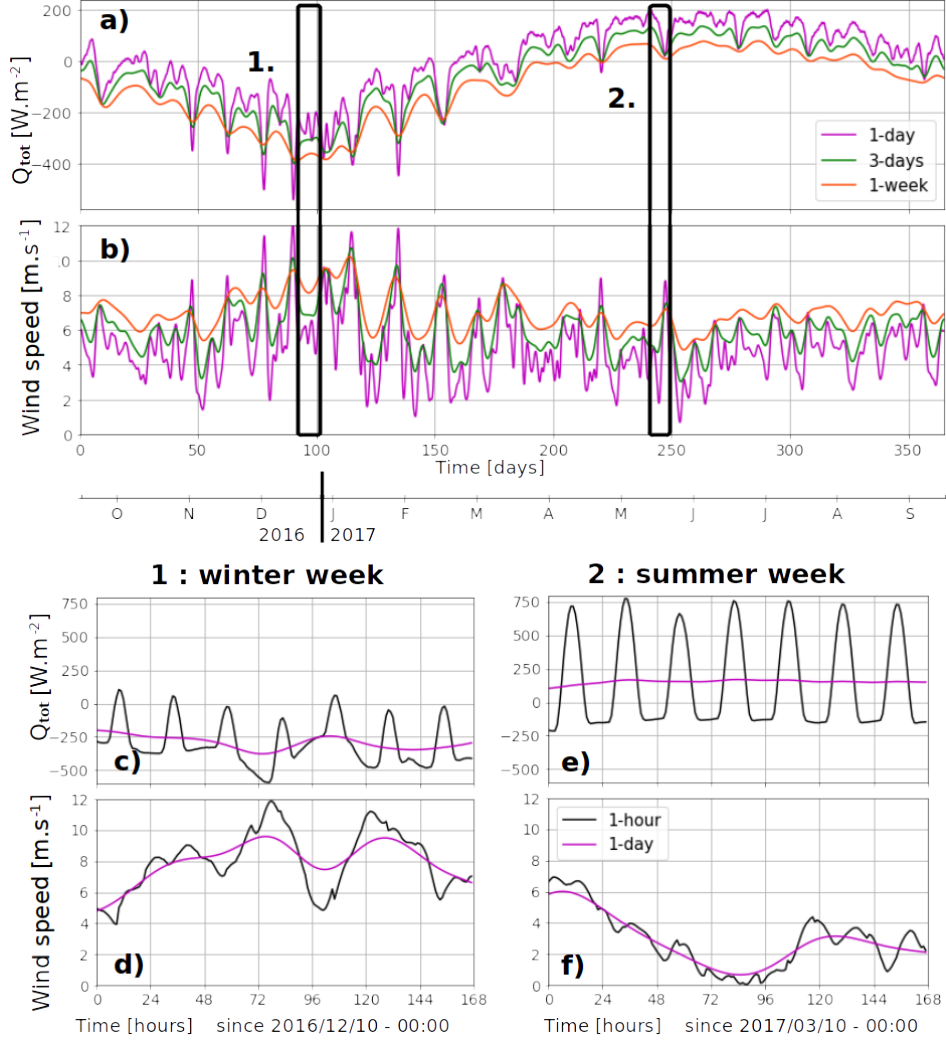


Figure 2. Net heat flux and wind speed for the 5 input timeseries, shown separately as diurnal cycle gives larger variations. (a) Net heat flux and (b) wind speed for the 1-day (magenta line), 3-days (green) and 1-week (orange) timeseries over one year. To enhance readability, 3-days and 1-week net heat flux are lowered by 20 and 40 $W.m^{-2}$ respectively. (c) 1-hour (black) and 1-day (magenta) net heat flux (respectively (d) for wind speed) in a winter week of 2016. (e) and (f) : same as (c) and (d) in a summer 2017 week.

241 ERA5 reanalysis input is used for atmospheric forcing. Fields are available with
 242 a 1 hour temporal resolution and $1/4^\circ$ horizontal resolution (Hersbach et al., 2020). To
 243 focus on the temporal variability, forcing timeseries are spatially averaged over the Lev-
 244 antine basin (Fig.1a). Four forcing inputs with different temporal scales are tested : 1-
 245 hour, 1-day, 3-days and 1-week. The 1-hour forcing is the original ERA5 timeseries, the
 246 three later ones are Gaussian smoothing of the 1-hour timeseries with double-window
 247 size of 1, 3 and 7 days respectively, shown in Fig.2. One year of forcing from 15 Septem-
 248 ber 2016 to 15 September 2017 runs cyclically for 2 years as forcing input, with root mean
 249 square wind speed $\bar{V} = 5.5 m.s^{-1}$. 10m neutral wind from ERA5 is used for wind stress
 250 in Eq.10. To keep the same wind speed magnitude with varying wind frequency, smoothed
 251 timeseries for zonal and meridional winds (\bar{u} and \bar{v}) have to be rescaled. The correction
 252 factor λ being $\gtrsim 1.1$ for 1-day timeseries, and $1.1 < \lambda < 2$ for 3-days and 1-week :

$$\tilde{u} = \lambda \bar{u}; \tilde{v} = \lambda \bar{v} \quad \text{with} \quad \lambda = \frac{\sqrt{u^2 + v^2}}{\sqrt{\bar{u}^2 + \bar{v}^2}} \quad (11)$$

253 The same year is kept to avoid disturbance with interannual variations, which are
 254 strong for heat fluxes over the Mediterranean Sea (Mariotti, 2010; Pettenuzzo et al., 2010),
 255 but no significant variations were observed when selecting another year.

256 ***Forcing without surface temperature retroaction***

257 A comparison experiment is run without SST retroaction on ocean-atmosphere fluxes.
 258 In this configuration, the net heat flux Q_{tot} from ERA5 directly forces the upper ocean
 259 layer, the short wave part Q_{SW} being still distributed on the vertical (Eq.7). Momen-
 260 tum fluxes are computed from Eq.10 with constant drag coefficient $C_D = 1.6 \times 10^{-3}$.
 261 The net heat flux Q_{tot} timeseries in ERA5 has daily amplitudes around $\pm 150 W.m^{-2}$ and
 262 an annual average of $-3.0 W.m^{-2}$, consistent with the net evaporation of the Mediter-
 263 ranean sea (Mariotti, 2010). The net heat flux is then corrected by linearly decreasing
 264 the negative values to achieve a zero annual average, avoiding a drift of the mean strat-
 265 ification.

266 **2.4 Eddy tracking indicators**

267 ***Eddy shape, radius and intensity***

268 Eddy detections are provided through the Angular Momentum Eddy Detection and
 269 Tracking Algorithm (AMEDA). AMEDA is a mixed velocity-altimetry approach, its re-
 270 lies on using primarily streamlines from a velocity field and identifying possible eddy cen-
 271 ters computed as maxima of local normalized angular momentum (Le Vu et al., 2018).
 272 It was successfully used in several regions of the world ocean in altimetric data (Aroucha
 273 et al., 2020; Ayouche et al., 2021; Barboni et al., 2021), high frequency radar data (F. Liu
 274 et al., 2020) or numerical simulations (de Marez et al., 2021). In each eddy single ob-
 275 servation (one eddy observed one day), AMEDA gives a center (which position is noted
 276 \mathbf{X}_e hereafter) and two contours. The 'maximal speed' contour is the enclosed stream-
 277 line with maximal speed (i.e. in the geostrophic approximation, with maximal SSH gra-
 278 dient) ; it is assumed to be the limit of the eddy core region where water parcels are trapped.
 279 The 'end' contour is the outermost closed SSH contour surrounding the eddy center and
 280 the maximal speed contour ; it is assumed to be the area of the eddy footprint, larger
 281 than just its core but still influenced by the eddy shear (Le Vu et al., 2018). The observed
 282 maximal speed radius R_m is then defined as the radius of the circle having an area equal
 283 to the maximal speed contour. Eddy detection through interpolated Level 4 SSH prod-
 284 ucts leads to imperfections. It typically smooths gradients and then reduces observed
 285 geostrophic velocities (Amores et al., 2018; Stegner et al., 2021). To mimic those imper-
 286 fections in the numerical simulations, AMEDA detections are performed on the 48h-averaged
 287 SSH field at model grid resolution.

288 ***Eddy SST signature δT , heat flux δQ , differential mixing ratio ξ and mixed*** 289 ***layer anomaly***

290 The anticyclone-induced SST signature δT is defined as the difference of SST be-
 291 tween the eddy core SST_{in} and its periphery SST_{peri} . Adapting Moschos et al. (2022),
 292 SST_{in} is the average of the area centered on $\mathbf{X}_e(t)$ with radius $2/3R_m(t)$; SST_{peri} is
 293 the average on an annular area centered on \mathbf{X}_e with radius between $2/3R_m(t)$ and $2R_m(t)$.
 294 Positive (negative) δT then indicates a warm-core (cold-core) signature. Similarly the
 295 induced signature on ocean-atmosphere fluxes is defined as δQ , with positive δQ for in-
 296 creased warming at the eddy core. Thermal heat flux feedback (THFF) is then defined

297 as the linear regression of δQ as a function of δT over the second year of simulation (from
298 365 to 730 days, see Sect.3.3).

299 Differential mixing between the eddy core and outside-eddy are measured through
300 the index ξ . Temperature vertical diffusivity κ computed by $k-\epsilon$ mixing closure from
301 instantaneous history record is spatially averaged in the eddy core (κ^{AE}) and outside-
302 eddy (κ^{Out}). The eddy core region corresponds here to the area around the eddy center
303 with radius $2/3R_m(t)$. The outside-eddy region is defined as the area outside any 'end'
304 contours detected by the tracking algorithm. Diffusivity spanning several orders of mag-
305 nitude, differential mixing ξ is then evaluated as a vertical average of the ratio of these
306 two quantities, typically using a depth $h = 20m$ to focus on the upper layers stratified
307 in summer :

$$\xi = \frac{1}{h} \int_{-h}^{surf} \frac{\kappa^{AE}}{\kappa^{Out}} dz \quad (12)$$

308 Summer eddy SST signature magnitude $\overline{\delta T}$ is defined as the 30th δT percentile over
309 the summer, and its spread as the difference between the 30th and the 10th percentiles
310 (see results in Table 1). Similarly ξ is defined as the median of the ξ distribution over
311 the summer, and its spread as the difference between the median and the 30th percentile.
312 First and second summers are defined as 230 to 340 days and 590 to 700 days respec-
313 tively, corresponding to the May to August period when a significant number of warm-
314 core anticyclones are observed (Moschos et al., 2022).

315 Last, the MLD anomaly ΔMLD are defined for a given winter as the maximal dif-
316 ference reached between the MLD outside-eddy and the MLD inside-eddy, following (Barboni,
317 Coadou-Chaventon, et al., 2023). In the following numerical experiments running for 2
318 years, the first winter is considered as a transient period not retained for analysis. ΔMLD
319 is then computed only for the second winter, defined as 450 to 580 days, corresponding
320 to the December to April period, when maximal MLD are reached in the Mediterranean
321 Sea (Houpert et al., 2015).

322 **3 Idealized simulations compared to observations**

323 The temporal evolution of mesoscale eddies in the Levantine basin can be retrieved
324 for several anticyclones where Argo floats remained trapped several months, as exten-
325 sively studied in Barboni, Coadou-Chaventon, et al. (2023). A marked seasonal signal
326 is detected in both SST and vertical structure. An example is shown in Fig.3 with a Ier-
327 apetra anticyclone. Ierapetra anticyclones are strong recurrent anticyclonic structures
328 formed each year in the lee of Crete island (Ioannou et al., 2020). In the example shown
329 below, δT index has a marked oscillation between a winter warm core and summer cold
330 core. The weekly smoothed signature can be measured to about $\delta T \approx +0.7^\circ C$ in both
331 winters 2016-2017 and 2017-2018, and about $-0.3^\circ C$ in summer 2017 (about $-0.2^\circ C$
332 in summer 2018). The vertical structure could also be measured thanks to large Argo
333 deployments (Fig.3h) ; due to errors in the salinity sensors, density in 2018 is estimated
334 from temperature applying a linear regression using 2017 data. One can also notice the
335 seasonal variations of the anticyclone maximal speed, with two maxima in late winter.
336 This is consistent with kinetic energy inverse cascade maximal peak from submesoscale
337 to mesoscale in kinetic energy distributions (Zhai et al., 2008; Steinberg et al., 2022), but
338 it is still noticeable to have the same phenomenon tracking a single individual structure.
339 Here the physical processes driving these observed seasonal variations are studied with
340 numerical experiments, investigating sensitivity to horizontal resolutions, forcing frequency
341 and SST retroaction on air-sea fluxes. Simulations are summarized in Table 1, the ref-
342 erence considered being 1km resolution with 1-hour forcing, 100 vertical levels with SST
343 retroaction (run 1K100-1H in Table 1 below).

Ierapetra anticyclone timeline (2016-2018)

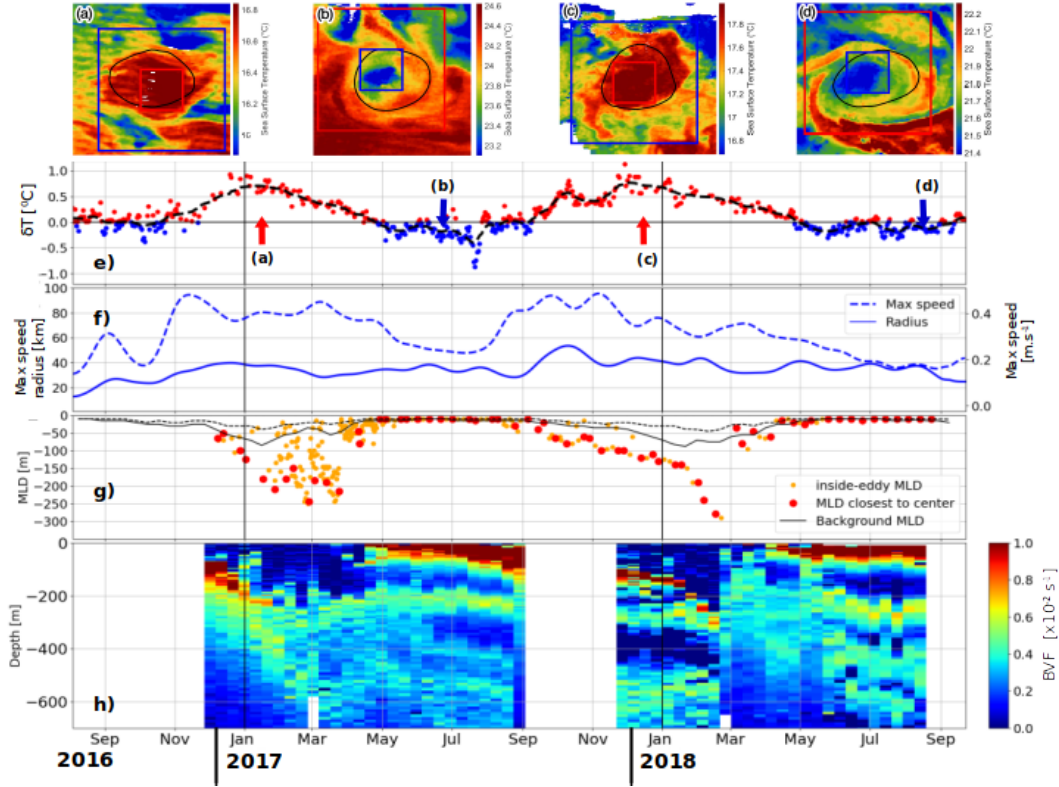


Figure 3. Temporal evolution of the Ierapetra anticyclone formed South-East of Crete in late summer 2016. Upper panels are high-resolution SST snapshots in (a) January 2017, (b) June 2017, (c) December 2017 and (d) July 2018, the maximal speed contour (see Sect.2.4 is in black line). (e) δT eddy SST anomaly, cold-core in blue and warm-core in red, with black dashed line showing the 5 days smoothed evolution. (f) Maximal speed V_m (dashed blue) and radius R_m (continuous blue) with 10 days smoothing. (g) MLD evolution inside the the anticyclone (dots, with red ones highlighting the closest to center), with outside-eddy background MLD in continuous black line (spread between dashed lines). (h) Brunt-Vaisala frequency.

344

3.1 Horizontal resolution sensitivity

345

346

347

348

349

350

351

352

353

354

The numerical simulation at 4km resolution and 25 vertical levels (run B in Table 1) reveals a few discrepancies with real observations. A horizontal resolution of 4km is close to operational oceanography models in the Mediterranean Sea (Juza et al., 2016). At the surface, despite seasonal variations of the eddy SST signatures (Fig.4a-c) and in the δT index (Fig.4f), summer 'inverse' signatures are not retrieved with no cold-core anticyclone. A steady erosion of the eddy strength is also noticeable, with a decrease in the maximal speed decreasing from $0.35m.s^{-1}$ to $0.15m.s^{-1}$ in 2 years, while its radius remains constant ($\approx 25km$, Fig. 4e). Note that the initial maximal speed is set to $0.4m.s^{-1}$ (see Sect.2.2) but the smoothing effect of time-averaging leads to a lower detected initial value of $0.35m.s^{-1}$.

355

356

357

At depth, the mixed layer anomaly is significant, on the order of 50m (Fig.4g). Some bursts of differential mixing are observed in late winter from December to March when mixed layer instabilities and restratification processes can occur, with ξ reaching a few

[ht]

Table 1. Summary table of CROCO numerical experiments. Runs start in September of the atmospheric forcing timeseries. Thermal heat flux feedback (THFF), eddy SST anomaly index $\delta\bar{T}$ and differential mixing ratio $\bar{\xi}$ are defined in Sect.2.4, and $\bar{\xi}$ is computed over the upper 20m. Subscripts ($\bar{\xi}_1, \bar{\xi}_2$) refers to first and second summers defined as 230 to 340 days and 590 to 700 days respectively. ΔMLD refers only to the second winter defined as 450 to 590 days (see shades in Fig.4d-h).

Name	Vertical levels	dx (km)	Freq	SST retroaction	THFF ($W.m^{-2}.K^{-1}$)	$\delta\bar{T}_1$ ($^{\circ}C$)	$\delta\bar{T}_2$ ($^{\circ}C$)	$\bar{\xi}_1$	$\bar{\xi}_2$	ΔMLD (m)
1K100-1H	100	1	1-hour	Yes	-41.5 ± 1.3	-0.20 ± 0.10	-0.18 ± 0.04	3.05 ± 0.70	2.81 ± 0.74	51
2K50-1H	50	2	1-hour	Yes	-40.7 ± 1.0	-0.12 ± 0.14	-0.11 ± 0.06	1.54 ± 0.31	1.34 ± 0.22	63
4K25-1H	25	4	1-hour	Yes	-34.3 ± 1.8	0.01 ± 0.14	0.02 ± 0.10	1.10 ± 0.12	1.00 ± 0.12	48
05K150-1H	150	0.5	1-hour	Yes	-39.2 ± 1.4	-0.16 ± 0.10	-0.19 ± 0.06	2.58 ± 0.58	2.71 ± 0.45	91
1K100-1D	100	1	1-day	Yes	-42.1 ± 0.8	-0.21 ± 0.20	-0.31 ± 0.06	2.99 ± 0.44	3.34 ± 1.23	57
1K100-3D	100	1	3-days	Yes	-44.7 ± 1.0	-0.12 ± 0.14	-0.09 ± 0.03	1.41 ± 0.28	0.99 ± 0.09	70
1K100-1W	100	1	1-week	Yes	-41.0 ± 0.4	-0.05 ± 0.05	-0.03 ± 0.01	1.25 ± 0.14	1.02 ± 0.01	94
1K100-1H-NoSST	100	1	1-hour	No	-	-0.41 ± 0.16	-0.51 ± 0.00	2.60 ± 0.46	2.47 ± 0.25	10

358 times values higher than 2 (Fig. 4h). However no differential mixing is retrieved in sum-
359 mer. On the other hand, the anticyclone vertical structure is coarsely reproduced. The
360 winter MLD cooling forms a homogeneous layer between 100 and 150m (Fig. 4i). These
361 winter waters formed by convection do not reproduce the homogeneous subsurface an-
362 ticyclone cores, separated by density jump or sharp temperature gradient such as the
363 continuous temperature gradient in Fig.3h around 200m depth (see other examples in
364 Fig.4-5 from Barboni, Coadou-Chaventon, et al. (2023)). The inability to reproduce this
365 mesoscale subsurface lens is not surprising given the low vertical resolution, the verti-
366 cal steps being on the order of 20m at 100m depth.

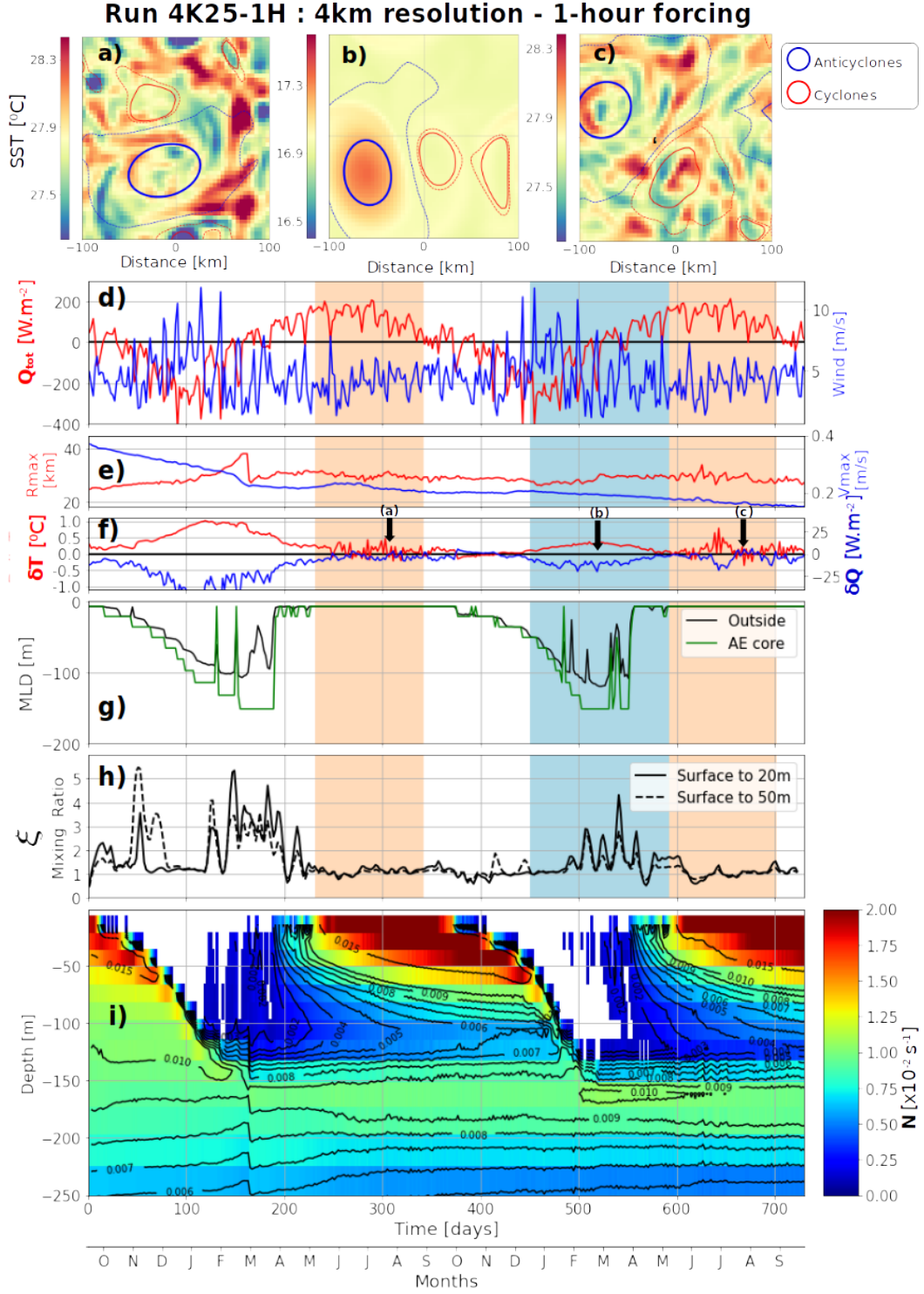


Figure 4. Simulation B from Table 1. (a) SST snapshot in the first summer, (b) in the second winter, (c) in the second summer, with eddies detected by AMEDA in contours. The initial anticyclone is highlighted by a thicker line. (d) Net heat flux (red) and windspeed (blue). (e) $R_m(t)$ (red) and $V_m(t)$ (blue) from AMEDA. (f) SST anomaly index δT (red), respectively heat flux anomaly δQ , blue). (g) Mixed layer inside-eddy (green) and outside-eddy (black). (h) Differential mixing ratio ξ defined in Eq.12 with $h = 20m$ (solid) and $h = 50m$ (dashed line). (i) Inside-eddy stratification evolution shown with Brunt-Vaisala frequency; contours are overlaid with interval $0.001s^{-1}$ and negative values are blanked. On panels c-h, summer periods are indicated by light red shades, winter by a light blue shade.

367 The same numerical set-up with a finer 1km horizontal resolution (run 1K100-1H
 368 in Table 1) shows a net contrast with the previous coarser simulation. This simulation
 369 has a 1km horizontal grid size and 100 levels with same stretching parameters giving ver-
 370 tical grid steps close to 3m in the upper 200m. A summer 'inverse' eddy surface tem-
 371 perature is clearly retrieved with 1-hour frequency heat and momentum forcing. As shown
 372 in Fig.5 in this configuration, a clear anticyclonic cold-core SST signature is observed
 373 in summer (Fig.5a), switching back to a winter warm-core SST the next winter (Fig.5b)
 374 and appearing again in the second summer (Fig.5c). This anticyclone surface seasonal
 375 oscillation can clearly be tracked by δT (Fig.5f). $\overline{\delta T}$ reached about $-0.2^{\circ}C$ in the both
 376 summers (see Table 1) with spikes of $\delta T \approx -0.5^{\circ}C$ and maximal value around $+0.4^{\circ}C$
 377 in winter. Considering anticyclonic cold-core signatures statistics in the Mediterranean
 378 Sea (Moschos et al., 2022) in particular their Fig.5b) $\delta T \approx -0.2^{\circ}C$ is a low but stan-
 379 dard value, anticyclone SST anomalies typically not being colder than $-0.5^{\circ}C$. This cold-
 380 core summer signature goes along with a mixing increase in the upper layers at the eddy
 381 core, measured by a diffusivity in summer more than twice as high inside the eddy core
 382 as outside. Sensibility of the ξ indicator is shown on Fig.5h, with ξ averaged over the
 383 upper 20m or 50m, the first case leading to ξ values higher than 4 in summer despite some
 384 variability. This enhanced mixing seems to be confined in the upper layers, as ξ decreases
 385 to approximately 1 as soon as the mixed layer deepens, but it increases again to simi-
 386 lar values during the second summer.

387 At depth the maximal mixed layer anomaly reaches about 50m (Fig.5h), very close
 388 to the value of the simulation at 4km resolution. However the vertical structure is bet-
 389 ter reproduced at 1km, and in particular between 100 and 150m deep the $5 \times 10^{-3} s^{-1}$
 390 stratification isoline closes in December, 4 months later than in the 4km simulation (in
 391 August, see Fig.4i). This means that homogeneous waters formed at depth in the first
 392 winter re-stratify more slowly. Eddy decay in time is also slower on maximal speed : af-
 393 ter 2 years the anticyclone velocity is about $0.3 m.s^{-1}$ with 1km resolution compared to
 394 $0.15 m.s^{-1}$ with 4km (Fig.4e). Sharp density gradients are smoothed in a coarser sim-
 395 ulation, leading to unrealistic temporal evolution of the anticyclones vertical structure.
 396 Surface (SST) or depth-integrated (maximal geostrophic speed) measurements are then
 397 not accurately reproduced at a spatial resolution of 4km.

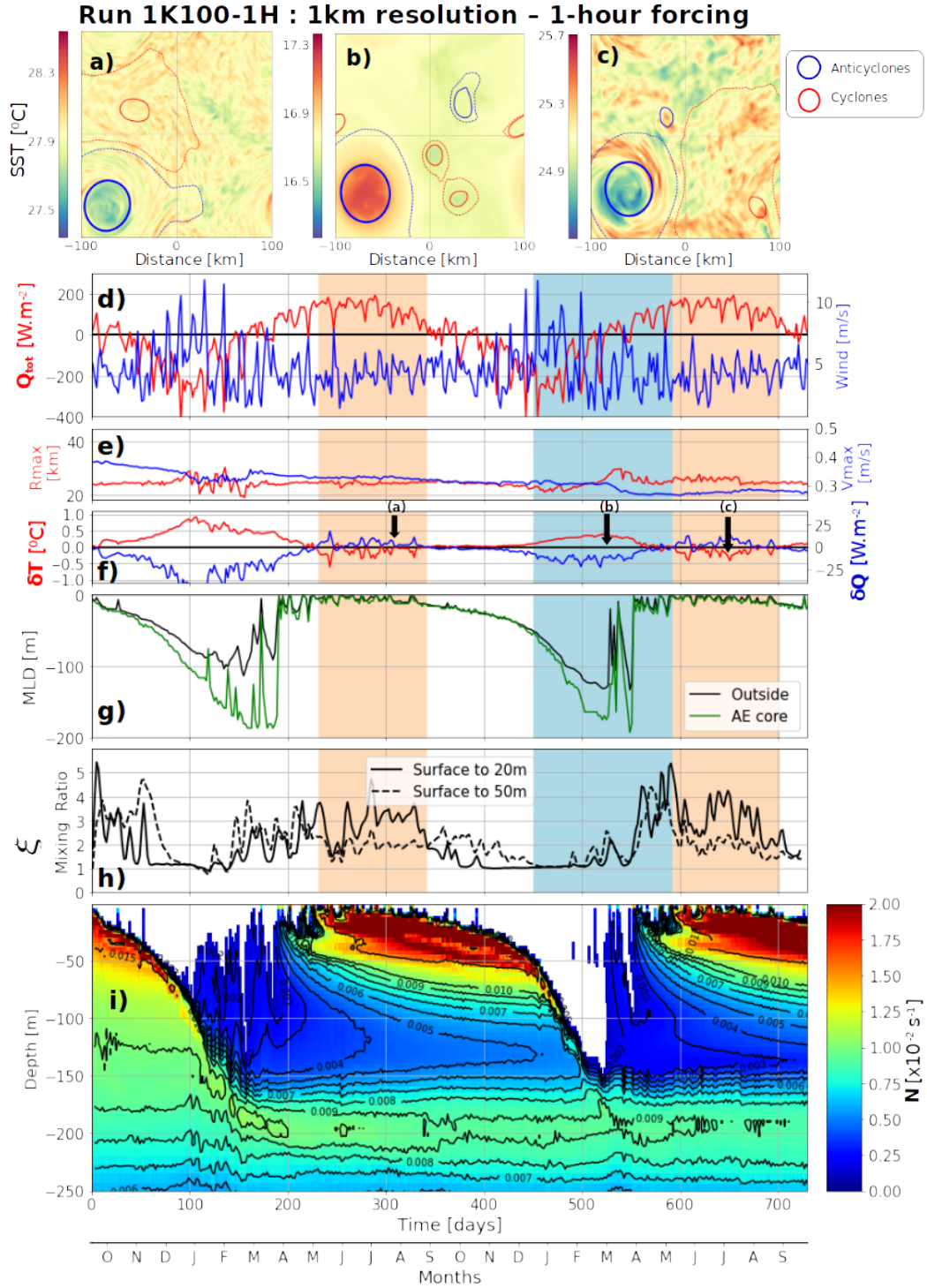


Figure 5. Simulation 1K100-1H from Table1. Same as in Fig.4 but with a 1km horizontal resolution.

398 An experimental series with the same numerical set-up is performed, increasing hori-
 399 zontal resolution from 4km to 500m (runs 1K100-1H, 2K50-1H, 4K25-1H, 05K150-1H)
 400 and vertical resolution accordingly. The horizontal to vertical resolution ratio is kept close
 401 to the Brunt-Vaisala to inertial frequencies ratio. It reveal that summer anticyclonic cold-

402 core signature $\overline{\delta T}$ and differential mixing $\overline{\xi}$ both continuously increase when decreasing
 403 the grid cell (see Fig.6c). Summer eddy SST inversions are then consistently correlated
 404 with an increased mixing. In addition a convergence behavior is observed for mixing at
 405 1km with 100 levels to $\xi \approx 3$, as no further mixing is obtained increasing the resolu-
 406 tion to 500m and 150 levels. Differential mixing appearing at 1km resolution implies that
 407 small scale processes, smaller than the eddy size are at stake. 1km horizontal resolution
 408 with a baroclinic first deformation radius around 11km entails that deformation radius
 409 to be explicitly resolved, which is not entirely effective for resolution of 2km or larger,
 410 similarly to other numerical studies (Marchesiello et al., 2011; Soufflet et al., 2016). On
 411 the other hand in winter very similar δT are retrieved at all resolution, with a maximum
 412 around $+0.4^\circ\text{C}$ (Fig.6a) and similar THFF suggesting that winter thermal loss is less af-
 413 fected by horizontal resolution. THFF slightly decreases for lower resolution, likely due
 414 to smoothing effect of strong SST patterns.

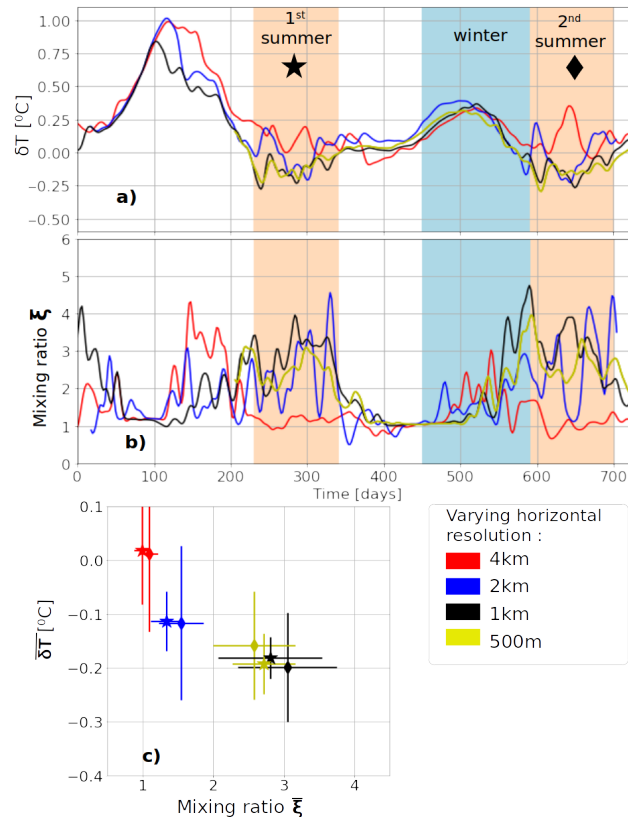


Figure 6. (a) δT and (b) ξ timeseries for experiments 1K100-1H, 2K50-1H, 4K25-1H, 05K150-1H listed in Tab.1 with SST retroaction on air-sea fluxes and varying horizontal resolution frequency. 2-days Gaussian smoothing is applied and summer periods are shaded in light red, winter in light blue. Due to computer memory issues, the first transient winter at 500m resolution was not recorded. (c) Summer-averaged eddy-induced SST anomalies ($\overline{\delta T}$) and mixing ratio ($\overline{\xi}$), with stars for the first summer and diamonds for the second one. Errorbars are ξ spread (30th percentile) over the same period.

415 For the eddy-induced mixed layer anomaly, similar values are obtained from 4km
 416 to 1km resolution ($\Delta MLD \approx 50m$), but a larger $\Delta MLD = 91m$ is retrieved at 500m
 417 resolution. This effect could be due to the partial resolution of sub-mesoscale processes

418 such as mixed layer instabilities (Boccaletti et al., 2007; Capet et al., 2008). Maximal
419 background mixed layer deepens when resolution gets finer down to 1km resolution (see
420 Fig.4g and 5g), in consistence with previous experiments (Couvelard et al., 2015). At
421 500m resolution, a closer look at the MLD evolution inside- and outside-eddy shows that
422 the outside-eddy MLD restratified earlier in run 05K150-1H (in March) than in run 1K100-
423 1H (in April) due to restratification beginning at submesoscale with mixed layer insta-
424 bilities (Fig.7b). But in both cases inside-eddy MLD reached the same depth (193m, see
425 Fig.7e-f). This suggests that maximal mixed layer inside-eddy indeed reached a max-
426 imum driven by air-sea cooling, while restratification outside-eddy occurred too late in
427 run 1K100-1H because vertical buoyancy fluxes are too weak (Capet et al., 2008). Com-
428 pared to Mediterranean MLD climatology, a restratification in April is indeed quite late
429 (Houpert et al., 2015).

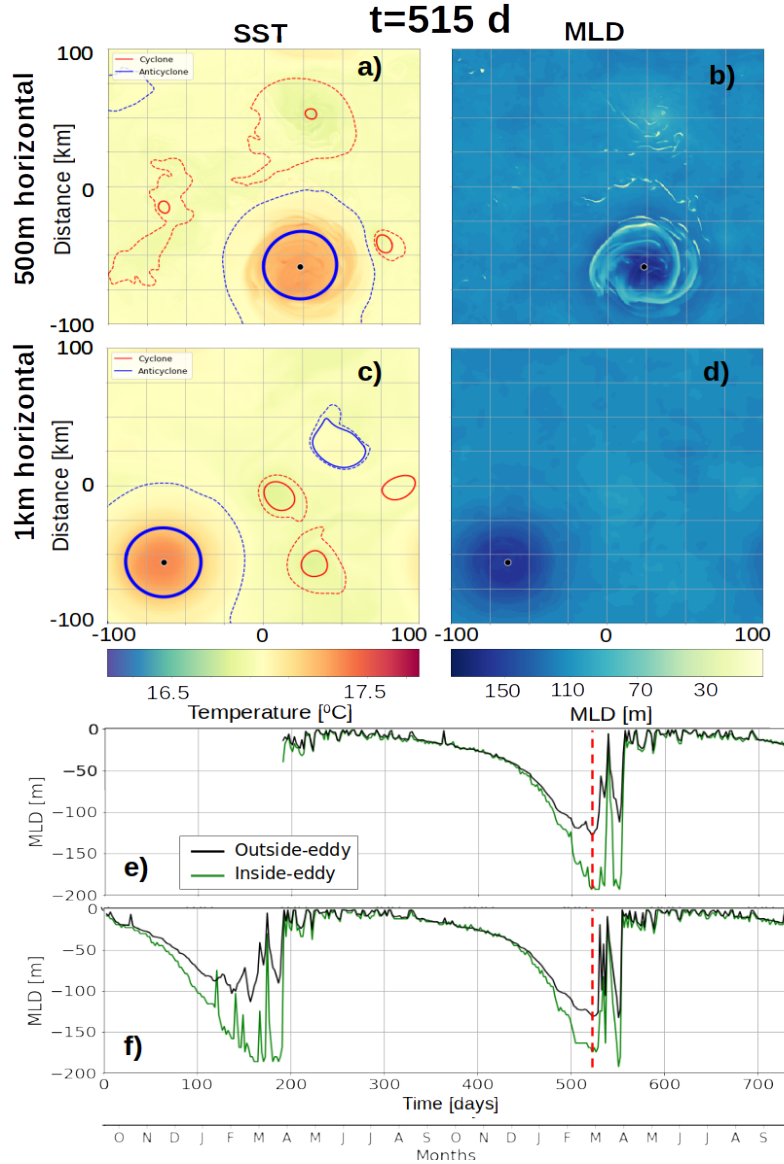


Figure 7. (a) SST with anticyclones and cyclones as in Fig.4 (the initial anticyclone has thicker contour) in 05K150-1H simulation. (b) MLD in 05K150-1H. (c) and (d) : same as (a) and (b) but in 1K100-1H simulation. (e) MLD time series inside-anticyclone (green) and outside-eddy (black) for the 05K150-1H simulation, a red dashed line indicates the time step shown in panels (a)-(d). Due to memory issues, the first transient winter was not recorded. (f) Same as (e) in 1K100-1H simulation.

430 Mixing patterns over the vertical in the 1km resolution simulation are also consistent with observations. Anticyclones were recently observed to enhance mixing at depth
 431 through the propagation of trapped near-inertial internal waves in their core. In studies from Martínez-Marrero et al. (2019) and Fernández-Castro et al. (2020), in situ measurements revealed lower dissipation rate ϵ in anticyclonic homogeneous core than in the
 432 neighboring background, and enhanced ϵ below at depth. In our numerical experiments, both diffusivity κ (Fig.8c) and dissipation rate ϵ (Fig.8e) match this feature, with enhanced mixing in summer below the anticyclone, up to one order of magnitude larger
 433
 434
 435
 436
 437

438 from 200 to 300m depth. The anticyclone subsurface core revealed by thick isopycnal
 439 displacement on Fig.8e, also shows locally reduced ϵ between 100 and 200m. Fig.8e is
 440 is then a striking reproduction of dissipation rate section obtained by Fernández-Castro
 441 et al. (2020) (see in particular their Fig.5f). However those in situ measurements could
 442 not compare outside- and inside-eddy mixing close to the surface, because the value range
 443 for ϵ would be too large with surface processes a lot more powerful than deep ocean ones.
 444 Numerical simulation enables to reveal that anticyclones also enhance mixing in near sur-
 445 face, with higher ϵ and κ just above the homogeneous core, in the upper 50 meters. The
 446 differential mixing ratio ξ previously shown in anticyclone time series then accurately
 447 measures a surface-enhanced mixing.

448 The seasonal cycle of eddy SST signature is then effectively reproduced at 1km hor-
 449 izontal resolution, close to observed value for the example shown above (Fig.3e). eddy
 450 SST seasonal shift correlates with increased mixing at the anticyclone core, in consis-
 451 tence with Moschos et al. (2022) hypothesis. This differential mixing is absent at 4km,
 452 but appears through $k - \epsilon$ mixing parametrization and converges at 1km resolution.

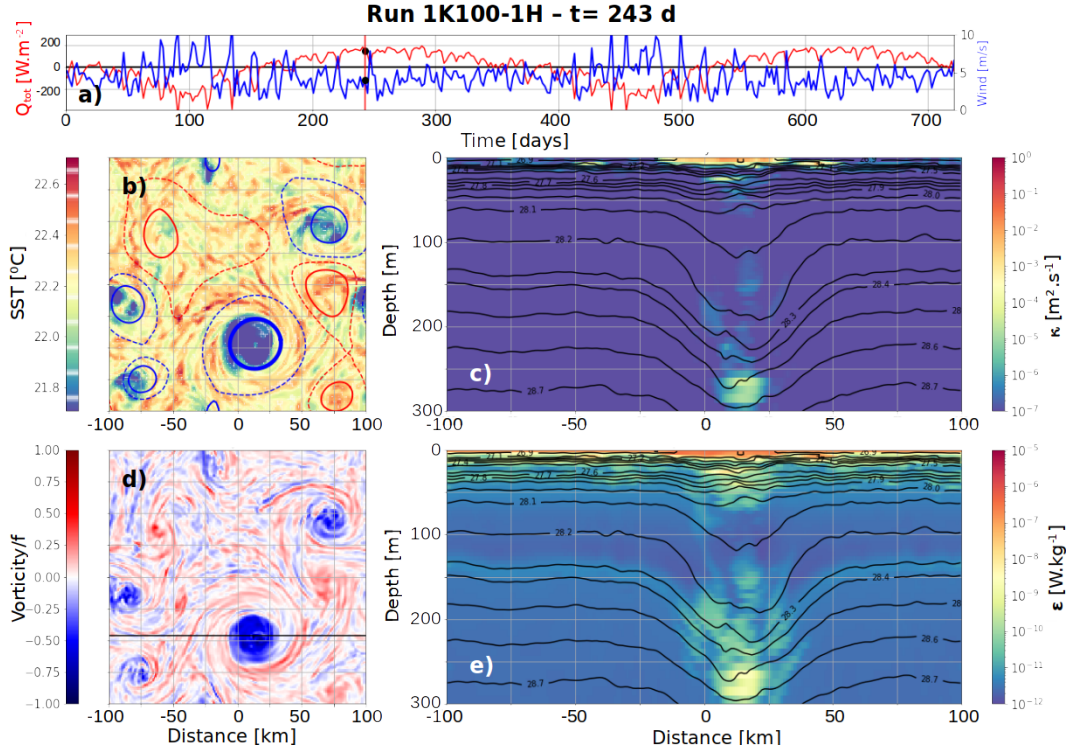


Figure 8. Snapshot at $t = 243 d$ for the 1K100-1H simulation (see Fig.5). (a) Wind speed (blue line) and Q_{tot} (red lines) timeseries. (b) SST and (d) surface vorticity normalized by f with eddy detections as in Fig.4 (initial anticyclone has a thicker contour). (c) κ and (e) ϵ vertical sections in the upper 300m with logarithmic color scales, in both case the colorbar lower bound is the minimal possible value (see Sect.2.1). Isopycnals are added in black lines.

453 3.2 Forcing frequency sensitivity

454 Sensitivity of the eddy SST signature δT and differential mixing ξ to forcing tem-
 455 poral resolution is investigated by progressively removing high frequencies from the at-
 456 mospheric inputs. These experiences are summarized as 1K100-1D to 1K100-1W in Ta-

457 ble 1, using 1-day, 3-days and 1-week atmospheric timeseries respectively. δT and dif-
 458 ferential mixing ξ timeseries for these experiments are shown in Fig.9a-b. Significantly
 459 cold SST signatures ($\overline{\delta T} \lesssim -0.2^\circ C$) are obtained together with strong mixing ($\bar{\xi} \approx 3$)
 460 for 1-hour and 1-day frequency, but no significant differential mixing is retrieved ($1 <$
 461 $\bar{\xi} < 1.5$) for all lower forcing frequencies (Fig.9c). This threshold behavior is a strong
 462 result and shows that spontaneous appearance of differential mixing is driven by small
 463 scale and high frequency features. With a Coriolis parameter $f = 9.0 \times 10^{-5} s^{-1} =$
 464 $1.24cpd$, the inertial period is about 19h, the 1-day forcing can then partly trigger near-
 465 inertial waves.

466 The relationship between $\overline{\delta T}$ and $\bar{\xi}$ is however less clear than for the resolution sen-
 467 sitivity analysis (Fig.6). No differential mixing is observed for forcing frequencies lower
 468 than 1 day, but summer cold-core signatures are still found ($\overline{\delta T} \gtrsim 0.1^\circ C$, see Table1),
 469 even for the 1-week forcing. δT timeseries clearly show for all frequencies a marked sea-
 470 sonal signal (Fig.6a). In particular a significant warm winter signature is always observed,
 471 with stable maximal value at $\delta T \approx +0.4^\circ C$. In the same context a surprising result is
 472 the summer averaged $\overline{\delta T}$ being colder on average at 1-day than 1-hour forcing, despite
 473 similar differential mixing. Temporal evolution of eddy SST anomalies reveals this ef-
 474 fect to be caused by a larger oscillation of the eddy surface signature (Fig.9a) about $\pm 0.2^\circ C$,
 475 hence larger errorbars at 1-day on Fig.9c. This suggests that other mechanisms not trig-
 476 gered by high frequency winds also contribute to the eddy SST seasonal cycle. If no dif-
 477 ferential vertical mixing is observed but if seasonal variations of the anticyclone SST (and
 478 hence surface density) is found, one can only hypothesize the role of lateral exchanges.
 479 Despite some tries, we were unsuccessful in quantifying eddy lateral exchanges follow-
 480 ing a varying $R_m(t)$ contour. No particular asymmetric wave modes was observed on SST
 481 snapshots, discarding the hypothesis of vortex Rossby waves (Guinn & Schubert, 1993;
 482 Montgomery & Kallenbach, 1997).

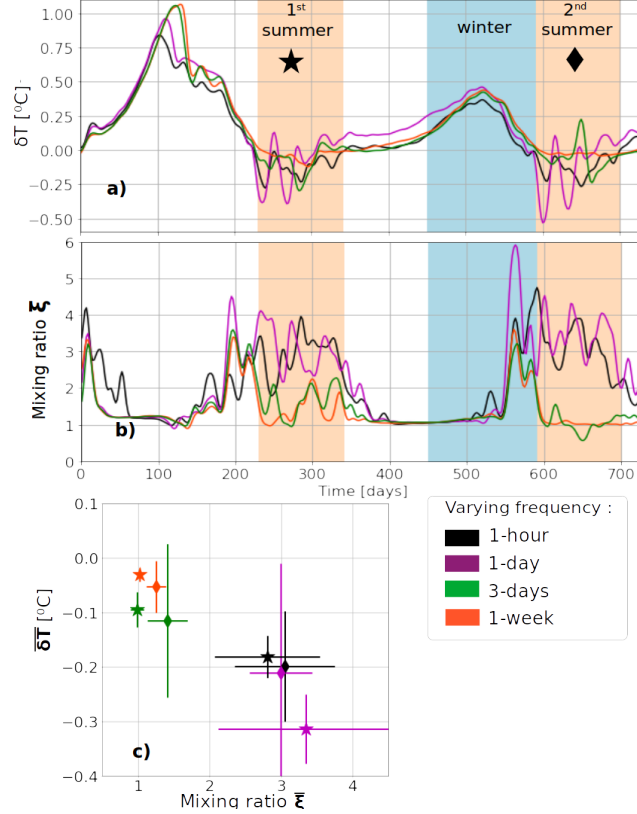


Figure 9. (a) δT and (b) ξ timeseries for experiments 1K100-1H, 1K100-1D, 1K100-3D and 1K100-1W listed in Tab.1 with SST retroaction on air-sea fluxes and varying forcing frequency. 2-days Gaussian smoothing is applied, summer periods are shaded in light red, winter in light blue. (c) Summer-averaged eddy-induced SST anomalies ($\overline{\delta T}$) and mixing ratio ($\overline{\xi}$), with stars for the first summer and diamonds for the second one.

483 Near-inertial internal waves are investigated using Fourier transforms on vertical
 484 speed anomalies in run 1K100-1H. We focus on a single vertical level at 20m in near-surface
 485 where the enhanced mixing occurs (see Fig.8c). Transforms are computed only in the
 486 second summer (590 to 700 simulated days) with a 1-hour sampling frequency. Follow-
 487 ing Babiano et al. (1987), inside-eddy spectrum is performed keeping only the inside-eddy
 488 area (around the eddy center with radius $2/3R_m(t)$) and the remaining area is set to 0
 489 before performing the Fourier transform. Similarly outside-eddy spectrum is performed
 490 blanking all value inside any eddy contours. The results clearly show a differential ef-
 491 fect inside-eddy vertical kinetic energy density revealing a second powerful peak at the
 492 effective inertial frequency $f_e = f + \zeta/2 \approx 1.0cpd$, lower than the inertia frequency
 493 (Fig.10a). Outside-eddy spectrum (Fig.10b) shows only one peak at the inertial frequency,
 494 and internal waves cannot propagate at lower frequencies due to the f -cut-off (Garrett
 495 & Munk, 1972). Normalizing by the investigated area, total vertical kinetic energy per
 496 unit surface is indeed higher inside the anticyclone ($4.19 \times 10^{-14} m^2 \cdot s^{-2} / m^2$) than outside-
 497 eddy ($1.64 \times 10^{-14} m^2 \cdot s^{-2} / m^2$) due to these powerful subinertial internal waves. An as-
 498 sumption of this method is however to assume that both inside- and outside-eddy ar-
 499 eas roughly keep the same area, which is verified. This result is consistent with (Kunze,
 500 1985) theory and recent numerical works (Danioux et al., 2015; Asselin & Young, 2020)
 501 subinertial waves ($\omega \lesssim f$) can be trapped in the anticyclone due to the locally lower
 502 absolute vorticity, and enhance mixing while breaking as proposed by Fernández-Castro
 503 et al. (2020).

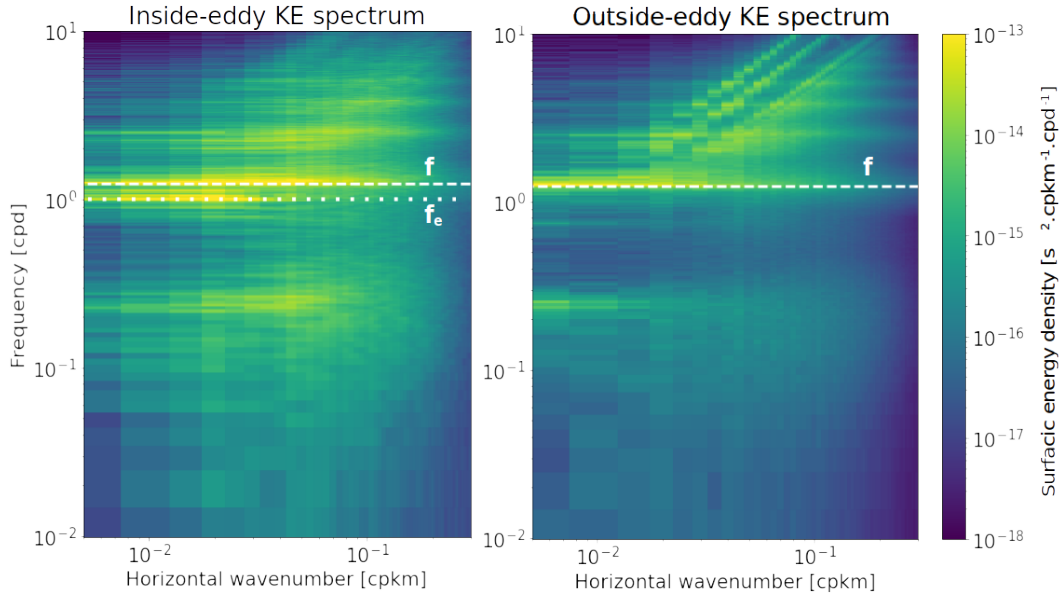


Figure 10. (a) Inside-eddy and (b) outside-eddy vertical kinetic energy density spectrum at 20m depth. For comparison, spectrum are normalized by the area of interest. Analysis performed on simulation 1K100-1H with 1-hour sampling. Normal (respectively effective) inertial frequencies $f = 1.24cpd$ ($f_e \approx 1.0cpd$) are highlighted by a white dashed (dotted) line.

504

3.3 Air-sea fluxes sensitivity

505

506

507

508

509

510

511

512

513

514

515

516

517

Sensitivity of the anticyclone temporal evolution to air-sea fluxes components is further investigated. A $1km$ resolution simulation experiment is run similarly as the 1K100-1H simulation without applying SST retroaction on air-sea fluxes (see Sect.2.3, run 1K100-1H-NoSST in Table 1). Although quite unrealistic, this experiment enables to check if the eddy SST anomaly seasonal shift and differential mixing observed in previous simulations are triggered by air-sea fluxes retroaction. Time series for SST reveals that eddy SST anomalies seasonal oscillation is retrieved without SST retroaction (Fig.11a-c), and summer cold-core signatures are even stronger : $\delta T \approx -0.8^\circ C$ the first summer and $\approx -0.8^\circ C$ the second one (Fig.11f). Simultaneously, differential mixing reaches $\xi \approx 3$, approximately the same value as run 1K100-1H (Fig.11h). This confirms that differential eddy mixing triggering the eddy SST variations is not linked to air-sea fluxes retroaction. However this feedback can modulate and dampen the δT seasonal cycle leading to reduced anomalies.

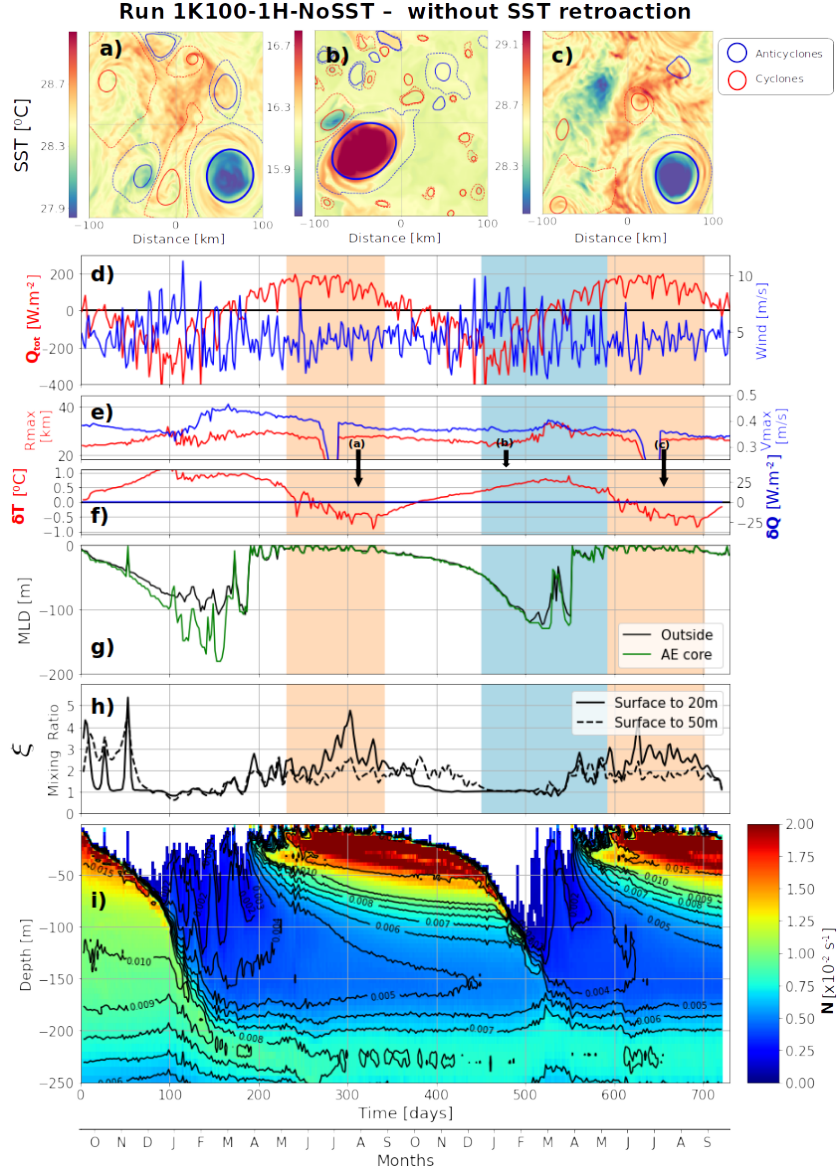


Figure 11. Simulation 1K100-1H-NoSST from Table 1. Same as in Fig.4 but without SST retroaction on air-sea fluxes. Discontinuities in R_{max} and V_{max} in panel (e) are due to the anticyclone crossing twice the grid borders.

518 SST retroaction acting as a negative feedback on SST anomalies can be analyti-
 519 cally expected as linear. The derivative of each heat component with respect to T_s is in-
 520 deed approximately constant (T_s being in Kelvin in Eq.13). Transfer coefficients C_E and
 521 C_S are indeed much more dependent on wind speed than on temperature, varying roughly
 522 about 0.2 with a T_s change of 1K. The most sensitive case is a low air-sea temperature
 523 difference with weak wind, in which the boundary layer can switch from stable to un-
 524 stable conditions (see for instance Fig.A1b from Pettenuzzo et al. (2010)). Assuming C_E
 525 and C_S are roughly constant with respect to temperature one gets :

$$\frac{\partial Q_{LW}^\uparrow}{\partial T_s} = -4\epsilon_{sb}\sigma_{sb}T_s^3 \approx -6 \text{ W.m}^{-2}.\text{K}^{-1} \quad (13)$$

$$\frac{\partial Q_{Lat}}{\partial T_s} \approx -\frac{\rho_a L_E C_E |V| 0.610}{P_{SL}} \frac{dP_{sat}}{dT_s} \approx -3 \times 10^1 W.m^{-2}.K^{-1} \quad (14)$$

$$\frac{\partial Q_{Sen}}{\partial T_s} = -\rho_a c_p C_S |V| \approx -1 \times 10^1 W.m^{-2}.K^{-1} \quad (15)$$

526 Altogether a thermal feedback on the order of $\frac{dQ_{tot}}{dT_s} \approx -4 \times 10^1 W.m^{-2}.K^{-1}$ is
 527 then expected, mostly driven by latent heat flux. THFF in Table 1 is computed only on
 528 the whole simulated year (from 365 to 730 days) and a value of $\approx -40 W.m^{-2}.K^{-1}$ is
 529 retrieved with a simple SST retroaction, in consistence with Eq.13 to 15. This value is
 530 relatively constant in our simulations, slightly decreasing for coarser resolution and lower
 531 forcing frequencies (see Table 1). $\partial C_E/\partial T_s$ and $\partial C_S/\partial T_s$ being also positive, taking this
 532 into account in Eq.14 leads to a even higher THFF estimate. THFF for the 1K100-1H
 533 simulation, defined here as δQ as a function of δT is shown in Fig.12. The obtained ther-
 534 mal feedback is consistent with previous estimates in coupled climate model : Ma et al.
 535 (2016) found a higher THFF ranging between 40 and $56 W.m^{-2}.K^{-1}$ but in the specific
 536 area of very warm eddies of the Kuroshio extension region. Moreton et al. (2021) found
 537 THFF ranging between 35 and $45 W.m^{-2}.K^{-1}$ over mesoscale eddies. They however used
 538 a composite approach in a model coupled with atmosphere and maximal oceanic reso-
 539 lution of $1/12^\circ$, for effective radius about $40km$. A coupled atmosphere layer is expected
 540 to further dampen the total THFF, taking into account other feedbacks than SST, in
 541 particular evaporation. Humidity is expected to increase over warm eddy, consequently
 542 decreasing the latent heat flux driving evaporation, whereas we applied a uniform h_{2m}
 543 field. Similar THFF in our simulations compared to coupled ocean-atmosphere models
 544 suggests that our results would not change significantly with more complex heat flux retroac-
 545 tion.

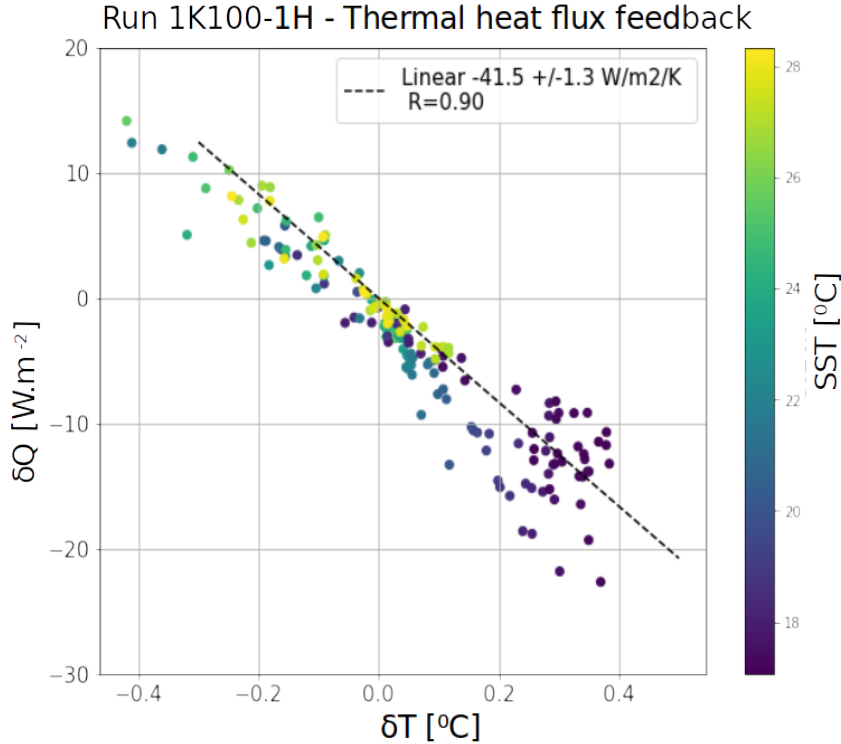


Figure 12. Thermal heat flux feedback in run 1K100-1H on the 2nd simulated year, with linear regression as dashed black line, δQ and δT are from Fig.5f. Regression coefficient and parameters are indicated in the legend.

546 Without SST retroaction on air-sea fluxes, the most important difference from run
 547 1K100-1H is the MLD anomaly variations. Outside-eddy, mixed layer evolution is very
 548 similar in runs 1K100-1H and 1K100-1H-NoSST reaching about 100m at its winter max-
 549 imum, but the eddy MLD anomaly is an order of magnitude smaller ($\Delta MLD = 10m$,
 550 see Fig.11h). With no THFF, the MLD deepens at the same rate outside- and inside-
 551 eddy. Winter MLD deepening can be computed estimating the thermal loss ΔT , assum-
 552 ing a linear thermal linear stratification $\partial_z T$:

$$MLD = \frac{\Delta T}{\partial_z T} \quad (16)$$

553 The thermal loss is the integration of the heat flux over winter duration D . Assum-
 554 ing stratification is at first order the same outside- and inside-eddy, MLD anomaly is then
 555 driven by heat flux lateral gradients :

$$\Delta MLD = \frac{D}{\rho_0 c_p \partial_z T} \delta Q \quad (17)$$

556 In the 1K100-1H with SST retroaction on air-sea fluxes, δQ is positive in winter
 557 reaching about $+15W.m^{-2}$ over 4 months. This leads to an estimate $\Delta MLD \approx 2 \times$
 558 $10^1 m$. This estimate should then be the eddy MLD anomaly contribution from THFF
 559 alone, but a lot higher difference is obtained between run 1K100-1H and 1K100-1H-NoSST.
 560 The main assumption in Eq.17 is that $\partial_z T$ is roughly the same inside- and outside-eddy.
 561 This is true in the upper layers where stratification is mostly the seasonal thermocline
 562 (see isopycnals in Fig.8c-d). At depth lower than 100m however, the anticyclone consti-
 563 tutes a more homogenized layer and this assumption should not hold as MLD should deepen
 564 faster inside-eddy, even with no SST retroaction. The very low ΔMLD found with no
 565 THFF then suggests that thermal feedback may also impact inside-eddy stratification.
 566 An example of inside-eddy MLD faster deepening is shown in Fig.3g : the MLD connects
 567 in February 2018 with the layer homogenized the previous winter and reaching quickly
 568 about 300m. Such mixed layer deepening acceleration is partly retrieved in run 1K100-
 569 1H around 500 days, with a MLD jump of about 30m (Fig.5g) inside-eddy but only about
 570 10m outside-eddy. This coincides with the mixing of the subsurface homogenized layer
 571 formed in the first winter, despite diffusion (stratification isolines progressively closing,
 572 Fig. 5i) as discussed earlier.

573 ΔMLD is however still relatively weak compared to the 200 to 300m MLD anoma-
 574 lies observed in Mediterranean anticyclones (Barboni, Coadou-Chaventon, et al., 2023).
 575 Two main hypotheses can be proposed, the first being that some interannual variabil-
 576 ity is needed. The second hypothesis is that layers homogenized by winter MLD progres-
 577 sively restratify at depth in summer due to numerical diffusion. MLD in the following
 578 winter will then have to break this numerical stratification. This second hypothesis en-
 579 tails that the vertical grid is not enough refined yet to correctly preserve homogenized
 580 layers from one winter to another. From the comparison between runs 1K100-1H and
 581 1K100-1H-NoSST shows that SST retroaction on air-sea fluxes is necessary to obtained
 582 eddy MLD anomalies, but quantitative description deserves further research and ΔMLD
 583 is not only driven by fluxes gradients at the eddy scale.

584 Conclusions

585 Idealized numerical experiment at high horizontal resolution and high frequency
 586 atmospheric forcing are able to qualitatively and quantitatively retrieve SST signature
 587 seasonal cycle for a mesoscale anticyclone. Starting from a surface intensified mesoscale
 588 anticyclone at $Ro \approx 0.16$, seasonal oscillations of the eddy SST anomalies are recov-
 589 ered with an 1km resolution, hourly atmospheric forcing and SST retroaction on air-sea

590 fluxes. Retrieved eddy anomalies are a warm winter SST feature at $\delta T \approx +0.5^\circ C$ and
 591 a cold summer SST at $\delta T \approx -0.2^\circ C$, in consistence with in situ observations. The shift
 592 from warm winter SST signature to summer cold one is partly explained by an increased
 593 vertical mixing in the anticyclone upper layers. This differential mixing is due to higher
 594 NIW energy propagation well captured through the $\kappa - \epsilon$ mixing parametrization.

595 A sensitivity analysis reveals that this differential mixing depends on the grid res-
 596 olution. Model diffusivity near the surface is then consistently 3 times higher in sum-
 597 mer inside-eddy than outside for horizontal resolution of 1km or smaller. This resolu-
 598 tion corresponds to an explicitly resolved first baroclinic deformation radius. Sensitiv-
 599 ity to the forcing frequency is investigated by progressively removing high frequencies
 600 from the atmospheric input fields. A threshold behavior is observed when forcing fre-
 601 quency is lower than a day, then differential mixing dramatically vanishes with no sig-
 602 nificant summer cold-core anticyclonic SST. Vertical kinetic energy signing internal wave
 603 propagation indeed reveals a second powerful peak at $\omega = 1.0cpd$ inside the anticyclone
 604 in near-surface, corresponding to the effective inertial frequency and responding to high
 605 frequency forcing. This peak is absent outside-eddy because the cut-off inertia frequency
 606 $f = 1.24cpd$ is higher. Such an analysis suggests a significant impact of the eddy vort-
 607 icity as cut-off frequency in allowing or not the selective NIW propagation. Weaker eddy
 608 SST seasonal oscillations are also retrieved in the absence of high frequently forcing and
 609 consequently without differential mixing (3-days and 1-week experiments). This high-
 610 lights that other contributions might participate to these eddy SST signatures, in par-
 611 ticular lateral exchanges. A new question for future research opened by this eddy-modulated
 612 mixing is how it depends on the eddy vorticity and size.

613 SST retroaction on air-sea fluxes is not found to be responsible of eddy SST sig-
 614 natures seasonal shift, as the seasonal oscillation is retrieved with and without air-sea
 615 fluxes parametrization. However this retroaction is logically found to dampen the SST
 616 anomalies, and then reduces eddy anomalies magnitude in both summer and winter. The
 617 average thermal heat flux feedback of our mesoscale anticyclone is approximately $40W.m^{-2}.K^{-1}$,
 618 in consistence with analytical derivation and previous studies.

619 Significant eddy-induced mixed layer anomaly $\Delta MLD \approx 50m$ are found at 1km
 620 horizontal resolution, only in the presence of SST retroaction on fluxes. Linear MLD anomaly
 621 analysis suggests that the thermal feedback is only responsible for about half of the MLD
 622 anomaly. Further analysis should then investigate how SST retroaction impacts inside-
 623 eddy stratification. MLD anomalies do not completely converge at 1km as larger anoma-
 624 lies are obtained with a 500m resolution due to restratification beginning outside-eddy
 625 driven by submesoscale instabilities, despite similar maximal mixed-layer at the anticy-
 626 clone core. No restratification delay is clearly observed, but it could occur at even higher
 627 resolution inside the anticyclone because the balanced density gradients inhibits mixed
 628 layer instabilities there. This hypothesis is consistent with observations (Barboni, Coadou-
 629 Chaventon, et al., 2023) but would deserve more investigation in the future. This result
 630 is also important as the mixed layer is a significant driver of atmospheric and bio-geochemical
 631 exchanges, and the explicit resolution of submesoscale processes might be needed to ac-
 632 curately reproduce their interaction with eddies (Capet et al., 2008; Lévy et al., 2018).
 633 An important result is still that significant ΔMLD is retrieved only when SST exerts
 634 a retroaction on air-sea fluxes, but the quantitative description of its evolution would de-
 635 serve more analysis.

636 This is the first time that subinertial waves concentration in anticyclones is linked
 637 to an increased mixing in near surface, spontaneously retrieved through the $k-\epsilon$ mix-
 638 ing closure. Mixing modulation by eddies suggests a strong scale interactions between
 639 subinertial internal waves ($\omega \lesssim f$) and the mesoscale ($\omega \ll f$). Differential mixing trig-
 640 gered by high frequency winds is an important result highlighting the need of both fine
 641 resolution and atmospheric forcing at sufficiently high frequency to correctly reproduce
 642 mesoscale eddies evolution. At present stage, global operational models do not have the

643 spatial resolution to capture these phenomena. According to this study, 1/120 °resolution
 644 with 100 vertical levels would then be necessary to reproduce accurately mesoscale tem-
 645 poral evolution.

646 Open Research Section

647 In-situ profiles colocalized with mesoscale eddies database is available at <https://doi.org/10.17882/93077>. AMEDA eddy tracking algorithm is open source and avail-
 648 able at <https://github.com/briaclevu/AMEDA>. ERA5 atmospheric reanalysis are pub-
 649 650 licly available at <https://doi.org/10.24381/cds.adbb2d47>. The CROCO code is pub-
 651 licly available at <https://www.croco-ocean.org/>.

652 Acknowledgments

653 Authors gratefully acknowledge *Ifremer* and *Service Hydrographique et Océanographique de la Marine*
 654 *de la Marine* for their use of the *Datarmor* computing facility. Authors acknowledge Evan-
 655 gelos Moschos (*Amphitrite*) for the reuse of his figures as snapshots in Fig.3a-d. Authors
 656 also acknowledge fruitful discussions with Clément Vic (*Ifremer*), in particular the com-
 657 parison with observations in Fig.8 and 10.

658 References

- 659 Amores, A., Jordà, G., Arsouze, T., & Le Sommer, J. (2018). Up to what extent can
 660 we characterize ocean eddies using present-day gridded altimetric products?
 661 *Journal of Geophysical Research: Oceans*, *123*(10), 7220–7236.
- 662 Arai, M., & Yamagata, T. (1994). Asymmetric evolution of eddies in rotating shal-
 663 low water. *Chaos: An Interdisciplinary Journal of Nonlinear Science*, *4*(2),
 664 163–175.
- 665 Aroucha, L. C., Veleda, D., Lopes, F. S., Tyaquicã, P., Lefèvre, N., & Araujo, M.
 666 (2020). Intra- and inter-annual variability of north brazil current rings us-
 667 ing angular momentum eddy detection and tracking algorithm: Observa-
 668 tions from 1993 to 2016. *Journal of Geophysical Research: Oceans*, *125*(12),
 669 e2019JC015921. doi: <https://doi.org/10.1029/2019JC015921>
- 670 Asselin, O., & Young, W. R. (2020). Penetration of wind-generated near-inertial
 671 waves into a turbulent ocean. *Journal of Physical Oceanography*, *50*(6), 1699–
 672 1716.
- 673 Ayouche, A., De Marez, C., Morvan, M., L’hegaret, P., Carton, X., Le Vu, B., &
 674 Stegner, A. (2021). Structure and dynamics of the ras al hadd oceanic dipole
 675 in the arabian sea. In *Oceans* (Vol. 2, pp. 105–125).
- 676 Babiano, A., Basdevant, C., Legras, B., & Sadourny, R. (1987). Vorticity and
 677 passive-scalar dynamics in two-dimensional turbulence. *Journal of Fluid Me-*
 678 *chanics*, *183*, 379–397.
- 679 Barboni, A., Coadou-Chaventon, S., Stegner, A., Le Vu, B., & Dumas, F. (2023).
 680 How subsurface and double-core anticyclones intensify the winter mixed-layer
 681 deepening in the mediterranean sea. *Ocean Science*, *19*(2), 229–250.
- 682 Barboni, A., Lazar, A., Stegner, A., & Moschos, E. (2021). Lagrangian eddy track-
 683 ing reveals the eratosthenes anticyclonic attractor in the eastern levantine
 684 basin. *Ocean Science*, *17*(5), 1231–1250.
- 685 Barboni, A., Stegner, A., Le Vu, B., & Dumas, F. (2023). *2000-2021 in situ pro-*
 686 *files colocalized with ameda eddy detections from 1/8 aviso altimetry in the*
 687 *mediterranean sea*. SEANOE.
- 688 Boccaletti, G., Ferrari, R., & Fox-Kemper, B. (2007). Mixed layer instabilities and
 689 restratification. *Journal of Physical Oceanography*, *37*(9), 2228–2250.
- 690 Capet, X., McWilliams, J. C., Molemaker, M. J., & Shchepetkin, A. F. (2008).
 691 Mesoscale to submesoscale transition in the california current system. part i:

- 692 Flow structure, eddy flux, and observational tests. *Journal of physical oceanog-*
693 *raphy*, *38*(1), 29–43.
- 694 Carton, X., Flierl, G., & Polvani, L. (1989). The generation of tripoles from unsta-
695 ble axisymmetric isolated vortex structures. *EPL (Europhysics Letters)*, *9*(4),
696 339.
- 697 Chaigneau, A., Eldin, G., & Dewitte, B. (2009). Eddy activity in the four major
698 upwelling systems from satellite altimetry (1992–2007). *Progress in Oceanogra-*
699 *phy*, *83*(1-4), 117–123.
- 700 Chelton, D. B., Gaube, P., Schlax, M. G., Early, J. J., & Samelson, R. M. (2011).
701 The influence of nonlinear mesoscale eddies on near-surface oceanic chloro-
702 phyll. *Science*, *334*(6054), 328–332.
- 703 Chelton, D. B., Schlax, M. G., & Samelson, R. M. (2011). Global observations of
704 nonlinear mesoscale eddies. *Progress in oceanography*, *91*(2), 167–216.
- 705 Chelton, D. B., Schlax, M. G., Samelson, R. M., & de Szoeke, R. A. (2007). Global
706 observations of large oceanic eddies. *Geophysical Research Letters*, *34*(15).
- 707 Couvelard, X., Dumas, F., Garnier, V., Ponte, A., Talandier, C., & Treguier, A.-M.
708 (2015). Mixed layer formation and restratification in presence of mesoscale and
709 submesoscale turbulence. *Ocean Modelling*, *96*, 243–253.
- 710 Danioux, E., Klein, P., & Rivière, P. (2008). Propagation of wind energy into the
711 deep ocean through a fully turbulent mesoscale eddy field. *Journal of Physical*
712 *Oceanography*, *38*(10), 2224–2241.
- 713 Danioux, E., Vanneste, J., & Bühler, O. (2015). On the concentration of near-
714 inertial waves in anticyclones. *Journal of Fluid Mechanics*, *773*, R2.
- 715 D’Asaro, E. A. (1995). Upper-ocean inertial currents forced by a strong storm.
716 part iii: Interaction of inertial currents and mesoscale eddies. *Journal of physi-*
717 *cal oceanography*, *25*(11), 2953–2958.
- 718 de Marez, C., Le Corre, M., & Gula, J. (2021). The influence of merger and con-
719 vection on an anticyclonic eddy trapped in a bowl. *Ocean Modelling*, *167*,
720 101874.
- 721 Doglioli, A., Blanke, B., Speich, S., & Lapeyre, G. (2007). Tracking coherent struc-
722 tures in a regional ocean model with wavelet analysis: Application to cape
723 basin eddies. *Journal of Geophysical Research: Oceans*, *112*(C5).
- 724 Escudier, R., Renault, L., Pascual, A., Brasseur, P., Chelton, D., & Beuvier, J.
725 (2016). Eddy properties in the western mediterranean sea from satellite alti-
726 metry and a numerical simulation. *Journal of Geophysical Research: Oceans*,
727 *121*(6), 3990–4006.
- 728 Everett, J., Baird, M., Oke, P., & Suthers, I. (2012). An avenue of eddies: Quantify-
729 ing the biophysical properties of mesoscale eddies in the tasman sea. *Geophysi-*
730 *cal Research Letters*, *39*(16).
- 731 Fairall, C. W., Bradley, E. F., Hare, J., Grachev, A. A., & Edson, J. B. (2003).
732 Bulk parameterization of air–sea fluxes: Updates and verification for the coare
733 algorithm. *Journal of climate*, *16*(4), 571–591.
- 734 Fernández-Castro, B., Evans, D. G., Frajka-Williams, E., Vic, C., & Naveira-
735 Garabato, A. C. (2020). Breaking of internal waves and turbulent dissipation
736 in an anticyclonic mode water eddy. *Journal of Physical Oceanography*, *50*(7),
737 1893–1914.
- 738 Frenger, I., Gruber, N., Knutti, R., & Münnich, M. (2013). Imprint of southern
739 ocean eddies on winds, clouds and rainfall. *Nature geoscience*, *6*(8), 608–612.
- 740 Garrett, C., & Munk, W. (1972). Space-time scales of internal waves. *Geophysical*
741 *Fluid Dynamics*, *3*(3), 225–264.
- 742 Gaube, P., J. McGillicuddy Jr, D., & Moulin, A. J. (2019). Mesoscale eddies mod-
743 ulate mixed layer depth globally. *Geophysical Research Letters*, *46*(3), 1505–
744 1512.
- 745 Graves, L. P., McWilliams, J. C., & Montgomery, M. T. (2006). Vortex evolution
746 due to straining: A mechanism for dominance of strong, interior anticyclones.

- 747 *Geophysical and Astrophysical Fluid Dynamics*, 100(3), 151–183.
- 748 Guinn, T. A., & Schubert, W. H. (1993). Hurricane spiral bands. *Journal of the at-*
749 *mospheric sciences*, 50(20), 3380–3403.
- 750 Hausmann, U., & Czaja, A. (2012). The observed signature of mesoscale eddies in
751 sea surface temperature and the associated heat transport. *Deep Sea Research*
752 *Part I: Oceanographic Research Papers*, 70, 60–72.
- 753 Hersbach, H., Bell, B., Berrisford, P., Hirahara, S., Horányi, A., Muñoz-Sabater, J.,
754 ... others (2020). The era5 global reanalysis. *Quarterly Journal of the Royal*
755 *Meteorological Society*, 146(730), 1999–2049.
- 756 Houpert, L., Testor, P., De Madron, X. D., Somot, S., D’ortenzio, F., Estournel, C.,
757 & Lavigne, H. (2015). Seasonal cycle of the mixed layer, the seasonal thermo-
758 cline and the upper-ocean heat storage rate in the mediterranean sea derived
759 from observations. *Progress in Oceanography*, 132, 333–352.
- 760 Ioannou, A., Stegner, A., Dubos, T., Le Vu, B., & Speich, S. (2020). Generation
761 and intensification of mesoscale anticyclones by orographic wind jets: The case
762 of ierapetra eddies forced by the etesians. *Journal of Geophysical Research:*
763 *Oceans*, 125(8), e2019JC015810.
- 764 Ioannou, A., Stegner, A., & Dumas, F. (2021). Three-dimensional evolution of
765 mesoscale anticyclones in the lee of crete. *Frontiers in Marine Science*.
- 766 Ioannou, A., Stegner, A., Tuel, A., LeVu, B., Dumas, F., & Speich, S. (2019). Cy-
767 clostrophic corrections of aviso/duacs surface velocities and its application to
768 mesoscale eddies in the mediterranean sea. *Journal of Geophysical Research:*
769 *Oceans*, 124(12), 8913–8932.
- 770 Itoh, S., & Yasuda, I. (2010). Characteristics of mesoscale eddies in the kuroshio-
771 oyashio extension region detected from the distribution of the sea surface
772 height anomaly. *Journal of Physical Oceanography*, 40(5), 1018–1034.
- 773 Juza, M., Mourre, B., Renault, L., Gómara, S., Sebastián, K., Lora, S., ... others
774 (2016). Socib operational ocean forecasting system and multi-platform valida-
775 tion in the western mediterranean sea. *Journal of Operational Oceanography*,
776 9(sup1), s155–s166.
- 777 Kunze, E. (1985). Near-inertial wave propagation in geostrophic shear. *Journal of*
778 *Physical Oceanography*, 15(5), 544–565.
- 779 Laxenaire, R., Speich, S., Blanke, B., Chaigneau, A., Pegliasco, C., & Stegner, A.
780 (2018). Anticyclonic eddies connecting the western boundaries of indian and
781 atlantic oceans. *Journal of Geophysical Research: Oceans*, 123(11), 7651–
782 7677.
- 783 Laxenaire, R., Speich, S., & Stegner, A. (2020). Agulhas ring heat content and
784 transport in the south atlantic estimated by combining satellite altimetry and
785 argo profiling floats data. *Journal of Geophysical Research: Oceans*, 125(9),
786 e2019JC015511.
- 787 Le Vu, B., Stegner, A., & Arsouze, T. (2018). Angular momentum eddy detection
788 and tracking algorithm (amedea) and its application to coastal eddy formation.
789 *Journal of Atmospheric and Oceanic Technology*, 35(4), 739–762.
- 790 Lévy, M., Franks, P. J., & Smith, K. S. (2018). The role of submesoscale currents in
791 structuring marine ecosystems. *Nature communications*, 9(1), 4758.
- 792 Liu, F., Zhou, H., Huang, W., & Wen, B. (2020). Submesoscale eddies observation
793 using high-frequency radars: A case study in the northern south china sea.
794 *IEEE Journal of Oceanic Engineering*, 46(2), 624–633.
- 795 Liu, Y., Zheng, Q., & Li, X. (2021). Characteristics of global ocean abnormal
796 mesoscale eddies derived from the fusion of sea surface height and temperature
797 data by deep learning. *Geophysical Research Letters*, 48(17), e2021GL094772.
- 798 Ma, X., Jing, Z., Chang, P., Liu, X., Montuoro, R., Small, R. J., ... others (2016).
799 Western boundary currents regulated by interaction between ocean eddies and
800 the atmosphere. *Nature*, 535(7613), 533–537.
- 801 Marchesiello, P., Capet, X., Menkes, C., & Kennan, S. C. (2011). Submesoscale dy-

- 802 namics in tropical instability waves. *Ocean Modelling*, *39*(1-2), 31–46.
- 803 Mariotti, A. (2010). Recent changes in the mediterranean water cycle: a pathway
804 toward long-term regional hydroclimatic change? *Journal of Climate*, *23*(6),
805 1513–1525.
- 806 Martínez-Marrero, A., Barceló-Llull, B., Pallàs-Sanz, E., Aguiar-González, B.,
807 Gordo, C., Grisolia, D., . . . Arístegui, J. (2019). Near-inertial wave trapping
808 near the base of an anticyclonic mesoscale eddy under normal atmospheric
809 conditions. *Journal of Geophysical Research: Oceans*, *124*(11), 8455–8467.
- 810 Mason, E., Pascual, A., & McWilliams, J. C. (2014). A new sea surface height–based
811 code for oceanic mesoscale eddy tracking. *Journal of Atmospheric and Oceanic
812 Technology*, *31*(5), 1181–1188.
- 813 Mason, E., Ruiz, S., Bourdalle-Badie, R., Reffray, G., García-Sotillo, M., & Pascual,
814 A. (2019). New insight into 3-d mesoscale eddy properties from cmems opera-
815 tional models in the western mediterranean. *Ocean Science*, *15*(4), 1111–1131.
- 816 Mkhinini, N., Coimbra, A. L. S., Stegner, A., Arsouze, T., Taupier-Letage, I., &
817 Béranger, K. (2014). Long-lived mesoscale eddies in the eastern mediterranean
818 sea: Analysis of 20 years of aviso geostrophic velocities. *Journal of Geophysical
819 Research: Oceans*, *119*(12), 8603–8626.
- 820 Montgomery, M. T., & Kallenbach, R. J. (1997). A theory for vortex rossby-waves
821 and its application to spiral bands and intensity changes in hurricanes. *Quar-
822 terly Journal of the Royal Meteorological Society*, *123*(538), 435–465.
- 823 Moreton, S., Ferreira, D., Roberts, M., & Hewitt, H. (2021). Air-sea turbulent heat
824 flux feedback over mesoscale eddies. *Geophysical Research Letters*, *48*(20),
825 e2021GL095407.
- 826 Moschos, E., Barboni, A., & Stegner, A. (2022). Why do inverse eddy surface tem-
827 perature anomalies emerge? the case of the mediterranean sea. *Remote Sens-
828 ing*, *14*(15), 3807.
- 829 Nencioli, F., Dong, C., Dickey, T., Washburn, L., & McWilliams, J. C. (2010).
830 A vector geometry–based eddy detection algorithm and its application to a
831 high-resolution numerical model product and high-frequency radar surface
832 velocities in the southern california bight. *Journal of atmospheric and oceanic
833 technology*, *27*(3), 564–579.
- 834 Olson, D. B., & Evans, R. H. (1986). Rings of the agulhas current. *Deep Sea Re-
835 search Part A. Oceanographic Research Papers*, *33*(1), 27–42.
- 836 Paulson, C. A., & Simpson, J. J. (1977). Irradiance measurements in the upper
837 ocean. *Journal of Physical Oceanography*, *7*(6), 952–956.
- 838 Penven, P., Halo, I., Pous, S., & Marié, L. (2014). Cyclogeostrophic balance in the
839 mozambique channel. *Journal of Geophysical Research: Oceans*, *119*(2), 1054–
840 1067.
- 841 Perfect, B., Kumar, N., & Riley, J. (2020). Energetics of seamount wakes. part i:
842 Energy exchange. *Journal of Physical Oceanography*, *50*(5), 1365–1382.
- 843 Perret, G., Stegner, A., Farge, M., & Pichon, T. (2006). Cyclone-anticyclone asym-
844 metry of large-scale wakes in the laboratory. *Physics of Fluids*, *18*(3).
- 845 Pessini, F., Olita, A., Cotroneo, Y., & Perilli, A. (2018). Mesoscale eddies in the
846 algerian basin: do they differ as a function of their formation site? *Ocean Sci-
847 ence*, *14*(4), 669–688.
- 848 Pettenuzzo, D., Large, W., & Pinardi, N. (2010). On the corrections of era-40 sur-
849 face flux products consistent with the mediterranean heat and water budgets
850 and the connection between basin surface total heat flux and nao. *Journal of
851 Geophysical Research: Oceans*, *115*(C6).
- 852 Richardson, P. L. (1980). Gulf stream ring trajectories. *Journal of Physical
853 Oceanography*, *10*(1), 90–104.
- 854 Rodi, W. (1987). Examples of calculation methods for flow and mixing in stratified
855 fluids. *Journal of Geophysical Research: Oceans*, *92*(C5), 5305–5328. doi: 10
856 .1029/JC092iC05p05305

- 857 Shchepetkin, A. F., & McWilliams, J. C. (2005). The regional oceanic modeling
858 system (roms): a split-explicit, free-surface, topography-following-coordinate
859 oceanic model. *Ocean Modelling*, *9*(4), 347–404.
- 860 Smith, W. H., & Sandwell, D. T. (1997). Global sea floor topography from satellite
861 altimetry and ship depth soundings. *Science*, *277*(5334), 1956–1962.
- 862 Soufflet, Y., Marchesiello, P., Lemarié, F., Jouanno, J., Capet, X., Debreu, L., &
863 Benschila, R. (2016). On effective resolution in ocean models. *Ocean Modelling*,
864 *98*, 36–50.
- 865 Stegner, A., & Dritschel, D. (2000). A numerical investigation of the stability of iso-
866 lated shallow water vortices. *Journal of Physical Oceanography*, *30*(10), 2562–
867 2573.
- 868 Stegner, A., Le Vu, B., Dumas, F., Ghannami, M. A., Nicolle, A., Durand, C., &
869 Faugere, Y. (2021). Cyclone-anticyclone asymmetry of eddy detection on
870 gridded altimetry product in the mediterranean sea. *Journal of Geophysical*
871 *Research: Oceans*, *126*(9), e2021JC017475.
- 872 Steinberg, J. M., Cole, S. T., Drushka, K., & Abernathey, R. P. (2022). Seasonality
873 of the mesoscale inverse cascade as inferred from global scale-dependent eddy
874 energy observations. *Journal of Physical Oceanography*, *52*(8), 1677–1691.
- 875 Sun, W., Dong, C., Tan, W., & He, Y. (2019). Statistical characteristics of cyclonic
876 warm-core eddies and anticyclonic cold-core eddies in the north pacific based
877 on remote sensing data. *Remote Sensing*, *11*(2), 208.
- 878 Sun, W., Dong, C., Wang, R., Liu, Y., & Yu, K. (2017). Vertical structure anomalies
879 of oceanic eddies in the kuroshio extension region. *Journal of Geophysical Re-*
880 *search: Oceans*, *122*(2), 1476–1496.
- 881 Sverdrup, H. U., Johnson, M. W., Fleming, R. H., et al. (1942). *The oceans: Their*
882 *physics, chemistry, and general biology* (Vol. 1087) (No. 8). Prentice-Hall New
883 York.
- 884 Trott, C. B., Subrahmanyam, B., Chaigneau, A., & Roman-Stork, H. L. (2019).
885 Eddy-induced temperature and salinity variability in the arabian sea. *Geophys-*
886 *ical Research Letters*, *46*(5), 2734–2742.
- 887 Umlauf, L., & Burchard, H. (2003). A generic length-scale equation for geophysical
888 turbulence models. *Journal of Marine Research*, *61*(2), 235–265.
- 889 Villas Bôas, A., Sato, O., Chaigneau, A., & Castelão, G. (2015). The signature
890 of mesoscale eddies on the air-sea turbulent heat fluxes in the south atlantic
891 ocean. *Geophysical Research Letters*, *42*(6), 1856–1862.
- 892 Zhai, X., Greatbatch, R. J., & Kohlmann, J.-D. (2008). On the seasonal variability
893 of eddy kinetic energy in the gulf stream region. *Geophysical Research Letters*,
894 *35*(24).